Top Quark Mass Measurement: Prospects of Commissioning Studies for Early LHC Data in the ATLAS Detector

Emanuel Rauter

Dissertation

Max-Planck-Institut für Physik
(Werner-Heisenberg-Institut)

Technische Universität München

TECHNISCHE UNIVERSITÄT MÜNCHEN

Max-Planck-Institut für Physik
(Werner-Heisenberg-Institut)

Top Quark Mass Measurement: Prospects of Commissioning Studies for Early LHC Data in the ATLAS Detector

Emanuel Rauter

Vollständiger Abdruck der von der Fakultät für Physik
der Technischen Universität München zur Erlangung des akademischen Grades eines
Doktors der Naturwissenschaften (Dr. rer. nat.)
genehmigten Dissertation.

Vorsitzender: Univ.-Prof. Dr. A.J. Buras
Prüfer der Dissertation:
1. Hon.-Prof. Dr. S. Bethke
2. Univ.-Prof. Dr. St. Paul

Die Dissertation wurde am 5. Juni 2009 bei der Technischen Universität München eingereicht und durch die Fakultät für Physik am 1. Juli 2009 angenommen.

Abstract

A study to prepare a top quark mass measurement with early LHC data was carried out. The top quark reconstruction in the lepton plus jets decay channel using a simple and robust cut-based method has been studied. In particular, no b-tagging information was used. An in-situ jet calibration method was applied in order to minimise the systematic error due to jet energy scale. The reconstruction method is explained and its application on 145 pb^{-1} of simulated data is presented. Systematic effects and limitations of the method are discussed. Before applying the in-situ calibration, the dominant systematic error is found to be the jet energy scale as well as the combinatorial background. After applying the in-situ calibration, only the latter remains dominant. With a top quark mass of 172.5 GeV as input to the simulation, the method e.g. in the electron channel yields $\mathrm{m_t^{electron}} = 167.22 \pm (2.38)_{\mathrm{stat}}\ (^{+4.07}_{-3.16})_{\mathrm{syst}}$ GeV. First real data - both from cosmic muons and from LHC single beams - are used to study the in-situ performance of the ATLAS calorimeter system. Also included are calibration measurements of the electronics readout system. They yield a detector test of the expected calorimeter performance.

Contents

Introduction

At the Conseil Européenne pour la Recherche Nucléaire (CERN) the structure of matter has been studied in the last 50 years. Since then, the scale of nuclear physics has been left behind and experiments with higher and higher energies allowed to look deeper and deeper into the structure beyond.
In a new effort the Large Hadron Collider (LHC) has bee built to provide two colliding proton beams with a centre of mass energy of 14 TeV. At two high luminosity interaction points of the LHC multipurpose detectors have been constructed. One of these detectors is ATLAS (A Toroidal LHC ApparatuS). After the installation of ATLAS in the experimental cavern, it is of crucial importance to commission the detector and understand its performance as-built. This includes investigations on detector level such as signal and homogeneity studies as well as the preparation of first physics analysis.
Since summer 2006 the calorimeter system of ATLAS is regularly taking data with cosmic muons. In these data the first real physics signals are recorded and thus offer a broad field of commissioning studies for the calorimeters, the data acquisition chain and the trigger system.
Besides the commissioning of the detector hardware it is also of importance to develop and prepare analysis methods for first physics measurements. The decay of the top quark is an interesting topic, as $t\bar{t}$ pairs will be produced at high rates already at the very early stage of LHC operation. The top quark decay into leptons plus jets is a good candidate for an early physics analysis as it offers a rather clean trigger signature which facilitates background suppression. Using the hadronically decaying top quark for the actual reconstruction, it is possible to study the level of the jet energy scale calibration and to test in-situ calibration strategies.

The thesis is structured into six chapters:

1. **Top Quark Physics** The standard model of particle physics is briefly recalled. Here the main focus of attention will be given to the top quark production and decay mechanism in proton-proton collisions. The special role of the top quark within the standard model will briefly be illustrated. A short overview over the Monte Carlo generators used for the simulation of data will be given.

2. **The ATLAS Detector - Design and Performance** A brief description of the Large Hadron Collider at CERN will be given and the design of the ATLAS detector will be discussed. The physics performance goals motivating the design of ATLAS and the relevant sub-detectors and their expected performance will be reviewed briefly.

3. **Detector Commissioning and Calibration** Results from studies carried out in the scope of commissioning the liquid argon calorimeter system after its installation in the detector cavern will be presented. In particular, calibration measurements as well as signal studies with data from cosmic muons and first single beam LHC data will be discussed.

4. **Physics Objects Reconstruction and Calibration** The reconstruction of physics objects which are the basis of any data analysis will be discussed. In particular the focus is laid on energy reconstruction and calibration of clusters and jets as they are used in the top quark mass reconstruction presented in the last chapter.

5. **Top Quark Mass Reconstruction with Local Hadron Calibration** A study to prepare a top quark mass measurement with early LHC data was conducted. The top quark reconstruction was set up as a simple and robust cut-based method. An in-situ calibration method was applied in order to minimise the systematic error due to jet energy scale calibration. The reconstruction method will be explained and its application on 145 pb^{-1} of simulated data will be presented. Systematic effects and limitations of the method will be discussed.

6. **Conclusions** The findings and open issues of the commissioning work will be summarised and the prospects of the studies on the measurement of the top quark mass will be reviewed.

Chapter 1

Top Quark Physics

The Standard Model of particle physics (SM) [1,2,3,4,5,6,7,8] is a Quantum Field Theory (QFT) and as such incorporates the principles of quantum mechanics and relativity. It gives a description of all the observed elementary particles and their interactions via three of the four known fundamental interactions, the weak, the strong and the electromagnetic interaction, leaving out gravity (see Table 1.1[1]). Experimental data of the past decades are in agreement with the standard model at the order of $\mathcal{O}(10^{-3} - 10^{-8})$ depending on the observable [9] and the model therefore is regarded as one of the best-tested theories. However, it does show some shortcomings. For instance, it intrinsically does not include gravity and therefore has always merely been looked at as an effective theory. Also, the generation of mass is not explained by the standard model, the particle masses are merely accommodated as free parameters. Furthermore, experimental data, especially the observed oscillations, and thereby the massive character of neutrinos which is not predicted within the standard model, point towards physics beyond this model. Several frameworks of theories beyond the standard model have been developed, namely its super symmetric extension (SUSY) [10, 11, 12] and several other theories such as the String Theory [13].

1.1 A Reminder: The Standard Model of Particle Physics

The standard model is a specific QFT based on the gauge group $SU(3)_c \times SU(2)_L \times U(1)_Y$ and involves the fields representing the fermions, the gauge fields and the scalar Higgs field. The fundamental basis of this QFT is the principle of requiring *local gauge invariance* and renormalisability of its Lagrangian. The Lagrangian describes the dynamics of the model and can be written as:

$$\mathcal{L}_{SM} = \mathcal{L}_{Gauge} + \mathcal{L}_{Matter} + \mathcal{L}_{Yukava} + \mathcal{L}_{Higgs}$$

Where $\mathcal{L}_{Gauge}$ describes the gauge fields and their interactions, the fermions and their interactions with the gauge fields are described by $\mathcal{L}_{Matter}$. Respectively, $\mathcal{L}_{Yukava}$ describes the interactions of the fermions with the Higgs field, the energy of which is then described by $\mathcal{L}_{Higgs}$.

[1]Throughout this paper, a system of units is utilised where the speed of light and Planck's constant are set to unity, $\hbar = c = 1$. Energies, momenta and masses are hence all given in units of eV.

		Electric charge	Mass	Forces		
				strong	em.	weak
quarks (fermions)						
up quark	(u)	$2/3\,e$	$1.5 - 3.3$ MeV	✓	✓	✓
down quark	(d)	$-1/3\,e$	$3.5 - 6.0$ MeV	✓	✓	✓
strange quark	(s)	$2/3\,e$	104^{+26}_{-34} MeV	✓	✓	✓
charm quark	(c)	$-1/3\,e$	$1.27^{+0.07}_{-0.11}$ GeV	✓	✓	✓
top quark	(t)	$2/3\,e$	171.2 ± 2.1 GeV	✓	✓	✓
bottom quark	(b)	$-1/3\,e$	$4.20^{+0.17}_{-0.07}$ GeV	✓	✓	✓
leptons (fermions)						
electron	(e)	$-e$	$0.510998910 \pm 0.000000013$ MeV	-	✓	✓
electron neutrino	(ν_e)	0	< 2 eV	-	-	✓
muon	(μ)	$-e$	105.658367 ± 0.000004 MeV	-	✓	✓
muon neutrino	(ν_μ)	0	< 0.19 MeV	-	-	✓
tau	(τ)	$-e$	1776.84 ± 0.17 MeV	-	✓	✓
tau neutrino	(ν_τ)	0	< 18.2 MeV	-	-	✓
gauge bosons						
gluon	(g)	0	0 (theory)	✓	-	-
W boson	$(W^\pm)$	$\pm e$	80.398 ± 0.025 GeV	-	✓	✓
Z boson	(Z^0)	0	91.1876 ± 0.0021 GeV	-	-	✓
photon	(γ)	0	$< 1 \cdot 10^{-18}$ eV	-	✓	-

Table 1.1: Some properties of quarks, leptons and the force mediating bosons [9].

1.1.1 Electroweak Interactions

As one part of the standard model, Glashow, Weinberg and Salam found the unification of the weak and the electromagnetic interaction into one *electroweak* theory. It is based on the gauge symmetry group $SU(2)_L \times U(1)_Y$ [1, 2, 3]. The emerging fermion field can be written as the (lefthanded) weak isospin doublets carrying weak charge:

$$\ell_L = \begin{pmatrix} \nu_e \\ e^- \end{pmatrix}_L \quad \begin{pmatrix} \nu_\mu \\ \mu^- \end{pmatrix}_L \quad \begin{pmatrix} \nu_\tau \\ \tau^- \end{pmatrix}_L$$

$$q_L = \begin{pmatrix} u \\ d \end{pmatrix}_L \begin{pmatrix} c \\ s \end{pmatrix}_L \begin{pmatrix} t \\ b \end{pmatrix}_L$$

The corresponding weak gauge bosons of $SU(2)_L$ being the $\mathrm{W}^\pm$ and Z^0.
For the quark eigenstates there is a mixing between the mass eigenstates of the three generations and thus the weak eigenstates are linear combinations of the different states. The mixing was described by Cabbibo, Kobayashi and Maskawa in a 3×3 matrix (CKM-Matrix) [14, 15]. For the leptons however there is no equivalent mixing in the standard model. The experimentally found massive character of the neutrinos which is not described within the standard model, results in a mixing matrix for neutrino flavours, too. Hence only eigenstates of the charged leptons remain unmixed.
In order to include the electromagnetic interaction, all charged particles come with a righthanded singlet of $U(1)_Y$,

$$\ell_R \quad = \quad e_R \quad \mu_R \quad \tau_R$$

$$q_R \quad = \quad \begin{cases} u_R & c_R & t_R \\ d_R & s_R & b_R \end{cases}$$

the corresponding gauge boson being the photon (γ). Whereas the latter is massless, the three weak bosons were observed to be massive [16, 17]. This observation and also the massive character of the fermions is not a feature of the pure standard model has to be accommodated via an additional mechanism, the Higgs Mechanism [18]. An additional field is introduced as a scalar doublet

$$\Phi = \begin{pmatrix} \Phi^+ \\ \Phi^0 \end{pmatrix}$$

The elektroweak symmetry is spontaneously broken by the non-zero vacuum expectation value of Φ and thereby the three weak gauge bosons acquire mass.
Via the Yukawa coupling the fermion fields interact with Φ, which explains their massive character.

1.1.2 Strong Interactions

The second component of the standard model besides the electroweak theory is Quantum Chromo Dynamics (QCD) [19,20]. It is a gauge field theory based on the symmetry group $SU(3)_c$ giving a description of the strong interaction between the colour charged quarks and gluons. The gauge bosons of the non-Abelian group, the eight gluons, are massless but carry colour charge themselves and therefore are subject to self-interaction in 3-gluon and 4-gluon vertices.
A specific feature of QCD is its distinct behaviour at low and at high energy scales or at large and at small distances, accordingly. The coupling constant of QCD, α_s, is dependent on the transferred momentum in the interaction. QCD predicts that α_s decreases with increasing momentum transfer, and vanishes at asymptotically high energies (cf. Ref. [21] for a recent review); *asymptotic freedom* and *confinement* are the arising phenomena. The former describes the behaviour of quarks in particle interactions at high energy scales, where the quarks behave like free particles. A consequence of the latter is that isolated coloured states are forbidden, as the increasing field strength at larger distances leads to the creation of quark-anti-quark pairs out of the vacuum. These then allow for the formation of colour-neutral bound states, the hadrons. Bound states of three quarks, the baryons and the quark-antiquark bound states, the mesons, are indeed the only bound quark states observed so far.
Both, asymptotic freedom and confinement have important consequences for the calculations possible within QCD. Asymptotic freedom causes the strong coupling constant α_s to become small enough that in this regime quantitative predictions of the strong interactions are possible by the application of perturbation theory. At large distances and low momentum transfers (typically $\mathcal{O}(< 1\ \mathrm{GeV}^2)$), respectively, perturbation theory is no longer applicable and non-perturbative methods are needed in order to give quantitative descriptions. Monte Carlo generators (cf. Section 1.3) use models of hadronisation, which describe the fragmentation of quarks and gluons into hadrons. Mainly two methods, the *Lund String Model* [22] and *cluster fragmentation* [23] are applied.

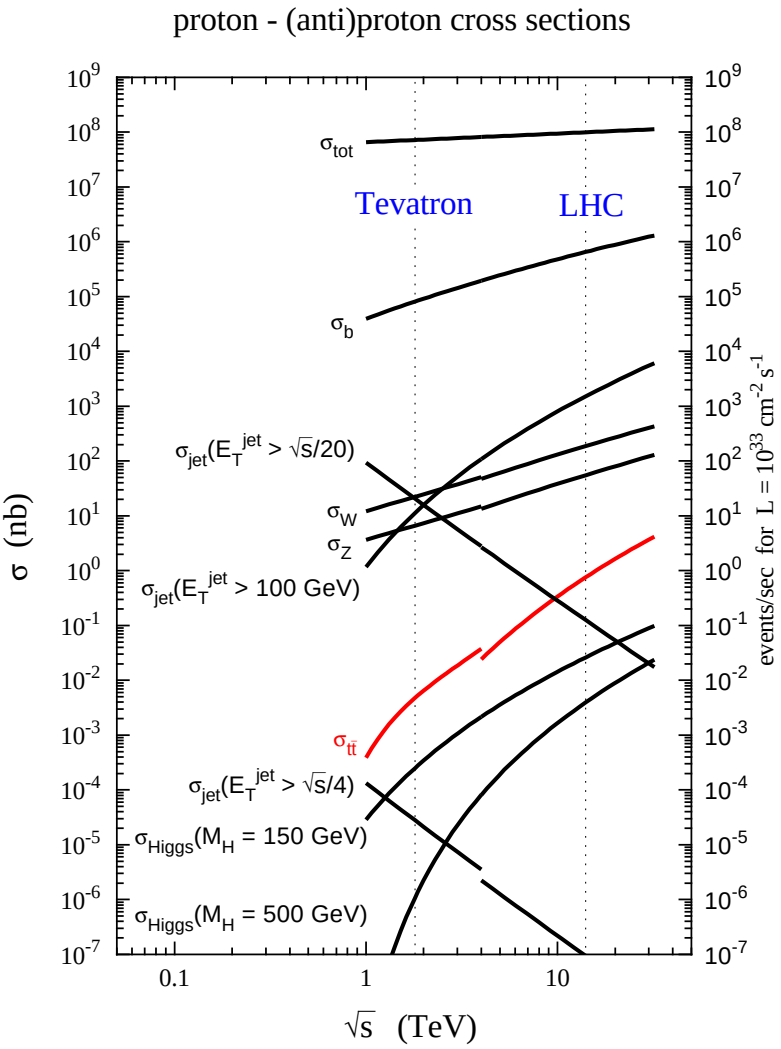

Figure 1.1: Predictions for hard scattering at the TEVATRON and the LHC [24] are shown in the top plot. The $t\bar{t}$ production cross-section is shown in red. The steps in the curves at $\sqrt{s}$ =4 TeV are due to the difference of colliding particles: $p\bar{p}$ scattering at the TEVATRON and pp scattering at the LHC.

LHC pp at $\sqrt{s}$	10 TeV	14 TeV
$\sigma_{t\bar{t}}$ [25]	401.60 pb	883.90 pb
$\sigma_{s-channel}$ [26]	6.627 pb	10.65 pb
$\sigma_{t-channel}$ [26]	124.51 pb	246.6 pb
$\sigma_{Wt-channel}$ [27]	32.66 pb	66 pb

Figure 1.2: The table shows calculated cross-sections for top quark pair and single top quark production at the LHC at different centre-of-mass energies. $\sigma_{t\bar{t}}$ is calculated at NLO with NLL corrections. The PDF-set used is CTEQ6.6 and the assumed top quark mass m_t = 172.5 GeV [25]. Single top cross-sections are calculated at LO and scaled to theoretical NLO cross-sections. 10 TeV cross-section was calculated at NLO using MCFM, the PDF-set used is CTEQ6M and the assumed top quark mass m_t = 172 GeV [28].

1.2 Top Quark and its Role

The analysis of data from electroweak measurements has shown that a weak-isospin 1/2 and charge +2/3 particle in the mass region of 170 GeV had to exist, if the data were to be compatible with the standard model [29]. Even though none of its quantum numbers have been directly measured, the top quark discovered in 1995 [30, 31] is *the* candidate. The comparison of the predicted cross-section and the values measured at TeVatron are consistent with it being a spin 1/2 and colour triplet particle.
Elektroweak precision measurements at the Z^0 pole especially in the Z^0 $b\bar{b}$ vertex had already shown compelling evidence for the existence of a weak-isospin partner of the b quark [32]. The prediction of the top quark mass has impressively illustrated the standard model's predictive power and is regarded as one of the standard model's great successes. Recent fits of electroweak data still are in very good agreement with the world average of the direct measurement of the top quark mass (see Sec. 1.2.3).
Within the family of quarks, the top quark seems to play a prominent role. With a mass of 173.1[2] GeV [33] it is very close to the scale of electroweak symmetry breaking and the question arises whether the top quark might have a more fundamental position within the standard model. Furthermore, it might be a point of manifestation of beyond-standard-model-physics, which e.g. would appear in anomalies of the top quark production and decay.
In addition, its width Γ_t of about 1.4 GeV manifests itself in an extremely short lifetime which leads to unique possibilities of analysis. In particular, Γ_t is smaller than the energy scale of hadronisation - this means that the top quark decays before having time to form bound states or hadronise. In contrast to the case of all lighter quarks, the observation of top quark decays thus allows for a direct study of its weak decay. Also, the spin information is completely transferred to the decay products of the top quark as the timescale for depolarisation $m_t/\lambda_{QCD} \gg 1/\Gamma_t$ is bigger than the available decay time [34].

1.2.1 Top Quark Production

Perturbative QCD offers the means to calculate the production cross-section of $t\bar{t}$ pairs in hadron accelerators such as the TeVatron or the LHC. The description of these collisions can be divided into a short distance part, the hard scattering process of the partons forming the proton, and a long distance part, which is represented by the Parton Distribution Functions (PDFs). The PDFs are not calculable from first principles, but rather are the result of global fits to experimental data, in particular of deep-inelastic scattering experiments [35, 36, 37, 38, 39, 40]. The PDF $f_i(x_i, \mu_F^2)$ describes the probability density for a parton of flavour i, to carry the longitudinal momentum fraction x_i of the incoming parton, where μ_F^2 is the probing scale.
The cross-section of the hard process (cf. Fig. 1.1, 1.3) in turn is a function of the effective centre of mass energy squared $\hat{s}$, the top quark mass[3] and the strong coupling constant α_s at the scale μ. Thus the $t\bar{t}$ production cross-section can be written as:

$$\sigma_{t\bar{t}}(\sqrt{\hat{s}}, \mathrm{m_t^2}) = \sum_{\mathrm{i,j=q,\bar{q},g}} \int \mathrm{dx_i dx_j f_i}(\mathrm{x_i}, \mu^2)\mathrm{f_j}(\mathrm{x_j}, \mu^2) \cdot \hat{\sigma}^{\mathrm{ij}\to\mathrm{t\bar{t}}}(\sqrt{\hat{\mathrm{s}}}, \mathrm{m_t^2}, \mathrm{x_i}, \mathrm{x_j}, \alpha_\mathrm{s}(\mu^2), \mu^2) \quad (1.1)$$

[2] current world average of direct measurements
[3] N.B. The determination of the production cross-section allows for an indirect measurement of m_t

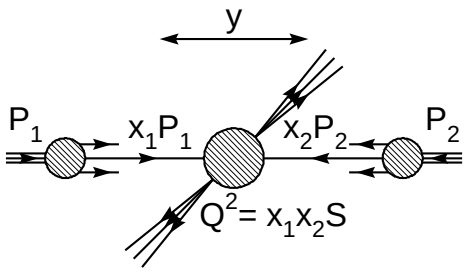

Figure 1.3: Hard scattering process of two partons carrying the momentum fraction x_1, x_2 of the protons P_1, P_2 respectively, which were colliding at a centre of mass energy S. The transferred momentum Q^2 produces a final state which is then moving with rapidity y.

Whereas in the case of TEVATRON the PDFs for the quarks are dominant, at LHC the gluon PDFs dominate. This is why for the latter the relevant $t\bar{t}$ production processes mainly go via gluon-gluon fusion (cf. Figure 1.4).

The production of single top quarks, on the other hand, is an electroweak process.

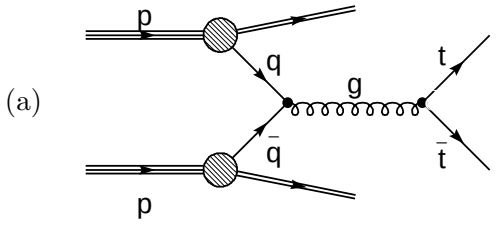

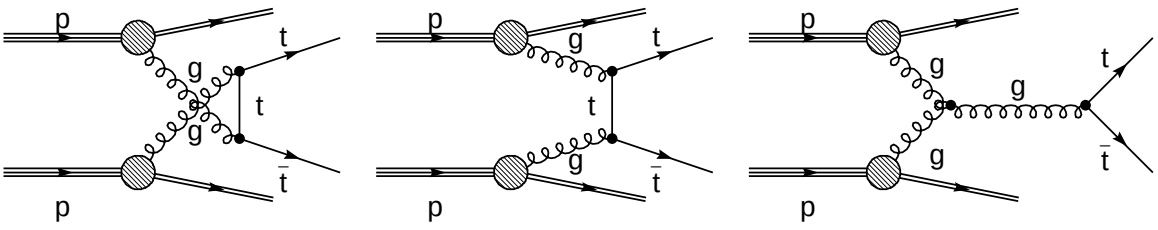

Figure 1.4: Top quark pair production via the strong interaction. Processes at lowest order through quark-anti-quark annihilation (a) and gluon fusion (b).

At tree level there are three different processes: the W-gluon fusion (t-channel) process, Wt production and quark-anti-quark annihilation (s-channel). The respective Feynman diagrams are shown in Figure 1.5.

As shown in the table of Figure 1.2 the total cross-section of the single top quark production (σ_t) is at the level of $\simeq 40\%$ of $\sigma_{t\bar{t}}$. This means that weak and strong interaction are almost equally strong at order (m_t^2), which is a surprising feature. The single top quark production

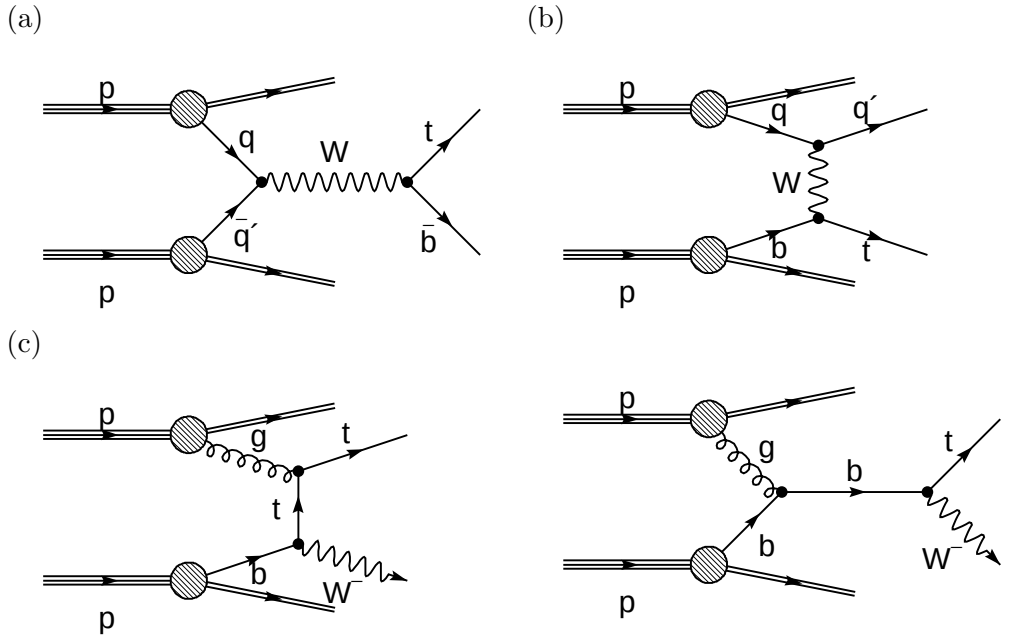

Figure 1.5: Feynman diagrams for the electroweak single top quark production at tree level: (a) s-channel or W^* process, (b) t-channel, (c) Wt production.

thus will be a background to the analysis of the $t\bar{t}$ decay channel.

1.2.2 Top Quark Decay

The top quark decays via the electroweak channel $t \to W q_d$ where q_d denotes a down-type quark and predominantly is a b quark (see 1.6). The corresponding CKM matrix element is $|V_{tb}| = 0.9990 - 0.9993$. In contrast $|V_{ts}| = 0.037 - 0.044$ and $|V_{td}| = 0.004 - 0.014$ [9] illustrate the drastic suppression of Ws or $W\,d$ final states.

As briefly mentioned above, the decay of the top quark is of unique character due to its very short lifetime; no bound states involving top quarks as constituents are known.
At lowest order, setting $M_W = m_b = 0$ and $|V_{tb}| = 1$ the top quark decay width can be written as [41]:

$$\Gamma_0 = \frac{G_F m_t^3}{8\pi\sqrt{2}} = 1.76 \text{ GeV} \tag{1.2}$$

Including higher order QCD and W corrections one achieves $\Gamma(t \to Wb)/\,|V_{tb}| \approx 0.87\Gamma_0 = 1.42$ GeV. Compared to the scale of hadronisation $\lambda_{QCD} \approx 0.22$ GeV [9, 34] Γ_t is small and therefore the study of top quark decays does not involve hadron spectroscopy but rather offers a direct observation of the weak decay. The topology of the observed final states then depends on the decay of the W (see 1.6). It can decay into lepton pairs of all three generations ($\ell\nu_\ell$) and quark pairs of the first two generations ($q\bar{q}'$) for all three different colour states. A decay into the third quark generation is strongly suppressed by the corresponding CKM matrix elements and in the case of the top quark kinematically not possible.

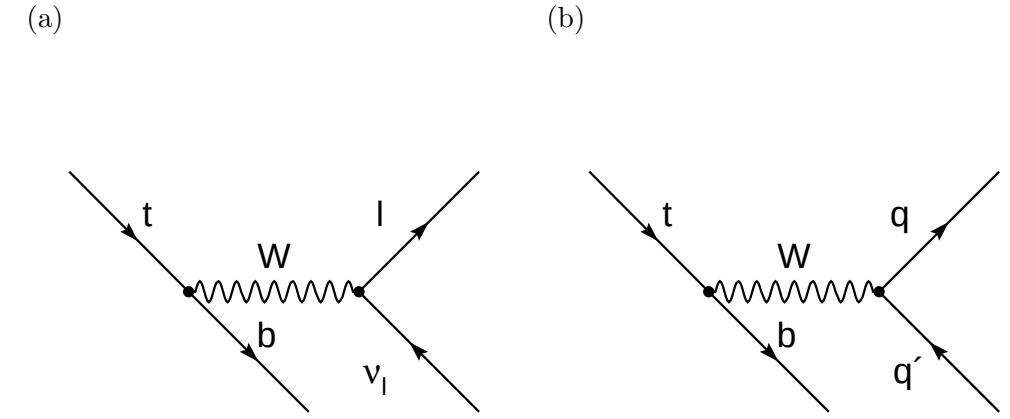

Figure 1.6: Feynman diagram for the decay of a top: (a) leptonic channel, (b) hadronic channel.

Again taking into account only the decay $t \to Wb$ one classifies three groups of decays [9]:

$$\begin{array}{lll} t\bar{t} \to W^+b\,W^-\bar{b} \to q\bar{q}'b\,q\bar{q}'\bar{b} & (46.2\%) & \text{[all-jets]} \\ t\bar{t} \to W^+b\,W^-\bar{b} \to q\bar{q}'b\,\ell\bar{\nu}_\ell\bar{b} & (43.5\%) & \text{[lepton+jets]} \\ t\bar{t} \to W^+b\,W^-\bar{b} \to \bar{\ell}\nu_\ell b\,\ell\bar{\nu}_\ell\bar{b} & (10.3\%) & \text{[di-lepton]} \end{array}$$

At Born level[4] in 1/3 of the events the W decays to a $\ell\nu$ pair and in 2/3 of the events into $q\bar{q}'$ pair. The corresponding branching ratios are listed below[5] [9]:

	Born level	measured
$W^+ \to e^+\nu_e$	1/9	$10.72 \pm 0.16\%$
$W^+ \to \mu^+\nu_\mu$	1/9	$10.57 \pm 0.22\%$
$W^+ \to \tau^+\nu_\tau$	1/9	$10.74 \pm 0.27\%$
$W^+ \to q\bar{q}'$	6/9	$67.96 \pm 0.35\%$

where q denotes an up or a charm quark and q' denotes a down, strange or a bottom quark.

1.2.3 Top Quark Mass

One of its fundamental properties, besides the quantum numbers, is the mass of the top quark. From the viewpoint of theory, the mass of a quark is convention-dependent and in the case of the top quark can differ by 10 GeV [41] - thus the relation of experimentally determined quality to the theoretical parameter m_t is of importance.
In the perturbative top quark propagator the single particle pole defines the top quark mass

[4] Born level is the lowest order at which the hard process contributes to any observable. Here $3+2\cdot3 = 9$ different fermions pairs are possible with equal rate, yielding a branching ratio of 1/9 for each.

[5] and equivalent for the W^-.

via $m_t^* = m_t - i\Gamma_t/2$. Mass measurement based on the reconstruction of the top quark decay products should be regarded as a measurement of the top quark pole mass [41] as mass reconstruction procedures mainly use comparisons of measured data with Monte Carlo simulations. These Monte Carlo simulations often are based on leading order calculations, which are not sensitive to mass renormalisation at all. In addition, the concept of the invariant mass of a top quark decay is prone to large non-perturbative corrections of relative order λ_{QCD}/m_t, as the loss or gain of a soft particle changes the invariant mass. These corrections are at the same magnitude as for the pole mass itself.
Besides the pole mass the top quark $\overline{MS}$ mass $\bar{m}_t(\mu)$ is often mentioned, but as it is not accessible with the presented measurements and its definition is rather complex and subtle, $\bar{m}_t(\mu)$ is not further detailed here and the reader is referred to the discussion in [41].
In the standard model, m_t appears in the top quark Yukawa coupling:

$$y_t(\mu) = 2^{2/3}\sqrt{G_F}m_t(1 + \delta_t(\mu)),$$

where $\delta_t(\mu)$ denotes radiative corrections.
The top quark mass thus enters the electroweak precision observables via quantum effects as an input parameter. This strong dependence of the standard model's loop corrections on the top quark mass and the excellent understanding of electroweak precision measurements had made it possible to predict the value of the top mass with impressive accuracy before the actual experimental observation of the direct decay and thereby its discovery. The latest fit of electroweak data results in $m_{top} = 178.9^{+11.7}_{-\ 8.6}$ GeV [42, 43, 44]. This is in very good agreement with the current world average of direct measurements of $m_{top} = 173.1 \pm 1.3$ GeV [33].
In addition, m_t also plays a prominent role in the indirect measurements and constraints for the mass of a Higgs boson. The standard model Higgs as well as the lightest Higgs in the minimal-super-symmetric standard model (MSSM) strongly depend on the top quark mass as shown in Figure 1.7.

1.3 Monte Carlo Generators

Based on the precise calculations of the standard model processes, several programs have been developed in order to calculate the matrix elements of the scattering events at tree level and up to next-to-leading-order in perturbation theory. Some programs also give a model for the parton showering and hadronisation processes. Only a brief summary of those programs used within this paper will be given here, however, a more detailed overview can be found in [46].

Herwig [23] and Pythia [22] both are packages which allow a full event simulation, covering the initial hard scattering process, parton showering and hadronisation and the subsequent decays of the unstable hadrons as well as the underlying event[6].

Herwig uses the parton-shower approach for initial- and final-state QCD radiation, including colour coherence effects and azimuthal correlations both within and between jets. In its treatment of the subsequent decay of unstable resonances, it includes full

[6] In a hard scattering process, the underlying event has a hard component (initial + final-state radiation) and a soft component (beam-beam remnants).

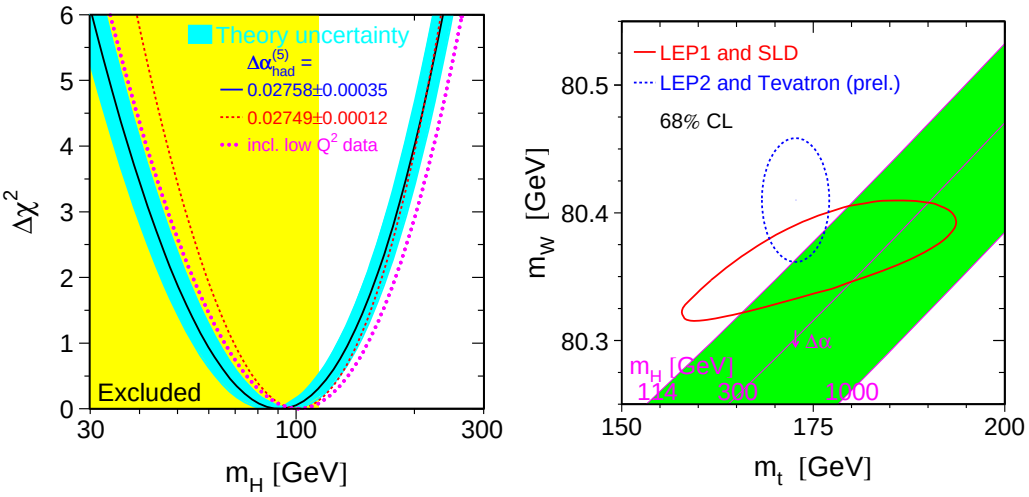

Figure 1.7: Blue-band plot (left), mass of the Higgs boson, as obtained by using all electroweak precision data. The 95% CL lower limit on the Higgs boson mass from the direct searches [45] is shown in yellow. The right plots shows lines of constant Higgs mass in the plane spanned by M_W vs. m_t. The 68% CL for direct measurement of M_W and m_t is shown in dotted blue, while the red curve shows the 68% CL for indirect measurements from precision electroweak data.

spin correlations for most processes.
It contains most standard model, Higgs and SUSY processes.

PYTHIA is a generator for hadronic events in pp, $p\bar{p}$, e^+e^- and ep collisions. It offers simulation of different subprocesses, initial- and final-state parton showers, the underlying event and hadronisation with the subsequent decays.

Tree Level Matrix Element Generators are packages which are specialised in simulating the hard scatter processes. The kinematic quantities obtained, such as masses and momenta, the spin, the colour connection, and the flavour of initial- and final-state partons are then stored and passed to the above-mentioned full event simulation packages. Here the parton shower models also supply the higher order corrections to the leading order matrix element calculations.

ACERMC [47,48] is dedicated to the generation of standard model background processes in pp collisions at the LHC and includes spin correlations.

ALPGEN [49] is specialised in the generation of standard model processes with final states with large jet multiplicities. It uses the exact LO evaluation of partonic matrix elements, as well as top quark and gauge boson decays with helicity correlations.

MC@NLO [50, 51, 52, 53, 54, 55] uses exact next-to-leading-order calculations of rates for QCD processes at hadron colliders, mainly for the processes $t\bar{t}$ and single-top (s- and t-channel).

The events in MC@NLO are produced with equal weights up-to a sign. Effectively each event carries a weight -1 or +1 to ensure a correct modelling of the full phase

space [7]. It should be pointed out that the negative-weight events in Mc@nlo are of a completely different nature from the negative contributions that appear in NLO computations. In particular, the distributions of the positive- and negative-weight events are separately finite in Mc@nlo and this allows for the generation of sets of events whose weights are all identical, up to a sign. For distributions of any physical observable these weights have to be taken into account as only the sum of the weights is a physical quantity.

In order to consistently combine matrix element descriptions with the parton shower modelling sophisticated matching algorithms have been developed. They assess the problem of possible double counting of configurations with different number of hard partons at the matrix element level but similar reconstructed final states. A final state with n jets could be produced by n partons at matrix element level, each of which is transformed into a jet by the parton shower model, or it could be produced by (n-1) partons at matrix element level, if the parton shower generated an additional jet. An additional source of double counting appears, if a jet is too soft or too forward to be reconstructed.
Two methods have been developed in order to match the generated partons to the reconstructed jets:

CKKW matching [56, 57] The matrix element weights are re-weighted by the use of Sudakov form factors, vetoing regions of the phase space which had been already covered by the parton level configurations.

MLM matching [58, 59] The partons from matrix element calculations are matched to parton jets reconstructed after the perturbative shower. Here the parton level is defined using kinematic variables, i.e. a minimum transverse energy and a minimum separation of the partons is required. In contrast to the CKKW matching, no Sudakov re-weighting is used. The events are showered without a veto on the emission. A cone jet algorithm applied on the final state is used to match the partons to the reconstructed jets. If each parton is matched to a jet, the event matching criterion is fulfilled. If this is not the case, the event is rejected. Also events with additional jets which fail to be match to the partons at matrix element level are rejected.

[7] In the $t\bar{t}$ sample a fraction of 13.5% has negative weight.

Chapter 2

The ATLAS Detector - Design and Performance

In September 2008, a new machine started operation in the existing tunnel of the Large Electron-Positron Collider (LEP) at CERN in Geneva, Switzerland: The Large Hadron Collider (LHC) [60]. This accelerator was designed to provide two counter-rotating proton beams in an unchallenged energy and luminosity range: a centre of mass energy of 14 TeV and a design luminosity for pp collisions of 10^{34} cm^{-2}s^{-1} .
After eight years of construction in a last commissioning step, the first proton beams were successfully circulated in the two directions - however a stable operation with colliding beams was not yet achieved. On September 19$^{\text{th}}$ a faulty interconnect between two of the superconducting dipole magnets caused an incident resulting in an uncontrolled quench and a huge loss of helium in the course of which several magnets were damaged. A repair and modification campaign is underway and the next operation of the accelerator with beams is currently scheduled for fall 2009. The physics motivation as well as the requirements for appropriate detectors shall briefly be reviewed in this chapter.

2.1 The pp Collider Ring LHC

After being produced in a proton source[1], protons are bunched and accelerated in different steps as sketched in Figure 2.1. The first element of the LHC accelerator chain is the LINAC (LINear particle ACcelerator) providing 50 MeV protons, which in a second step are brought up to 1.4 GeV in the Proton Synchrotron Booster (PSB) and to 26 GeV in the Proton Synchrotron (PS). The last step of pre-acceleration is done in the Super Proton Synchrotron (SPS) out of which the two LHC beam pipes are filled with protons at a nominal injection energy of 450 GeV. In the 26.7 km long tunnel two super-conducting radio-frequency (400.8 MHz) cavity modules per beam ensure the final acceleration up to 7 TeV per beam. Super-conducting dipole magnets with a field of up to 8.3 T store the protons in the two rings. In 2,835 bunches, each consisting of up to 10^{11} protons, with a bunch spacing of 25 ns an energy of 334 MJ is stored.
Four independent experiments are set up at the four interaction points, where the beam

[1] By ionisation of hydrogen gas.

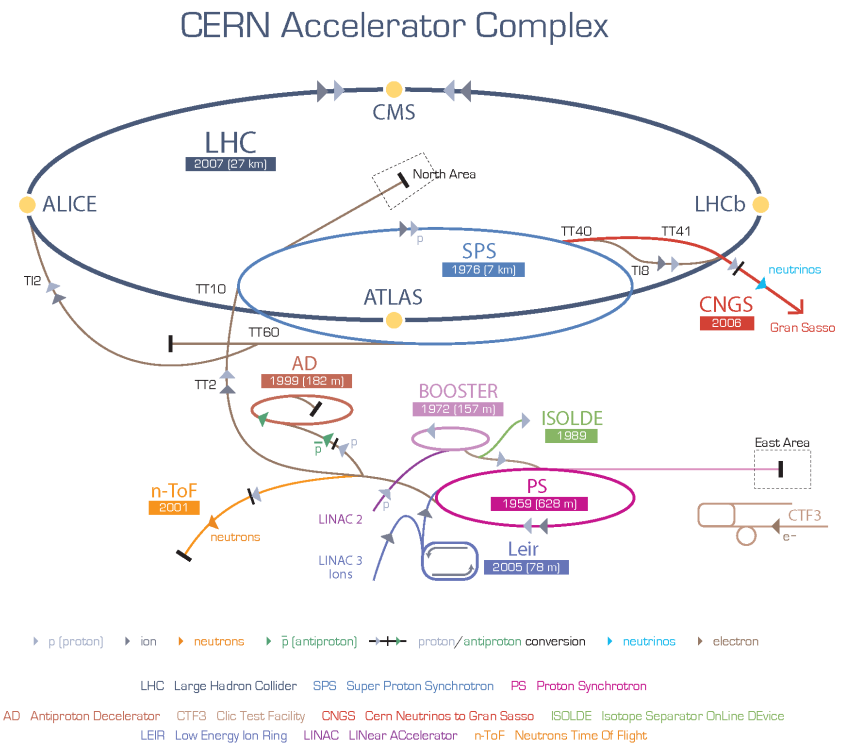

Figure 2.1: Schematic view of the chain of accelerators at CERN [61].

pipes intersect and the beam is focused. At a diameter of 16.6 μm, the proton bunches are brought to collision with a frequency of 40 MHz. The design luminosity for pp collisions being 10^{34} cm^{-2}s^{-1} one expects an average of about 23 inelastic collisions per bunch crossing and hence experiments will have to deal with a significant number of minimum bias events[2] and thus pile-up noise.
Of the four LHC experiments, two are devoted to specialised physics tasks: ALICE (A Large Ion Collider Experiment) was designed for studies in heavy ion physics and to possibly observe quark-gluon plasma [62]; while LHC-b is a spectrometer dedicated to b quark physics especially for studying CP violation [63]. Apart from these two specialised detectors, CMS (Compact Muon Solenoid) [64] and ATLAS (A Toroidal LHC ApparatuS) [65] are the two multipurpose detectors which were designed to cover a broad field of physics measurements.

2.2 Physics and Performance Goals for ATLAS

Both with its collision energy and its event rates for processes of interest, the LHC gives access to unchallenged kinematic regions. A vast field for new physics is thus accessible [60].

[2]Minimum bias events are events in which the colliding partons transfer only little transverse momentum. These events show a minimum activity in the detector and thus do not trigger the trigger system.

- LHC will allow to enter the parameter space of theories extending the SM. An example is super-symmetry [10] the lightest stable particle of which would also provide a candidate for dark matter, provided R-parity is conserved. But also Extra Dimensions [66] and Grand Unified Theories [67], theories predicting the production of new heavy gauge bosons W' and Z' as well as flavour-changing neutral currents and lepton flavour violation have been proposed. Many particles and phenomena predicted by these theories are in the kinematic range of LHC and can thus either be confirmed or excluded with LHC data.
- High rates of central parton-parton collisions at new energies will give excellent possibilities for testing Quantum Chromo Dynamics (QCD) and allow the search for a potential quark sub-structure which would manifest itself by deviations in the jet cross-sections from the QCD expectations.
- Even in the start-up phase at low-luminosity running, LHC will a be a good top-quark 'factory', providing tens of tops per second and thus allowing measurements of the top quark mass, its spin and its couplings. For example the Cabibbo-Kobayashi-Maskawa matrix element $|V_{tb}|$ will be accessible in the $t\bar{t}$ and the single top production cross-section measurements.
- The Higgs boson searches both in standard model [3, 18, 68] and beyond standard model channels are of high priority and have been used as a benchmark for the performance requirements of detector subsystems.

However, the experimental environment of the LHC is rather hostile than trivial as the high inelastic proton-proton cross-section of 80 mb will produce a total rate of 10^9 inelastic events per second at design luminosity. Both the high rate of minimum bias events and the fact that QCD jet production cross-sections dominate over the rare processes of interest aggravate the experimental measurements. This implies the necessity of high integrated luminosity, a sophisticated trigger system and the possibility to precisely measure the momentum and energy as well as a good particle identification in the detectors in order to reliably reconstruct the final states of the processes of interest.

Detector component	**Required resolution**	**η coverage**	
		Measurement	Trigger
Tracking	$\sigma_{p_T}/p_T = 0.05\%\ p_T \oplus 1\%$	± 2.5	
EM calorimetry	$\sigma_E/E = 10\%/\sqrt{E} \oplus 0.7\%$	± 3.2	± 2.5
Hadronic calorimetry (jets)			
barrel and end-cap	$\sigma_E/E = 50\%/\sqrt{E} \oplus 3\%$	± 3.2	± 3.2
forward	$\sigma_E/E = 100\%/\sqrt{E} \oplus 10\%$	$3.1 < \lvert\eta\rvert < 4.9$	$3.1 < \lvert\eta\rvert < 4.9$
Muon spectrometer	σ_{p_T}/p_T=10% at p_T = 1 TeV	± 2.7	± 2.4

Table 2.1: General performance goals of the ATLAS detector [65]. The units for E and p_T are in GeV.

2.3 The ATLAS detector

In order to study the aforementioned final states, the following *physics objects* need to be reconstructed and thus define the required precision of the detector (cf. Tab. 2.1):

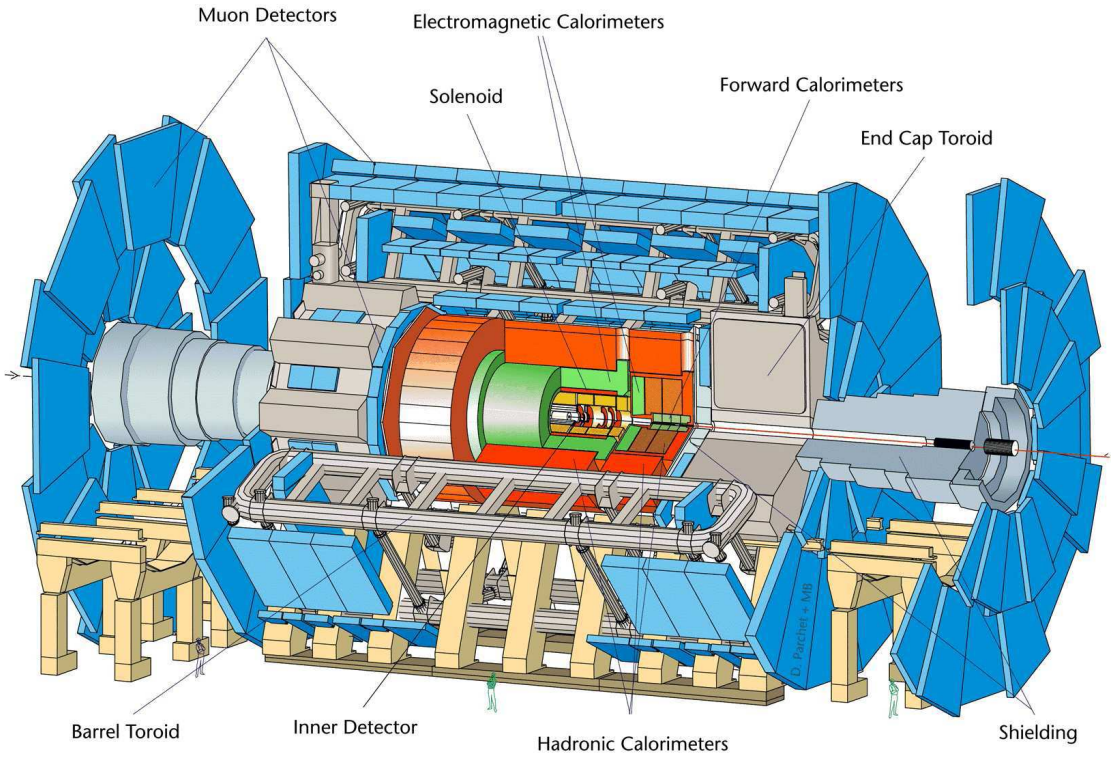

Figure 2.2: Schematic view of ATLAS, one of the multipurpose detectors at LHC. A description is given in the text.

Muons as charged particles leave a track in the inner detector and due to their minimum ionising nature are not absorbed in the calorimeter. Their momentum is thus best measured in the muon chambers.

Electrons also leave a track in the inner detector but are absorbed in the electromagnetic calorimeter where they are also measured in jets.

Photons are invisible to the inner detector and are measured in the electromagnetic calorimeter as clusters.

Jets are the manifestation of scattered partons after undergoing fragmentation and are measured as a collimated set of particles. Their energy and direction is measured in the calorimeters. For the charged particles, a signal in the inner detector makes it possible to combine the calorimeter measurement with tracking.

$\mathbf{E_T^{miss}}$ Particles interacting only weakly can not be measured directly but are indirectly reconstructed as **missing transverse energy** ($E_{\mathrm{T}}^{\mathrm{miss}}$) assuming that the products of the colliding protons are momentum balanced in the transverse plane.

For this purpose the ATLAS detector shown in Figure 2.2 is built out of several sub-detectors with specific tasks. In order to minimise im-precisions due to multiple interactions, tracking is done closest to the interaction point by the *inner detector*. A solenoidal magnet around it delivers the magnetic bending field for the momentum measurement and is hosted in the same cryostat as the adjacent electromagnetic calorimeter. The adjoining hadronic calorimeter serves also as the solenoid's return yoke. The outermost and name-giving detector layer is the muon spectrometer with its toroidal magnets - ATLAS: **A** large **T**oroidal **L**HC **A**pparatu**S**. A short description shall be given in the following sections, an elaborate review of the design, construction and expected performance is given in [65].

2.3.1 ATLAS Coordinate System

The global coordinate system used in ATLAS is oriented and named as follows:

- the origin is defined at the nominal interaction point
- the positive x-direction points towards the centre of the LHC
- the positive y-direction points upwards
- the z-direction points along the beam-line, and is defined such that xyz defines a right-handed orthogonal coordinate system. In ATLAS jargon the z-axis defines the two sides of ATLAS: They are referred to as side A for positive and side C for negative values of z.
- ϕ denotes the azimuthal, and θ the polar angle with regard to the beam-line.

The rapidity y,

$$y = \frac{1}{2} \ln \frac{E + p_z}{E - p_z} \tag{2.1}$$

is invariant under Lorentz boosts along the beam-line. Even though some of the reconstructed physics objects, particularly jets, are massive, it is common in particle physics to use the small mass limit of the rapidity, namely the pseudo-rapidity η. It is defined by:

$$\eta = -\ln \tan(\theta/2). \tag{2.2}$$

η and ϕ thus are natural coordinates for physics objects, and distances in η-ϕ-space are usually given in units of ΔR, defined by:

$$\Delta R = \sqrt{\Delta\eta^2 + \Delta\phi^2}. \tag{2.3}$$

It is useful to define some quantities in the x-y plane (transverse plane) as they then also become invariant under boosts along the beam-line: the transverse momentum p_{T}, the transverse energy E_{T} and the missing transverse energy $E_{\mathrm{T}}^{\mathrm{miss}}$(i.e. the energy balancing the energy distribution of the reconstructed objects in the transverse plane).

2.3.2 Magnet System

Solenoid In order not to compromise the desired calorimeter performance by additional inactive material in front of the calorimeters, the superconducting solenoid magnet shares

a common vacuum vessel with the barrel electromagnetic calorimeter. That way, it is aligned on the beam axis and provides a reasonably homogeneous 2 T axial magnetic field for the inner detector at an operating temperature of 4.5 K, while minimising the material in front of the calorimeters. The iron absorber of the hadronic tile calorimeter serves as its return yoke.

Toroids The bending field for the muon spectrometer is provided by a system of three air-core toroids, each consisting of eight superconducting coils in separate cryostats for the eight barrel coils and in a common cryostat for each of the endcaps. The magnetic field provided by the toroids is highly non-uniform. The field strength values vary between 0.2 T - 2.5 T for the barrel toroid and 0.2 T - 3.5 T for the endcap toroids, depending on the radial distance to the beam-line and ϕ.

2.3.3 Inner Detector - Tracking System

The inner detector (Figure 2.3) is designed to provide hermetic and robust pattern recognition, excellent momentum resolution and both primary and secondary vertex measurement for charged tracks within the pseudo-rapidity range of $|\eta| < 2.5$. Within $|\eta| < 2.0$ it also provides electron identification. For this purpose it is housed inside the solenoidal magnet which provides the 2 T axial bending field and consists of three sub-detectors: the two precision tracking detectors, Pixel and the SCT (Semi Conductor Tracker), which are adjoined by a straw-tube Transition Radiation Tracker, the TRT.

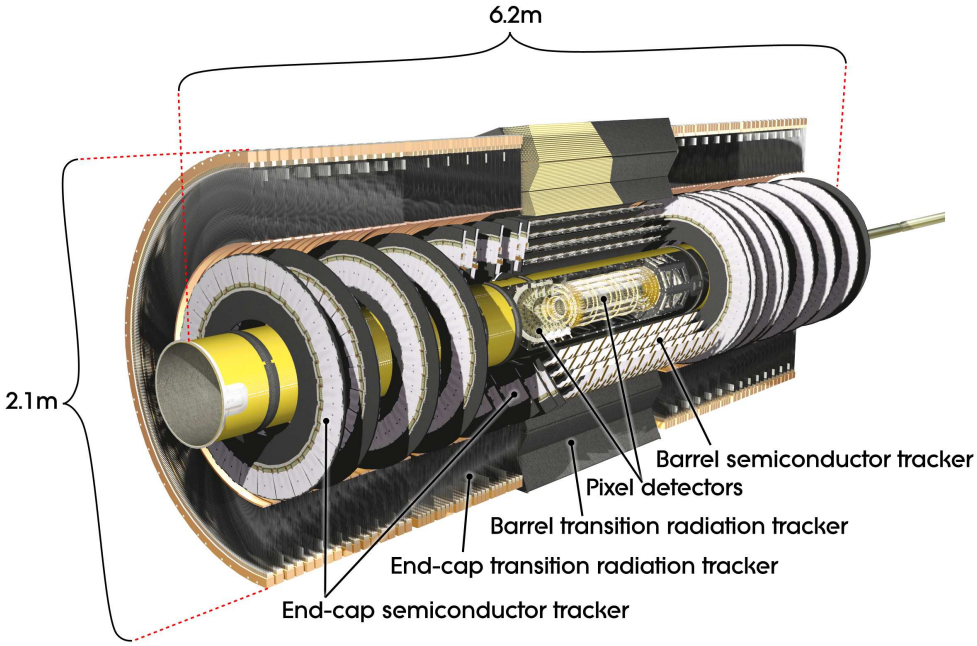

Figure 2.3: Cut-away view of the ATLAS inner detector [65].

Pixel Detector On silicon wavers over 80 million pixel sensors are arranged in three concentric cylinders around the beam axis in the barrel region, while in both endcap

regions they are mounted on three disks perpendicular to the beam axis. The pixel size is $50 \times 400\ \mu\text{m}^2$ and the accuracy achieved by the pixel detector is 10 μm in R-ϕ and 115 μm in z or R in the barrel and endcap region, respectively. This is crucial for precise vertex measurements which in turn are the basis for heavy flavour tagging and τ-identification algorithms as well as minimum bias tagging.

SCT The modules of the SCT are equipped with 80 μm pitch micro-strip sensors on both sides, with a stereo angle of 40 mrad. The modules are arranged in four barrel layers and nine endcap disks on each side and provide a total of 6.3 million readout channels. For single modules at normal incidence, a combined spatial resolution of $\sim$16 μm in R-ϕ was measured in test-beams, which is compatible with the intrinsic accuracy of 17 μm in R-ϕ and 580 μm in z or R per module. The four precision space points measured by the SCT are a fundamental input to track reconstruction.

TRT The TRT consists of more than 350,000 straw-tubes with a diameter of 4 mm, arranged in 73 layers in the barrel, interleaved with fibres and 160 layers in each endcap interleaved with foils. These polypropylene fibres and foils are used as transition radiation material and thus allow for electron identification. The straw-tubes are filled with a $Xe/CO_2/O_2$ gas mixture and are read out with an anode of a gold plated tungsten wire. A charged particle from the interaction point typically traverses 36 straw-tubes. With a single-tube resolution of 130 μm the key task of the TRT thus is an accurate track measurement. Although it only provides R-ϕ information and has a much lower single-point resolution than the silicon detectors, the TRT contributes significantly to the momentum measurement exploiting the higher number of track points and the longer track length.

2.3.4 Calorimeter System

The calorimeter system of ATLAS plays a crucial role in measurements of many physics channels. It provides the means for precision measurements of energy and direction of electrons and photons as well as of quark and gluon jets. In addition, the calorimeter system is designed, to provide fast signals as input for the Level-1 trigger[3](cf. Section. 2.3.6). Sampling calorimeters exploit the fact that the incident particles hitting the absorber material induce a shower of secondary particles. The number of secondary particles produced in the shower is proportional to the energy of the primary particle. The energy deposited by the secondary particles in the active material thus is proportional to the energy of the primary particle ($\text{E} = \alpha \cdot \text{Signal}$). One defines the sampling fraction as the energy deposited in the active material over the sum of energies deposited in active and the absorber material. The so defined sampling fraction is a geometry and material dependent property of the calorimeter and hence varies with geometry and the used material in the different calorimeters. In order to achieve a good energy resolution, a sophisticated calibration procedure including the calibration of the read out electronics and the calorimeter response is necessary (cf. Chapter 3 and 4).
A precise reconstruction of missing transverse energy ($E_{\text{T}}^{\text{miss}}$) is indispensable for the detection of only weakly interacting particles such as the known neutrinos or possible new

[3]The readout channels of the calorimeters are grouped in *trigger towers* with a granularity of $\Delta\eta \times \Delta\phi = 0.1 \times 0.1$ for this purpose.

particles predicted by theories extending the SM.
This calls for a calorimeter system which ensures good containment of electromagnetic and hadronic showers over the whole solid angle of 4π. Therefore, the calorimeter system in ATLAS (shown in Figure 2.4) consists of different hadronic and electromagnetic calorimeters divided into the barrel and the two endcap sections, guaranteeing a hermetic coverage in ϕ and in pseudo-rapidity of up to $|\eta| < 4.9$. The electromagnetic calorimeters contain 22 (24) radiation lengths (X_0) in the barrel (endcap), respectively. Together with the hadronic calorimeters this adds to a total depth of approximately 10 interaction lengths (λ_I). All calorimeters in ATLAS are sampling calorimeters, and depending on the region use appropriate geometry and technology:
The hadronic calorimeter in the barrel and extended barrel region, the so-called Tile, is built as a sandwich of steel absorber plates and plastic scintillators as active material. In the active material scintillation light of the shower particles generates the signal. All other calorimeters in ATLAS use different absorber materials and geometries but commonly use liquid argon as active material and are housed in one cryostat for each region, the barrel, and the two endcaps, respectively. Liquid Argon (LAr) technology was chosen because of its good linearity in a wide energy range, its longterm stability and its radiation hardness. The signal is generated by the incoming particles with an energy above 26.4 eV, which ionise the Argon, i.e. they create electron-ion pairs. In an electric field supplied by the high voltage (HV) system, the electrons then drift towards a readout electrode, where the induced current is measured (a description of the LAr readout electronics will be given in Chapter 3).

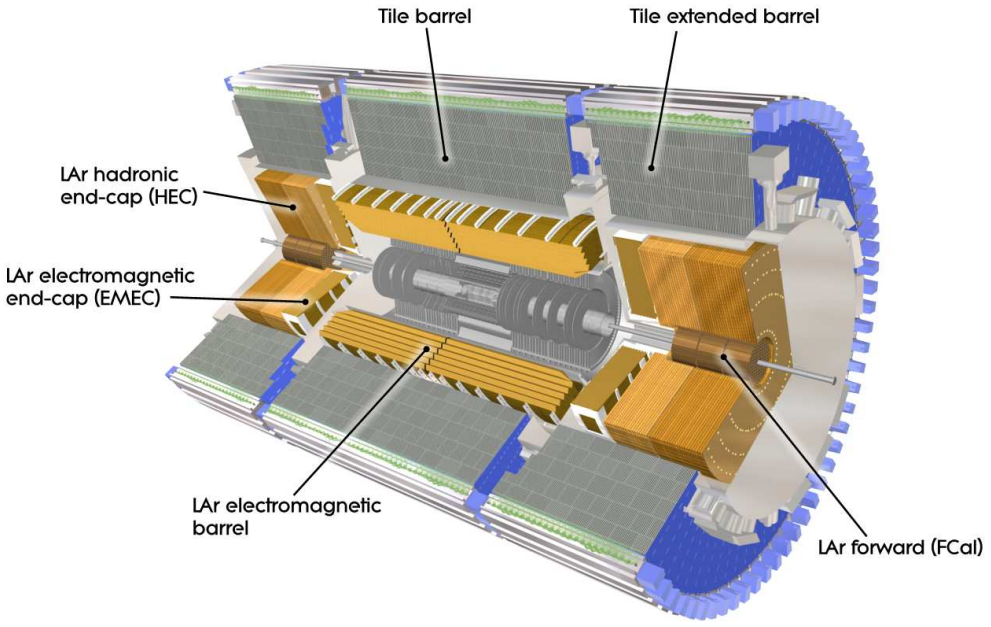

Figure 2.4: Cut-away view of the calorimeter system of ATLAS [65].

The Tile Calorimeter

The tile calorimeter serves as the hadronic calorimeter in the barrel region; it is divided into a central barrel part ($|\eta| < 1.0$) and an extended barrel part ($0.8 < |\eta| < 1.7$). Each of the three parts is built of 64 wedge-shaped modules. Iron is used as absorber material and tiles of plastic scintillator as active material. The signal in the tile calorimeter is generated by scintillation light caused by the shower particles. The scintillator tiles are oriented radially and normal to the beam axis. For regions of small η, where the incident particles hit the scintillator and iron tiles at small angles, the lateral shower fluctuations are large enough to generate the signal, even if the particles trajectory is nearly parallel to the sampling layers. The scintillator tiles are coupled to wavelength-shifting optical fibres, which are grouped in approximately projective geometry in pseudo-rapidity and are read out by photo-multiplier tubes. The passive material being iron allows the tile calorimeter to also serve as a flux return yoke for the central solenoidal magnetic field. Since the signal (scintillation light) is read out by photo-multipliers it has a fast response time. The tile calorimeter has three sampling layers with a granularity of $\Delta\eta \times \Delta\phi = 0.1 \times 0.1$. The containment ranges from 8 to 14 λ_I depending on the η region.
Due to the geometry of the tile calorimeter, the sampling fraction varies with the incident angle of the incoming particles and hence is a function of η. It is in the order of about 3%.

The Liquid Argon Barrel Calorimeter

The central electromagnetic calorimeter in the barrel (EMB) covering $|\eta| < 1.475$ consists of two cylinders, each built from 16 modules. It uses lead as an absorber, which is sandwiched between a 0.2 mm stainless steel foil for mechanical strength. The readout electrodes are kept in position between the absorber by a honeycomb spacer-mat. In order to avoid any discontinuities in the ϕ-coverage and to guarantee a fast signal collection, a complex accordion geometry was chosen (Figure 2.7). The accordion waves are axial and run in ϕ. This way the signals in the different samplings are collected on one electrode and no further summing is necessary.
Housed in the same cryostat, a finely segmented presampler precedes the calorimeter. It acts as an active layer of 11 mm LAr and provides first sampling information, such as to distinguish π^0 and γs. It also helps to correct for the energy losses in the dead material[4] in front of the calorimeters.
Outside of the presampler the barrel has three sampling layers for $|\eta| < 1.35$ and two layers for higher η. The first layer has a granularity as fine as $\Delta\eta \times \Delta\phi = 0.025/8 \times 0.025$ which becomes coarser in the outer layers. The containment of the calorimeter is 24-33 X_0 depending on the η region. In the EMB, the sampling fraction is of the order of 16 - 20%, and as consequence of the accordion geometry varies with ϕ.

The Liquid Argon Endcap Calorimeter

The ElectroMagnetic Endcap Calorimeter (EMEC) is based on the same design as the barrel and covers the region $1.375 < |\eta| < 3.2$. It is hosted in the same cryostat as the

[4] i.e. inactive material of the inner detector, cables, cryostat walls etc., for the barrel typically 1 X_0.

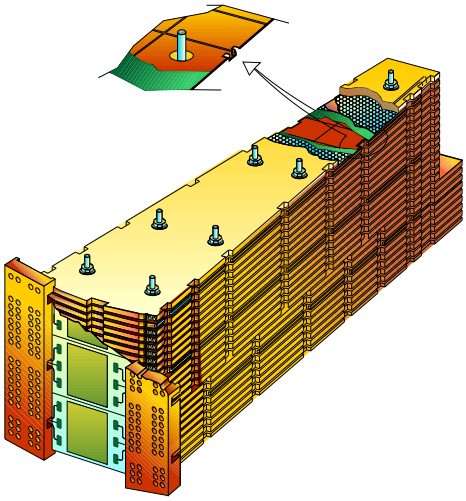

Figure 2.5: Artist's view of one HEC module (ϕ-wedge) [65]. On the back side one can spot the pre-amplification and summing boards and the zoom in shows the readout electrode at the position of a tie rod.

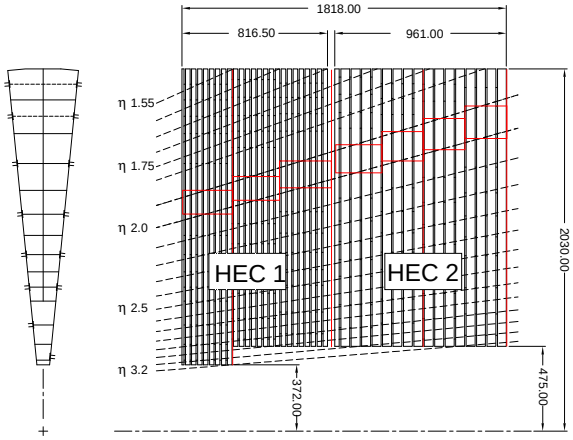

Figure 2.6: Schematic $R-\phi$ (left) and $R-z$ (right) view of the hadronic endcap calorimeter [65]. The semi-pointing layout of the readout electrodes is indicated by the dashed lines, the red lines show the cells in the four samplings. Dimensions are in mm.

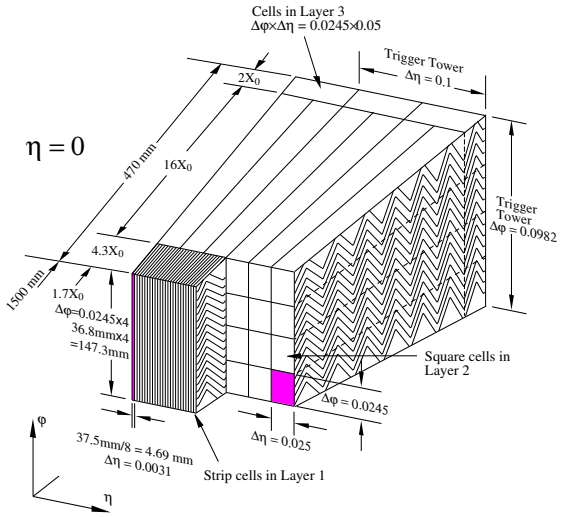

Figure 2.7: Sketch of an EMB module where the different layers are clearly visible with the ganging of electrodes in ϕ. The granularity in η and ϕ of the cells of each of the three layers and of the trigger towers are also shown [65].

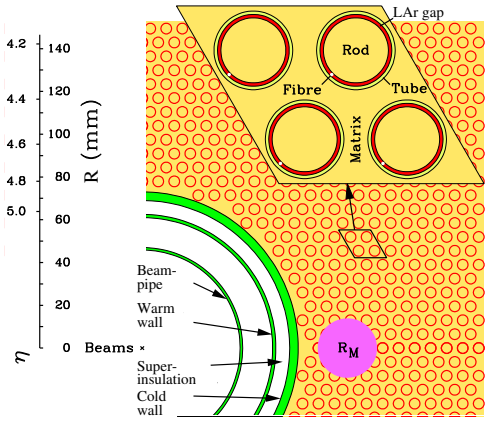

Figure 2.8: Electrode structure of the first FCal module [65]. The copper matrix, tubes and rods with the LAr gaps are shown.

hadronic endcap calorimeter and the forward calorimeter. For the EMEC, the accordion waves are radial and run axially. The absorbers are mounted in a radial arrangement like spokes of a wheel. The EMEC inner and outer coaxial wheels each consist of eight modules. With increasing radius, the accordion wave 'amplitude' and hence also the LAr gap increases. However, the absorber thickness is kept constant. To compensate this, the high voltage has to be varied with the radius.
Dead material in the order of 3-4 X_0 in front of the EMEC require a presampler as first layer in the endcap cryostat as well. It is realised for $1.5 < |\eta| < 1.80$ as a 5 mm LAr active layer and serves the same purpose as in the case of the barrel. Like the barrel, the EMEC has two or three sampling layers depending on η, the granularity varies from $\Delta\eta \times \Delta\phi = 0.025 \times 0.025$ to 0.1×0.1 and the containment reaches from 24 to 38 X_0. The sampling fraction in the EMEC is of the order of 7 - 10% and due to the orientation of the accordion, varies with η.

The Liquid Argon Hadronic Endcap Calorimeter

The region of $1.5 < |\eta| < 3.24$ is covered by the Hadronic Endcap Calorimeter (HEC). As the only calorimeter of ATLAS in a classical geometry, the absorbers of the HEC are realised as flat copper plates. Each HEC is structured in two wheels, HEC1 and HEC2 and is housed in the same cryostat as the EMEC and the forward calorimeter (FCal).
The copper plates which in the case of HEC1 (HEC2) have a thickness of 25 mm (50 mm) are stacked to ϕ-wedges on stainless steel tie rods as shown in Figure 2.5 and 2.6, 32 of which build one wheel. Spacers on the tie rods between the plates guarantee the 24 (16) LAr gaps of HEC1 (HEC2) to be 8.5 mm wide. The LAr gaps are divided into four sub-gaps by the readout and high voltage electrodes as shown in Figure 3.3. In order to achieve fast signal summation and a very low noise level, the HEC readout (cf. Chapter 3) uses pre-amplification and summing electronics in the cold.
The granularity of the four layers of the HEC is $\Delta\eta \times \Delta\phi = 0.1 \times 0.1$ for $|\eta| < 2.5$ and $\Delta\eta \times \Delta\phi = 0.2 \times 0.2$ for $|\eta| > 2.5$. In total, the HEC achieves a containment of 11 λ_I.
The simple geometry in the HEC keeps the sampling fraction constant in each wheel. In the HEC front wheel it is 4.4% and 2.2% in the rear wheel, where the absorber plates are double as thick.

The Liquid Argon Forward Calorimeter

The forward calorimeter (FCal) with its electromagnetic (absorber copper) and hadronic (absorber tungsten) part covers the region of $3.1 < |\eta| < 4.9$ and is hosted in a tube at the centre of the endcap cryostats. In a matrix of the corresponding absorber material, tubes holding the cylindrical electrodes are inserted and form a cylindrical shell LAr gap of 269 to 508 μm depending on the module. The first module of the FCal is electromagnetic, the second and third are hadronic modules.
FCal1 (Figure 2.8) has a readout cell size of $\Delta x \times \Delta y = 3.0 \times 2.6\,\mathrm{cm}^2$, FCal2 has a readout cell size of $\Delta x \times \Delta y = 3.3 \times 4.2\,\mathrm{cm}^2$ and FCal3 of $\Delta x \times \Delta y = 5.4 \times 4.7\,\mathrm{cm}^2$. The three active modules of the FCal add up to a total containment of approximately 210 X_0 and 10 λ.
In the case of the FCal it is difficult to extract the sampling fraction, as the geometry

is not pointing at all and the sampling fraction is strongly dependent on the particles' incident angle, it is in the order of 1%.

Performance of the Calorimeter System

A typical plot of the combined performance of the ATLAS calorimetry system is shown in Figures 2.9 and 2.10. Detailed studies of the performance of the different sub-systems have been performed in test-beam measurements [69, 70, 71, 72, 73, 74, 75, 76]. Calibration constants for the calorimeter response have been derived and used for the validation of Monte Carlo simulations [77], which are used to calibrate the final setup in ATLAS (cf. Section 4.1). In order to correctly reconstruct the energy deposited in the calorimeters, it is important to understand the noise in the calorimeters, especially for the energy reconstruction using topological clusters, which are built using cuts on the signal-over-noise ratio (cf. Section 4.1.1). Figures 2.11 and 2.12 show the electronics and pile-up noise as expected in ATLAS conditions. The plot of the electronics noise already includes the real noise as measured in commissioning studies.

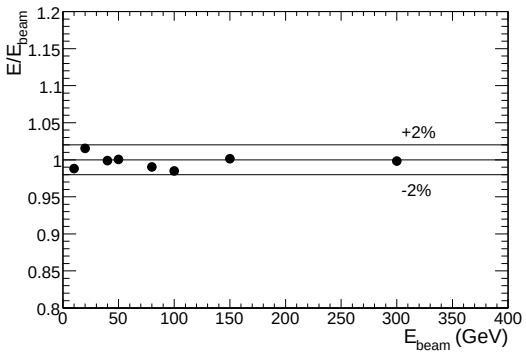

Figure 2.9: Linearity of response as a function of the pion beam energy, E_{beam}, for combined LAr and tile calorimetry at $|\eta| = 0.25$ [65].

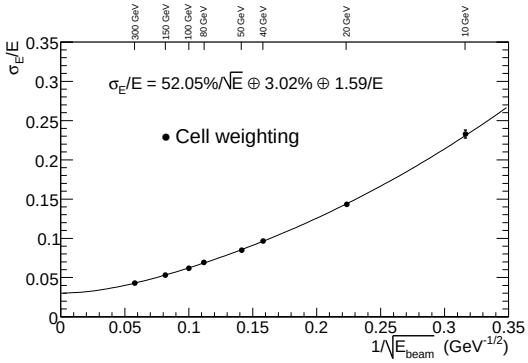

Figure 2.10: Fractional energy resolution obtained for pions as a function of the inverse square root of the beam energy, E_{beam}, for combined LAr and tile calorimetry at $|\eta| = 0.25$. The curve corresponds to the result of a fit to the data points with the functional form as shown [65].

2.3.5 Muon Spectrometer

The muon system (Figure 2.13) is designed to provide muon momentum measurement at excellent precision in the pseudo-rapidity range of up to $|\eta| < 2.7$ as well as a muon trigger signal up to $|\eta| < 2.4$. The performance goal is set to achieve momentum resolution σ_{p_T}/p_T of 10% for 1 TeV. For muons of $\sim$ 100 GeV, this translates into a resolution of the order of 2-3%. The aforementioned toroidal magnet system provides a bending field which is mostly orthogonal to the muon trajectories. Its realisation with superconducting

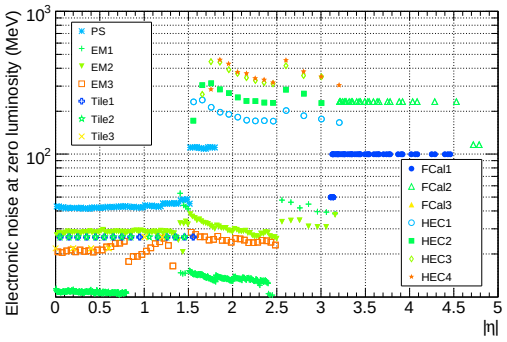

Figure 2.11: Expected electronic noise in individual cells of the various sampling layers of the calorimeters as a function of $|\eta|$ [65].

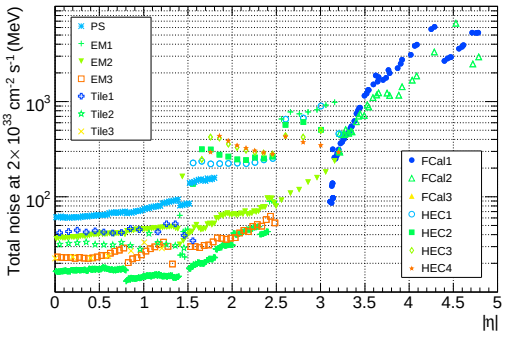

Figure 2.12: Expected noise from the electronics and pile-up at 2×10^{33} cm^{-2} s^{-1} in individual cells of the various layers of the calorimeters as a function of $|\eta|$ [65].

air-core coils mounted on a aluminium support structure minimises the degradation of momentum resolution due to multiple scattering. In order to meet the requirements, the muon system is instrumented with two types of precision tracking chambers and two types of trigger chambers with a timing resolution in the order of a few nano seconds (1.5 - 4 ns). In the barrel region, the chambers are arranged in three cylindrical layers around the beam axis and in each endcap region, the chambers are installed in three layers perpendicular to the beam axis.

Monitored Drift Tube chambers (MDT) The MDTs are equipped with two multilayers of three or four tubes. In total 354,000 drift tubes are mounted on 1,150 chambers. The aluminium tubes with a diameter of 30 mm are filled with an $Ar(93\%)CO_2(7\%)$ gas mixture at a pressure of three bar and read out via a concentric anode wire made of a tungsten-rhenium alloy. At 3,080 V, the maximal drift time is $\sim$ 700 ns and the spatial resolution of a single tube is 80 μm or about 35 μm per chamber.

Cathode Strip Chambers (CSC) In order to deal with the high rates in the innermost layer of the very forward region ($2.0 < |\eta| < 2.7$), multi-wire proportional chambers with strip-segmented cathodes and a higher granularity are used. The resolution of a chamber is 40 μm in the bending plane and about 5 mm in the transverse plane.

Resistive Plate Chambers (RPC) RPCs are chambers with two parallel electrode plates at a distance of 2 mm filled with a $C_2H_2F_4$/Iso-C_4H_{10}/SF_6 mixture. The RPCs are used as trigger chambers and can be operated in avalanche and streamer mode at an electric field of $\sim$ 4.9 kV/mm. They are read out by metallic strips on the outer faces via capacitive coupling. Their spatial resolution is in the order of 10 mm.

Thin Gap Chambers (TGC) TGCs are multi-wire proportional chambers, *thin* because the wire-to-cathode distance of 1.4 mm is smaller than the wire-to-wire distance

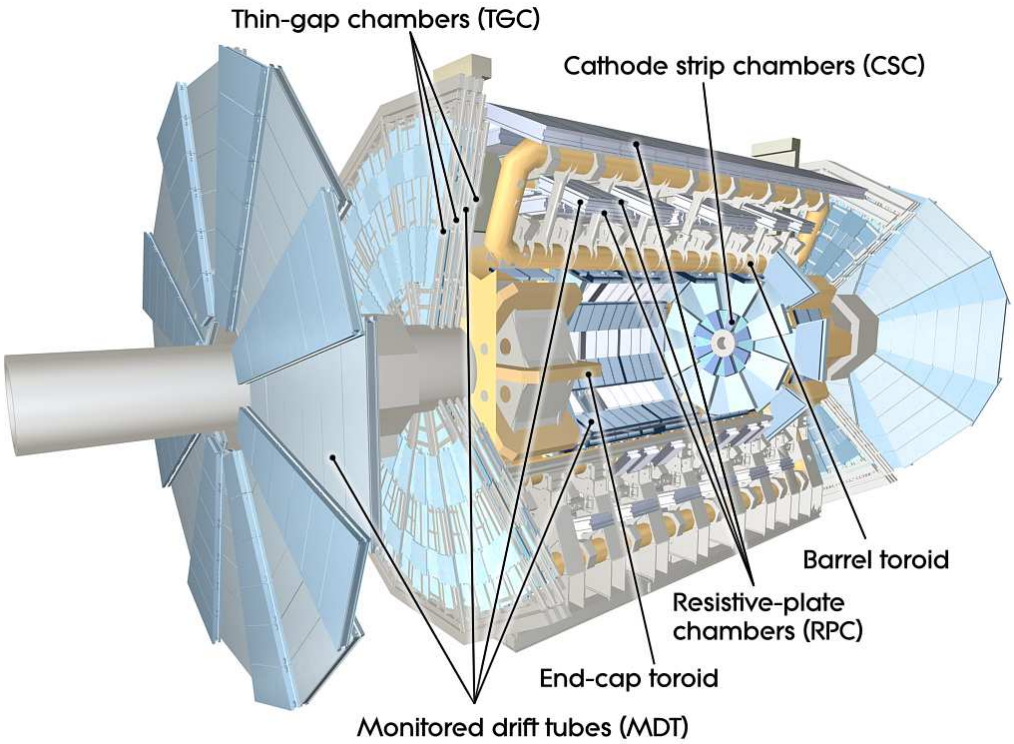

Figure 2.13: Cut-away view of the ATLAS Muon Spectrometer [65]

of 1.8 mm. Their high granularity in combination with a highly quenching gas mixture of CO_2 and n-C_5H_{12} (n-pentane) qualifies them to be used as trigger chambers in the forward region ($1.5 < |\eta| < 2.4$) where they have to cope with a high muon rate. Their spatial resolution is in the order of a few mm.

As trigger chambers, 606 RPC and 3, 588 TGC provide the bunch-crossing identification, a fast muon trigger signal with a well-defined p_T threshold and the track coordinates orthogonal to the ones measured the MDTs and CSCs.
In order to reach the needed momentum resolution, a relative alignment of the precision-tracking chambers in the order of 30 μm and a very good knowledge of the magnetic field is necessary. More than 12,000 optical alignment sensors monitor the internal deformations of the MDT chambers as well as the relative positions of the MDTs and CSCs. A total of 1,800 Hall sensors distributed throughout the muon spectrometer volume is continuously monitoring the field strength. The output of this monitoring system is used to tune a detailed simulation of the magnetic field in order to correctly account for perturbations induced by nearby metallic structures such as the calorimeters.

2.3.6 Trigger

The purpose of the ATLAS trigger system is to reduce the LHC event rate of 1 GHz to a maximal data-taking rate of 200 Hz. In order to reject events which are of no interest to data analysis, the trigger decision is made in three steps: a first hardware-based level (L1)

passes events to the central trigger processor consisting of the level-2 trigger (L2) and the event filter (EF). Each level uses more detailed detector information and selection criteria in order to refine the decision made by the preceding level.

L1 This hardware based trigger uses only reduced information from a subset of detectors, namely information from the entire calorimeter system, however with reduced granularity, as well as data from the muon system trigger chambers. Within a decision time of 2.5 μs it reduces the rate to about 75 kHz by selecting events with high p_{T} leptons or jets as well as events with large $E_{\mathrm{T}}^{\mathrm{miss}}$ or E_{T}. In the selected events the L1 also defines Regions-of-Interest (RoIs), η-ϕ coordinates of those detector regions where the interesting features triggering the selection have been found.

L2 The RoI seeds the selection decision of the L2, which uses all the available detector information within the RoI at full granularity and precision ($\sim 2\%$ of the total event data). With a processing time of about 40 ms per event it reduces the rate to approximately 3.5 kHz.

EF The event filter already uses offline analysis procedures and with a processing time in the order of four seconds achieves a final rate reduction down to 200 Hz. With an event size of approximately 1.3 MB, several hundreds of MB per second are then written to permanent storage.

Chapter 3

Detector Commissioning and Calibration

3.1 Understanding the Detector As-Built

After the assembly and installation of all components in the experimental cavern of ATLAS, it is of vital importance to get a precise knowledge of the performance of the detector *as-built* and understand possible deviations from the expected design performance. The search for dead channels, distorted channels and the validation of the signal calibration, as well as studies of the noise behaviour are examples for the commissioning work. This chapter will give a brief overview of the electronics design and go into detail only on those components which were subject of the studies carried out. In particular, the discussion will focus on the electronics components of the HEC readout. A detailed description of the calorimeter readout electronics design is presented in [78, 65].

3.2 Electronics Readout and Calibration System

The electronics readout chain of the LAr calorimeters consists of the Front End (FE) system [79] of custom design boards, mounted in crates directly on the cryostat feedthroughs (FT) [80], thus being an extension of its Faraday cage, and the Back End (BE) system [81] of VME-based boards, located in an off-detector counting room. Figure 3.1 gives an overview of the different components and their basic elements. The main components of the front end system are:

The Front End Boards (FEBs) [82], on which the calorimeter signals are pre-amplified (with the exception of the HEC, where the pre-amplification is done inside the cryostat before the signals reach the FEBs), shaped and summed to trigger towers. In a pipeline memory on the FEBs the signals await the trigger decision upon the receipt of which they are finally digitised;

The Calibration Boards (CB) [83] allow the injection of precision calibration pulses which simulate the ionisation signals as accurately as possible;

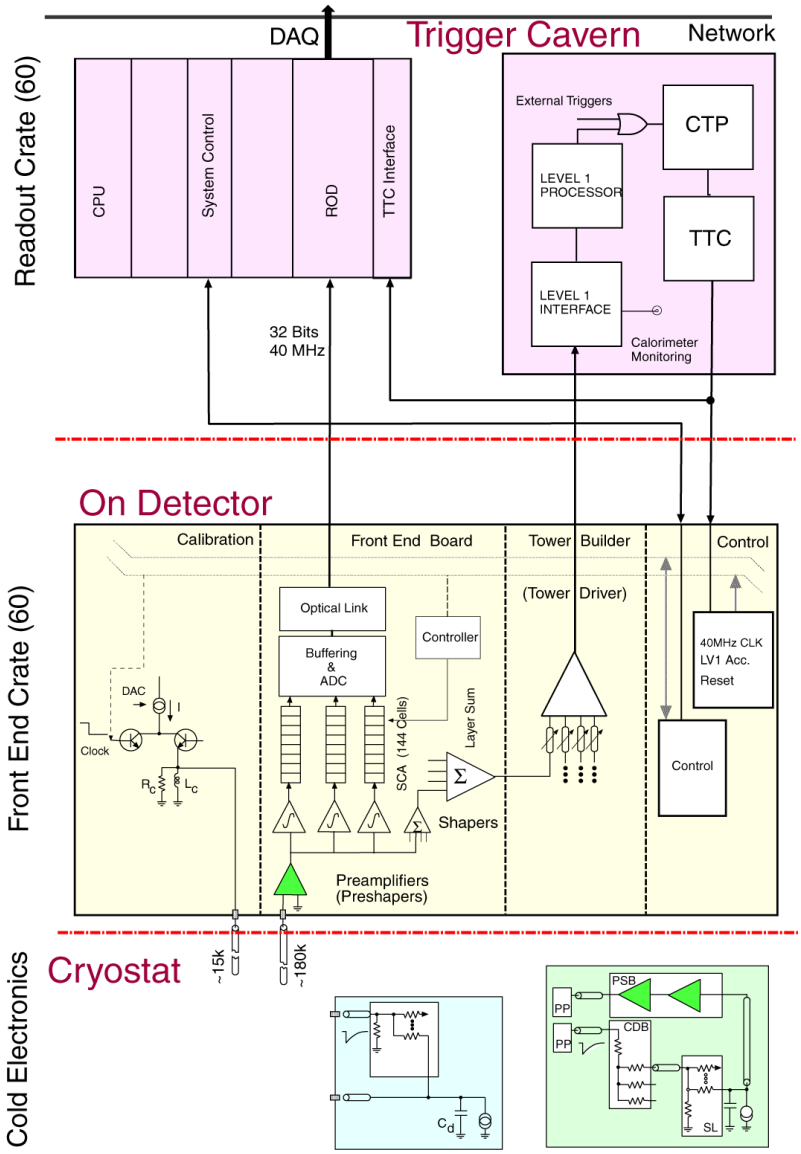

Figure 3.1: Block diagram of the read-out electronics. Note the different motherboards in the cold: EMEC and FCAL (blue): pre-amps on the FEB, HEC (green): pre-amps and summing in the cold [78].

The Tower-Builder Boards (TBB) [84] performing analogue summation of calorimeter cells to form trigger-tower signals which are transmitted to the Level 1 (L1) trigger processor;

The Control and Monitoring boards: The Level-1 accept as well as the 40 MHz clock signal together with several other fast control signals (Trigger, Timing and Control: TTC [85]) are received optically by the controller boards, which control the other boards in the crates via a dedicated bus using the Serial Protocol for Atlas Calorimeters (SPAC [86]). The monitoring boards transmit information from the temperature and liquid argon purity monitoring system.

The BE electronics include Readout Driver (ROD) boards which perform DSP-based digital filtering of the signals and reconstruct the corresponding time, energy and data quality tag, before sending the data to storage. A more detailed overview of the entire ATLAS LAr readout chain can be found in [81]. The overall FE system architecture is documented in [79]. Details about the design and implementation of the FEB and Calibration boards can be found in [82] and [83], respectively.

Ionisation Signal and Shaping

The incoming particles with an energy above 26.4 eV ionise Argon, i.e. they create electron-ion-pairs. In an electric field supplied by the high voltage (HV) system, the electrons then drift with a drift velocity v_D towards a readout electrode. The current induced in the electrode decreases linearly with time as the electrons arrive at the electrode (see Figure 3.2 (a) for a typical ATLAS LAr signal).

This way a minimal ionising particle loses 2.1 MeV per cm in pure LAr and in a gap of

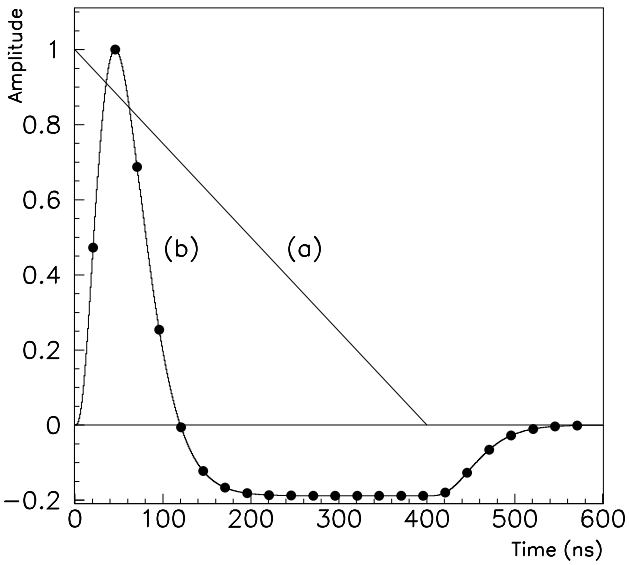

Figure 3.2: The ionisation signal is shown (a) before and (b) after shaping. The dots indicate the digitisation samples [87].

2 mm induces a maximal current of 48 nA to the capacitance of the read out electrode. The typical drift time of the electrons in a 2 mm LAr gap, and hence the length of the total signal, is about 450 ns for a typical field of 2 kV.
Depending on the region in the calorimeter system, the noise of the pre-amplifiers due to the mere detector capacitance for a single calorimeter channel is typically ∼10 - 50 MeV (and somewhat higher for the HEC, where the cells are biggest). The low end of the FEB dynamic range is thus set by the pre-amplifier noise. The high end of the scale has been set to ∼3 TeV, which is the largest energy that could be deposited in a single channel of the EM calorimeter due to an electron originating from the decay of a 5 TeV Z' boson. Being able to cover this entire energy range requires the FEB to have a dynamic range of about 17 bits.
An additional complication is the high luminosity at LHC, which leads to multiple collisions at each bunch crossing, i.e. every 25 ns. One expects 23 minimum bias events per bunch crossing, which will preoccupy the detector with so called pile-up noise. In order to satisfy these demanding requirements, the signals are *shaped*. The pre-amplified signals are fed into a four-channel shaper ASIC, which splits each signal into three overlapping, linear gain scales in the ratio 0.8 (LOW gain), 8.4 (MEDIUM gain) and 82 (HIGH gain). The shaper applies a bipolar $CR-(RC)^2$ analogue filter to each scale to optimise the signal-to-noise ratio. Here the single differentiation step removes the long tail from the detector response, while the two integrations limit the bandwidth in order to reduce the noise. The output signal of the shaper is shown in Figure 3.2 (b) and has a time integral of zero. Finally the signal is sampled with 40 MHz for digitisation in 12-bit ADCs (dots in Figure 3.2). Upon receipt of a L1 accept signal typically five samples around the peak of the signal are acquired, but for calibration and monitoring purposes up to 32 samples can be read out.
In the BE system a first signal reconstruction step is performed, using the method of optimal filtering. The method is used to reconstruct the amplitude and time of a signal of known shape as a linear combination of discrete measurements, i.e. the digitised samples. It is described in detail in [88], [89]; its basic principle is a minimisation of the noise contribution to the variance of the signal amplitude, by using the known signal shape and the corresponding noise autocorrelation matrix. With a Lagrange multiplier technique individual weights for each of the 5 samples are computed: One set of weights in order to optimally reconstruct the signal amplitude (a_j in Equation 3.3) and a second set of weights (b_j in Equation 3.3) in order to reconstruct the corresponding time shift of the signal. This procedure minimises the error in energy and time reconstruction.

The Calibration System

In order to simulate the ionisation signals in the calorimeter, a pulse of precisely known current is injected into high precision resistors, located in the cold in direct proximity to the electrodes. The pulse is generated by fast switching of a current flowing through an inductance. The shape of the calibration pulse has to be as close to the 'physics' signal as possible, i.e. the rise time should be less than a few ns and the decay time should correspond to the drift time. The drifting electrons in the gap generate a 'physics' signal of triangular shape, whereas the calibration signal is of exponential shape. This leads to a difference which is dependent on the shaping time and also on the electrical properties of the readout cells and hence on pseudo-rapidity. However, it never exceeds 4% and is

taken into account in the calibration procedure ($\frac{M_{phys}}{M_{cali}}$ in equation 3.1). This procedure will be discussed in further detail in section 3.3.

HEC LAr Gap and High Voltage

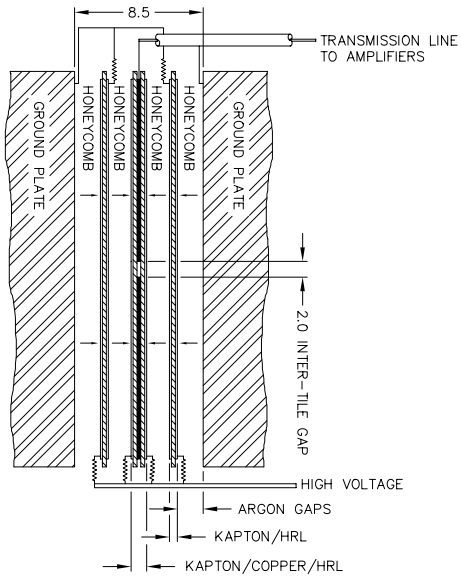

Figure 3.3: The HEC LAr gap between two copper plates with the Electro Static Transformer (EST) consisting of the three different high voltage (HV) and readout boards (see text), separated by a honeycomb spacer [78].

The HEC liquid Argon gaps are divided into four sub-gaps by the readout and high voltage electrodes as shown in Figure 3.3. The electrode structure is using the principle of the Electro Static Transformer (EST) [90]. The EST in each gap is made of a central readout electrode (PAD) and two high voltage boards (EST boards). The EST board consists of an insulating Kapton layer which is sandwiched in between two conducting high resistive layers (HRL). The PAD is made of a segmented copper readout electrode which defines the $\Delta\eta \times \Delta\phi$ granularity and is covered on both sides with an insulating layer and thereafter with a HRL. To guarantee the correct distance between the different boards of the EST over the whole area, a honeycomb spacer-mat is inserted in the four sub-gaps.
With the use of the EST the voltage necessary to reach the required electric field of 10 kV/cm is reduced by a factor of two. Also, the noise behaviour is more favourable as the effective gap is smaller, while the cell capacitance remains unchanged. A further advantage is that in the case of high voltage problems in one of the sub-gaps the signal amplitude is reduced, while all shower fluctuations are still measured correctly. Thus the energy resolution is affected only marginally. For the nominal high voltage of 1,800 V, the typical drift time for electrons in the drift zone is 430 ns.
The electrodes in the gaps use the concept of 'active pads': the input signal of each pair of two consecutive pads is fed into a separate pre-amplifier. These pre-amplifiers are located in direct proximity to the electrodes inside the cryostat. The use of GaAs pre-amplifiers [91] in the cold guarantees an optimum of signal-to-noise ratio for the HEC and hence allows for the detection of muons and the measurement of any radiative energy loss

in the HEC.
Groups of signals (2 to 16, depending on the region in the detector) from several preamplifiers are then summed actively in the cold, forming the output signal for one cell.

3.3 Electronics Commissioning and Calibration

In the following section the principle of electronics calibration of the liquid argon calorimeters in ATLAS shall be introduced briefly, and some studies carried out during the commissioning phase will be shown.

The conversion of an electronics signal (i.e. the current induced by the drifting ionisation electrons) measured in μA, to a measurement of the energy deposited in one cell in MeV is done in several steps. The calculation from ADC counts of the digitised samples (s_j) to the cell energy is shown in the following equation:

$$E_{cell} = F_{\mu A\rightarrow \text{ MeV}} \cdot F_{DAC\rightarrow\mu A} \frac{1}{\frac{M_{phys}}{M_{cali}}} \sum_{i=1}^{M_{ramps}} R_{iADC\rightarrow DAC} \left[\sum_{j=1}^{N_{samples}} a_j(s_j - p) \right]^i \tag{3.1}$$

where a_j are the aforementioned optimal filtering coefficients. The sampling fraction ($F_{\mu A\rightarrow \text{ MeV}}$ in Equation 3.1) mentioned in section 2.3.4 is extracted from the analysis of test-beam data, where the calorimeter modules were exposed to particle beams of known energy. For electronics calibration, LAr calibration data are taken in *delay runs*: A calibration pulse delivered by the calibration board is pulsing the calibration chain and the signal is read out with the standard readout chain. For a detailed study of the signal, the nominal sampling rate of 25 ns used in the readout is too coarse. In order to get a finer resolution, the sampling trigger is shifted by 24 delay steps of 1 ns with respect to the calibration signal in consecutive events. Thereby an effective sampling rate of 1 ns is achieved. The full calibration shape is then reconstructed as the average over a given set of triggers per point (usually 100 triggers are taken). Given the precise modelling of the electronics chain, this allows for the extraction of the factors $F_{DAC\rightarrow\mu A}$ and $\frac{M_{phys}}{M_{cali}}$ in Equation 3.1. In so called *ramp runs* the electronics response to the calibration pulses of different amplitude ($R_{ADC\rightarrow DAC}$ in Equation 3.1) is determined. The noise behaviour and the channel specific pedestal is studied in *pedestal runs* where the detector is read out while idle and for each cell the pedestal (p in Equation 3.1) and its RMS, the noise, are measured. The correct knowledge of the pedestal is crucial, as it facilitates the definition of the baseline of the bipolar LAr signals. For the energy reconstruction the pedestal value is subtracted from the read out samples. The noise, particularly its autocorrelation matrix, on the other hand, is needed for the computation of the optimal filtering coefficients.

3.3.1 Pulse Shape

The ramp runs and delay scans were used to do a full pulse-shape analysis of all signal channels. Pathological channels were identified and the amplitude stability was monitored. For pathological channels it was important to identify the source of the distortion, whether it was coming from the calibration line or the readout line. In the first case, ϕ symmetry was exploited to patch the calibration signal with a signal from a neighbouring cell with

similar geometry and cable-length. However, in the case of a real readout pathology, the prediction of the pulse had to be adapted, using the measured calibration signal.
Figure 3.4 shows two examples of calibration signals for the different gains in the HEC (the HIGH gain is not used in the HEC). The left plot shows a typical calibration signal - note the difference in the undershoot to the physics signal shown in Figure 3.2. It is this difference which has to be accounted for by $\frac{M_{phys}}{M_{cali}}$ in Equation 3.1 and the modelling of the electronics chain.
The right plot in Figure 3.4 shows a channel with a problem in the readout chain: The second peak is due to a reflection caused by a faulty termination resistor on that line. However, the pulse prediction is correctly taking this into account and hence the physics signal is correctly described as will be shown later (Figure 3.25). The time stability of pulse amplitude and pulse width of the calibration shapes is shown in 3.5. By pulsing calibration

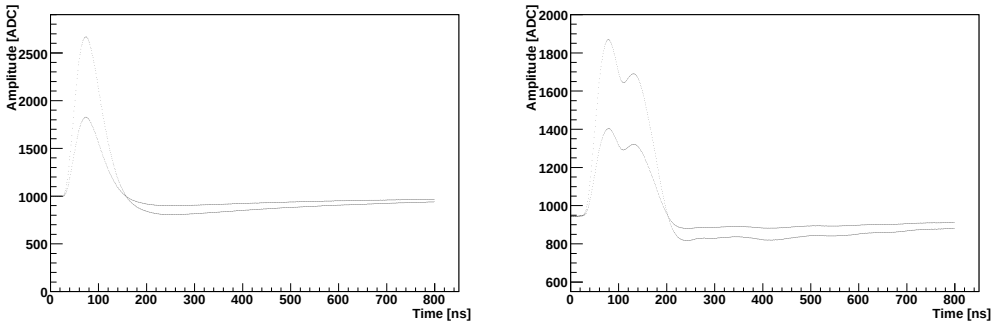

Figure 3.4: A typical calibration signal for two different gains is shown on the left - note the difference especially in the undershoot to the physics signal in Figure 3.2. On the right the calibration signal of a faulty channel is shown. The second peak stems from a reflection in the readout chain, caused by a faulty termination resistor.

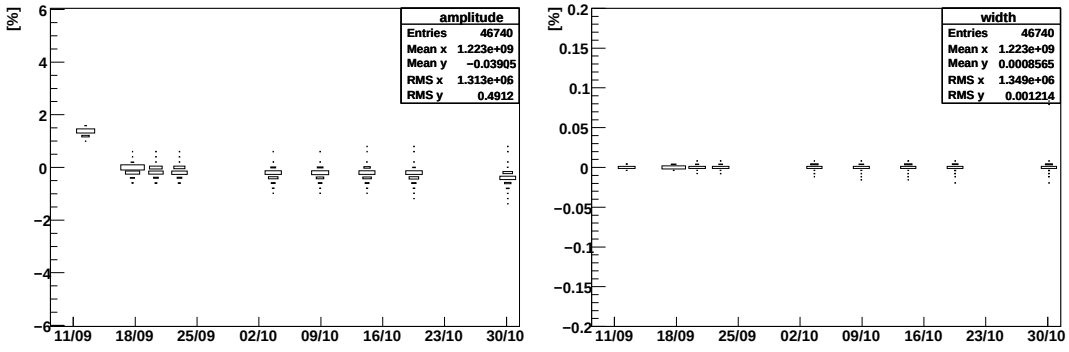

Figure 3.5: Time stability of the calibration shapes in the HEC during two months in fall 2008. The left plots shows the stability of the amplitude. Note that the first measurement was done with a different cooling temperature. The right plot shows the stability of the pulse width. The number of entries in the respective bin is represented by the width of the box.

lines in dedicated patterns the crosstalk between the different readout channels is studied. In some regions of the calorimeters, e.g. in the first, very finely segmented sampling of the electromagnetic calorimeter, the strips, the crosstalk is in the order of $\mathcal{O}(10-15\%)$ and a dedicated correction is necessary, as this capacitive crosstalk is influencing the signal. In the HEC the capacitive crosstalk is in the order of $\mathcal{O}(< 0.5\%)$ and present in most channels (due to the routing of the cables), whereas resistive crosstalk is in the order of $\mathcal{O}(< 7\%)$ and typically only visible between neighbouring pads. This resistive cross talk is mainly due to the high resistive coating layer (HLR) on the HEC electrodes. Contrary to the capacitive crosstalk, the resistive crosstalk is in time with the signal, does not change the signal shape and hence is not problematic.
Figure 3.6 (right) shows the typical crosstalk induced by the calibration signal displayed on the left. Neighbouring channels typically show resistive crosstalk (e.g. upper row left) which is due to the resistive coating of the electrodes and is in time with the signal. By contrast opposed channels usually show capacitive crosstalk (e.g. upper row middle), which shows the shape of an inverted derivative of the signal.

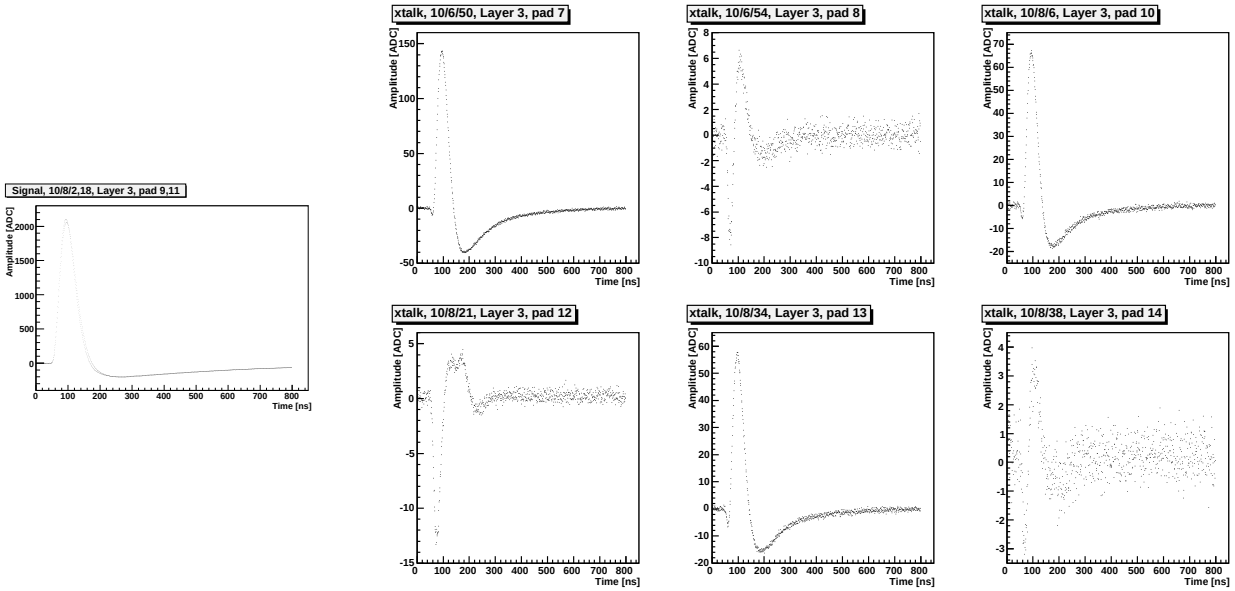

Figure 3.6: The calibration signals shown on the left cause the crosstalk signals in the different pads as shown in the six plots on the right. Neighbouring channels typically show resistive crosstalk (upper row left and right as well as lower row middle) which is due to the resistive coating of the electrodes. While opposed channels usually show capacitive crosstalk (e.g. upper row middle).

3.3.2 Shape Prediction in the HEC

As the reconstruction of the energy with the method of optimal filtering uses the signal shape as an input, it is of importance to have a good prediction of the physics pulse shape. This prediction [92] is obtained exploiting the fact that the ionisation current is read out through the same chain as the calibration current (cf. Figure 3.7). Both

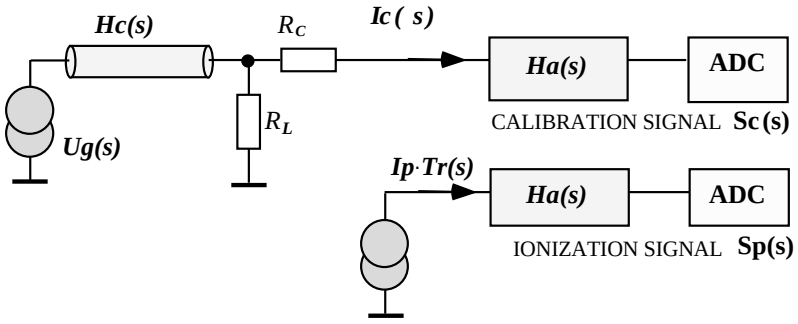

Figure 3.7: Block diagram of the HEC electronics chain for the calibration signal $Sc(s)$ (top) and the ionisation signal $Sp(s)$ (bottom) [92]. The calibration pulse from the generator on its path through the calibration chain results in the calibration current $Ic(s)$, while the ionisation signal generated on the electrodes is described by the triangular function $Tr(s)$. Both signals are read out through the same readout chain described by the transfer function $Ha(s)$. With measured calibration signals $Sc(s)$ it is hence possible to give a prediction of the ionisation signal without a precise knowledge of the readout chain.

the calibration output signal ($Sc(s) = Ic(s) \cdot Ha(s)$) and the ionisation output signal ($Sp(s) = Tr(s) \cdot Ha(s)$) contain the transfer function of the whole readout chain $Ha(s)$. Here $Ic(s)$ is the calibration generator pulse and $Tr(s)$ is the triangular function describing the ionisation pulse.
$Ha(s)$ hence can be excluded:

$$Sp(s) = \left[Tr(s) \cdot \frac{1}{Ic(s)} \right] \cdot Sc(s)$$

The predicted physics pulse in the time domain then can be written as the convolution of the measured calibration signal $Sc(t)$ with a kernel function $R(t)$:

$$Sp(t) = \int R(t-x) \cdot Sc(x)\, dx$$

This kernel function $R(t)$ is obtained through analytical calculations from the model of the calibration chain and the triangular shape of the ionisation current.
Hence a precise knowledge of the calibration chain in combination with a measured calibration signal is sufficient in order to predict the physics pulse shape and a precise description of the readout chain is not necessary.

3.3.3 Jitter

In order to get an understanding of the timing precision and to measure possible variations in timing caused by the components in the readout chain, the so called jitter on the

signal is computed. The principle of this computation [93] is sketched in the following paragraphs.
The approach chosen here uses as input the full calibration and readout chain. The resulting jitter will thus be a convolution of contributions from the readout and the calibration electronics components. On the FEBs themselves a dedicated component, the Quartz Phase Locked Loop (QPLL) was installed in order to reduce the jitter. In order to get an estimate of the jitter on the readout chain only, the reader is referred to [82] where the jitter of the FEBs was measured on a test bench. Typical values of the jitter were ~ 10 ps, and a requirement was made that the value is not to exceed 30 ps.
The calibration pulses obtained by *delay runs* are available in the `C++` object `CALIWAVE`. Amongst other detailed information, the amplitude, rms^2 (σ^2_{total}) and a numerical derivative of the signal for each time bin of this reconstructed calibration waveform are stored and used for the jitter computation.

Jitter Computation

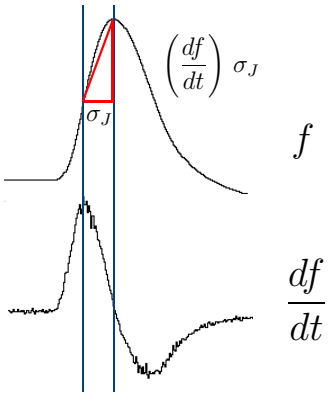

Figure 3.8: On a non-constant, smooth signal $f(t)$ the jitter σ^2_J can be de-convoluted out of the RMS by using the derivative of the signal $\frac{df}{dt}$, as sketched here and described by Equation 3.2.

The above introduced σ^2_{total} can be looked at as a convolution of two variations: The variation if no signal were present σ^2_n (referred to as noise) and a variation in the timing σ^2_J (mostly referred to as jitter). Without further computations these two components are indistinguishable. In order to get a measure of the jitter, one can exploit the fact that the signal most of the time has a derivative different from zero and thereby allows a de-convolution into the time and the amplitude contribution, as the horizontal jitter on the pulse flanks appears as an uncertainty on the pulse height. On a non-constant, smooth signal f the jitter can be de-convoluted out of σ^2_{total} by using the derivative of the signal $\left(\frac{df}{dt}\right)$, as sketched in Figure 3.8.

The following formula illustrates this ansatz:

$$\sigma^2_{total} = \sigma^2_n + \left(\frac{df}{dt}\right)^2 \cdot \sigma^2_J \tag{3.2}$$

The second parameter, i.e. the slope of a linear fit to σ^2_{total} plotted over the squared derivative $\left(\frac{df}{dt}\right)^2$ of the `CALIWAVE` yields a value for σ^2_J.

Typical Jitter Distribution

In ATLAS calibration runs, the components contributing most to the jitter are located on the calibration boards. Therefore the jitter within groups of readout channels pulsed by the same calibration board shows a rather Gaussian distribution (with only a few outliers). The mean jitter of these groups however varies significantly from calibration board to calibration board. Figure 3.9 shows a typical jitter distribution of all channels on the FEBs in one feed-through (HECA FT 16) which are pulsed by the same calibration board.
The mean jitter typically ranges from 70 - 80 ps with the exception of channels pulsed by some distinct calibration boards as described in the following paragraph. However, even these channels show a jitter below the TDR requirement of < 150 ns. In particular, one should note that the jitter measured here is the jitter of the whole calibration and readout chain.
During the commissioning phase the jitter was found to be a good observable to quickly spot different problems which were not actually jitter, but often calibration board or readout features.

Jitter Depending on TTCrx settings

The components believed to be contributing most to the jitter are chips on the calibration boards. In the commissioning phase of the electronics, a group of readout channels was found to have significantly higher jitter ($\sim$ 140 ps) than usually observed. To understand this effect in more detail, a small study was conducted, in which the jitter was measured with different configurations of the calibration board.
The Timing Trigger and Control (TTC) system optically distributes the central clock signal to the individual boards of the calibration and readout system. On the calibration board, a dedicated chip, the TTCrx [85,94,95,96] receives and decodes the clock signal such that it is available for the other components on the calibration board, in particular to set the needed delay of the calibration pulse. On the receiver chip, the reference clock signal is filtered by a narrow bandwidth Phase Locked Loop (PLL) which generates the desired local low jitter reference clock signal. The phase between the central clock signal and the local reference clock is regulated by the use of a charge-pump based control circuit. A Delay Locked Loop (DLL) is using a similar principle and defines the delay time to equivalent precision.
The charge-pump current on the control circuits (PLL/DLL) defines the strength of the regeneration and hence has a influence on the jitter on the signal. The charge-pumps current for the PLL and DLL can be changed in order to minimise the jitter. Lower values

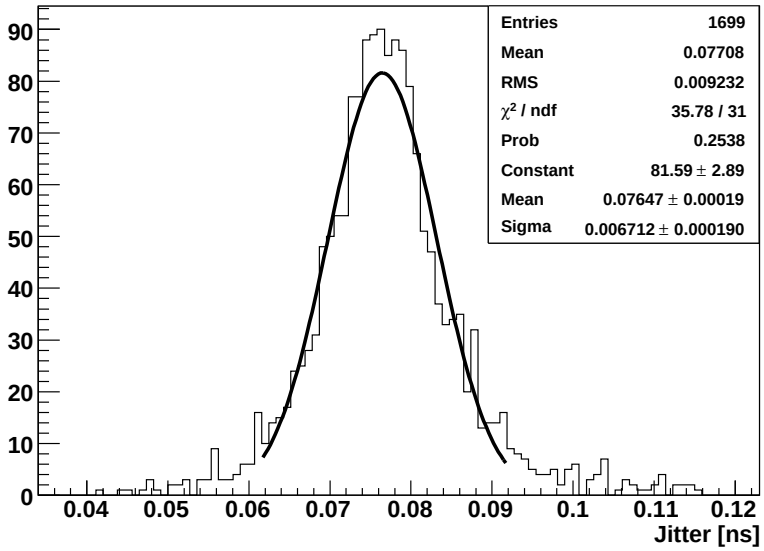

Figure 3.9: Typical jitter distribution of all readout channels pulsed by the same calibration board in feed-through 16 of HEC A. The data used (delay run 102925) was taken in MEDIUM gain.

in general result in lower jitter. There are cases, however, in which jitter can be minimised by using higher values.
For the study the charge-pump current setting on the DLL and PLL were scanned through. Figure 3.11 shows the jitter in feed-through 17 of EMEC C in dependence of various settings of the PLL and DLL. The strong dependence of the jitter on the PLL charge-pump current settings was found to be present only for some of the calibration boards. This might indicate a manufacturing variation of the corresponding PLL circuit. For these calibration boards a tuning of the settings in order to decrease the jitter in principle is possible. The jitter for most calibration boards however, was rather independent of the current settings.

Jitter Conclusions

It should be stated clearly that the jitter values shown here follow the definition of jitter given above, which is a simplified approach - however, it allows to extract some valuable informations about the timing in-situ. In terms of precision they are not competitive to electronics in-lab measurements. Furthermore, they are measured on calibration signals; and as shown in this study, components on the calibration board, namely the PLL and the DLL on the TTCrx dominate the jitter. For the readout chain only, one can safely expect a significantly lower jitter on physics signals as the test-bench measurements in [82] showed.
As the calibration amplitudes for the ramp runs are reconstructed using optimal filtering, a jitter of the here-observed size is expected to have a negligible impact on the amplitude reconstruction where 100 events are averaged. It is expected that this holds up to a jitter of at least 300 ps.

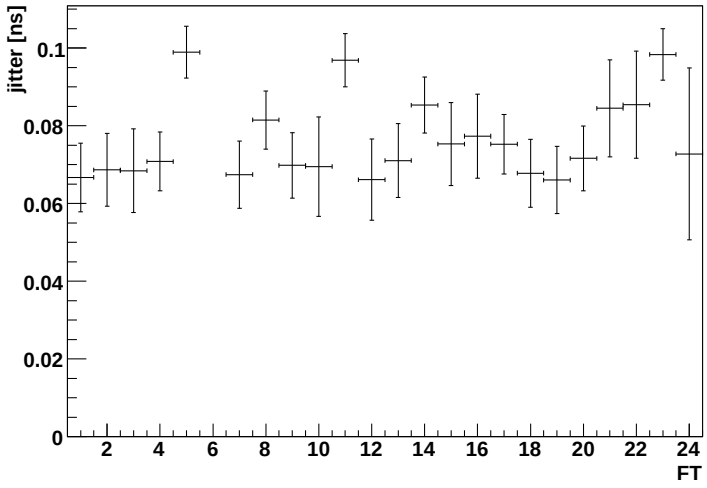

Figure 3.10: Jitter distribution of the single FTs of EMEC A (run 112971 MEDIUM gain). The error bars show the spread of the distributions in the single feed-throughs.

For delay runs, again the average over $\mathcal{O}(100)$ events is used to compute the calibration pulse and hence the impact of the jitter is negligible. A small jitter on the calibration signal would be needed only for a study of the time resolution using calibration pulses. In this case, however, the contributions from the readout chain and the calibration chain could not be measured separately, and even the observed 80 ps are not good enough to look at the electronics readout performance which is much better (20 ps constant). A study on time resolution would need to be performed using the time difference between channels pulsed simultaneously where the jitter contribution is cancelled out.
Therefore the jitter on the calibration signals is acceptable and it is not necessary to further tune the TTCrx settings.

3.3.4 Pedestal and Noise

As mentioned above, it is important to closely monitor the pedestals and their RMS, the electronics noise for each channel. Even though the bipolar character of the LAr signals in principle allows for the extraction of the signal baseline out of the signal itself, the knowledge of each channels pedestal facilitates the signal reconstruction. Each channel has a very specific pedestal which is defined by the voltage offset at the input of the ADC. The components defining this voltage, in particular the operation amplifiers are tuned such that the voltage corresponds to about 1000 ADC counts. This value is chosen such that the positive and the negative amplitude of the shaped signal are well positioned within the dynamic range of the ADC. The pedestal values actually even offer a fingerprint-like identification of the different FEBs. The noise (RMS of the pedestal) is also channel-specific and in HIGH and MEDIUM gain dependent of the cells geometry, mostly dominated by the cell capacitance. At LOW gain, the noise of the preamplifier dominates the RMS. Figure 3.12 shows a typical picture of the pedestal and RMS in one FEB of the HEC. The time stability of the pedestal and noise are shown in Figure 3.13.

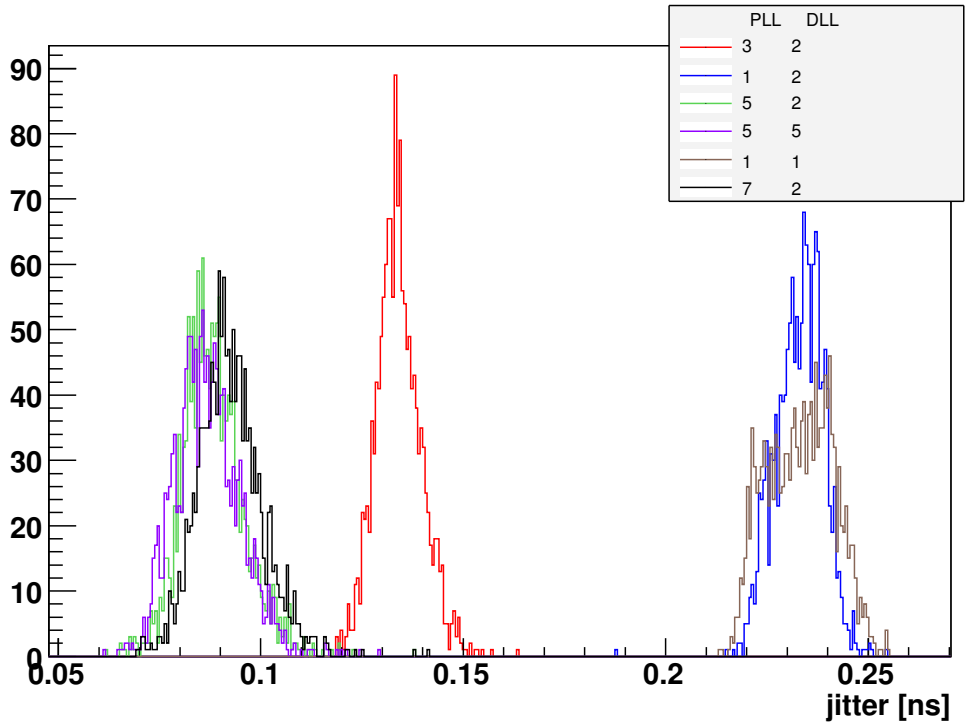

Figure 3.11: Jitter of all channels in feed-through 17 of EMEC C pulsed by one calibration board in dependence of different charge-pump settings of the reference clock signal on the calibration board. The red histogram shows the default settings. It is clearly visible that the settings strongly influence the jitter and a tuning of the settings in order to decrease the jitter in principle is possible.

For energy reconstruction, the pedestal is subtracted from the signal samples (cf. Equation 3.1). The pedestal values for each channel therefore are stored in a database. The knowledge of the noise for each channel, too, is needed for the reconstruction of the cell energy. It enters the calculation via the OFCs which are computed using the noise autocorrelation matrix. Also for higher level objects, the precise knowledge of the electronics noise is crucial. An example are the topological clusters, which are built using cuts on the signal-over-noise ratio (cf. Figure 2.11 and Section 4.1.1).

3.3.5 High Voltage

A further part of the commissioning tasks was a test of the high voltage (HV) system. Some channels were found to be shorted, others were drawing non-negligible currents. High-voltage tests have been performed on the calorimeters in their final position in ATLAS. In the case of the barrel pre-sampler and of the EMEC, most of the shorts can be eliminated by applying a high voltage discharge [97, 98]. After this procedure, approximately 3% of the total number of read out channels in the electromagnetic barrel, approximately 1% of channels in the barrel and endcap pre-sampler and EMEC remain with shorts. In the case of the HEC this procedure was not possible for two reasons: Firstly, the high resistive coating of the electrodes does not allow to punctually 'burn'

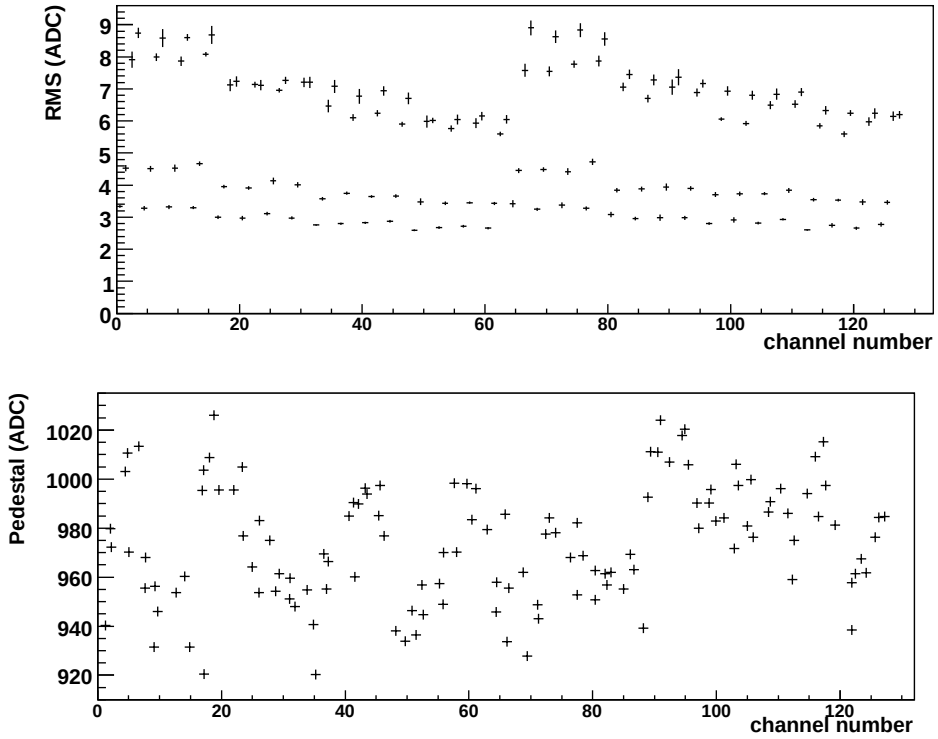

Figure 3.12: Typical noise distribution (top) in the channels of slot 8 for all HEC feed-throughs in MEDIUM gain. The noise is dependent on the cell geometry, i.e. the cell capacitance and hence shows a typical structure as function of the channel number. The bottom plot shows a typical pedestal distribution of one FEB 0 on HEC C feed-through 22. Each channel has a very specific pedestal which is defined by the voltage offset at the input of the ADC. The pedestal distribution hence offers a fingerprint-like identification of the FEBs.

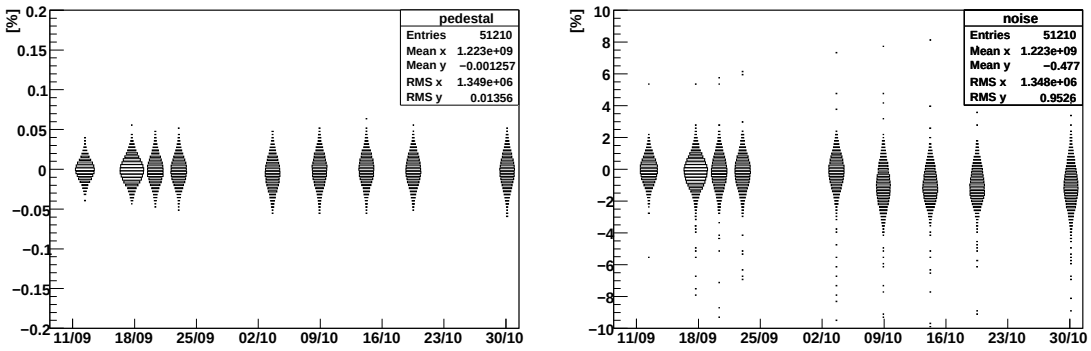

Figure 3.13: Time stability of the pedestal (left) and noise (right) in the channels of the HEC during two months in fall 2008. The number of entries in the respective bin is represented by the width of the box.

shorts and secondly, the sensitive pre-amplifiers are located in direct proximity to the electrodes and could not be disconnected or protected against damage due to this discharge. Approximately 5% of the readout channels in the HEC thus remain with a short. Even in the case of a complete short, a signal in the respective sub-gap will be generated, as the electric field is zero only at the exact location of the short, but non-zero over most of the electrode. In these channels it would be of great value if the position of the short on the electrode could be determined. Test-bench studies were conducted and the field variation was studied as a function of the location of the short [99].
For channels which do not show a complete short, but only draw a higher, but relatively constant current, the impact on the signal is well understood. As the pre-amplifiers are capacitively coupled to the electrodes, constant currents are not visible for the readout. Hence only the amplitude of the signal is reduced, but no other effect is expected. The impact of reduced high voltage on the signal is moderate: decreasing the high voltage to half of its value still results in a signal with an amplitude of 77% of the nominal case. The variation of the signal shape as function of the high voltage is mainly due to the variation of the drift velocity with high voltage.
These variations of the signal with variations of the high voltage have been studied in detail [100, 101] and can be accounted for in corrections used for the final energy computation. Figure 3.14 shows an example of the calorimeter response as a function of the high voltage as measured in test beam conditions.

3.4 Detector Status

In the following paragraphs an overview of the detector status as of last fall will be given - at that time ATLAS had been in operation for several months. The shown status has to be understood as an example of a temporary situation of the detector configuration, as some features have changed and many problems have been fixed since last fall. The data analysed in the following were taken in fall 2008 and this detector situation is shown in the following plots. Also, the simulated data for the top quark analysis discussed hereafter represent this detector configuration.

3.4.1 Reduced High Voltage

Figure 3.15 shows the situation of the high voltage system for the HEC. The figure shows all channels for which the correction factor to be applied in order to compensate for reduced signal height due to reduced high voltage is larger than 1.01. For some channels, the high voltage is shorted completely, but most of the channels only show a higher, but relatively constant current, which will lead to a reduction of the signal.
As the high voltage lines in the HEC supply the sub-gaps individually, while the electrodes cover the whole area of a HEC module, all η bins for a specific ϕ section are affected by a change in the high voltage on one line. If additional η information on the location of the short would become available (e.g. with physics data, or from correlations with the trigger rate in a specific tower), local corrections could be applied. The local variations of the high voltage field in case of different scenarios of shorts have been studied in test-bench measurements [99].

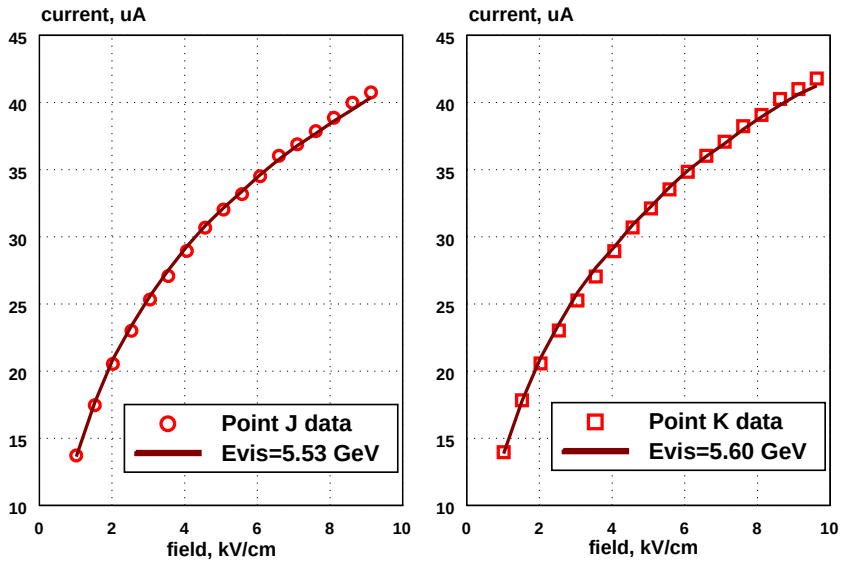

Figure 3.14: Test beam measurement of the ionisation current in the HEC cells as a function of the high voltage in the gap [101]. The data was successfully modelled and fitted as the curve shows. This curve will be used for high voltage corrections.

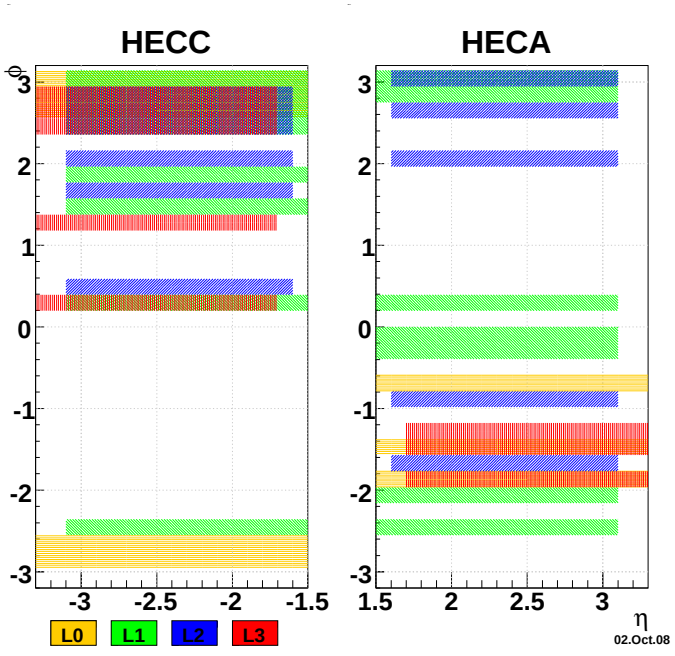

Figure 3.15: Channels with reduced high voltage in the HEC for which the correction factor to be applied to compensate for reduced signal height due to reduced high voltage is larger than 1.01. The first, second, third and fourth sampling layer is shown in yellow, green, blue and red, respectively.

3.4.2 Distorted Channels

Several channels were found to have distorted signals, their locations inside the detector are shown in Figures 3.16 and 3.17.
For some cases, the electronics calibration system is not functioning, but the physics pulses are expected not to be affected. A damaged calibration line or resistors could cause such a case, for which a repair is not possible. The calibration constants for channels with faulty calibration lines (cf. Figure 3.16) are obtained exploiting ϕ symmetry: the average of all ϕ neighbours at the same η position is taken as reference. In this case, the error on the reconstructed calibration pulse height is dominated by the spread of the preamplifier gains, which in average over all channels in the HEC is about $\pm 4.2\%$.
In some cases however, the distortion visible in the calibration signal is expected to affect both calibration and physics pulses. Figure 3.4 (right) is an example of such a channel. For this case no further corrections are applied as the distortion is expected in physics signals, too. The distortion hence is taken into account in the prediction of the expected physics signal shape (cf. Figure 3.25). Channels showing this feature are shown in Figure 3.17.

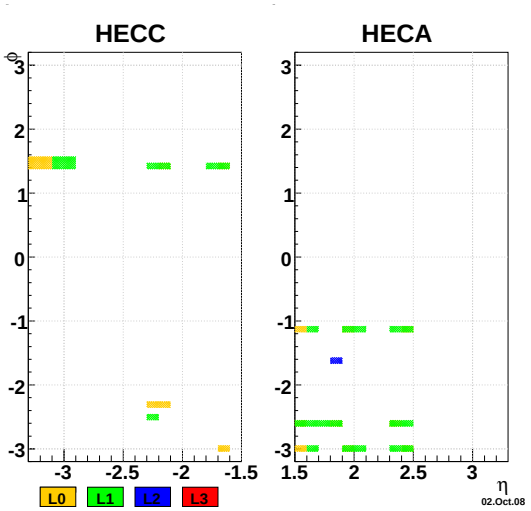

Figure 3.16: Channels with faulty calibration lines in the HEC. The calibration constants for these channels are obtained by exploiting ϕ symmetry in the HEC. The first, second, third and fourth sampling layer is shown in yellow, green, blue and red, respectively.

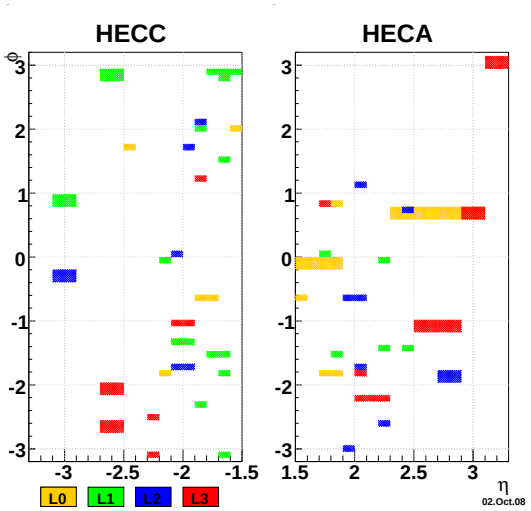

Figure 3.17: Channels with distorted signals in the HEC. This could be due to problems in the calibration chain or in the readout chain. For some channels the source can only be determined with physics signals (cf. Figure 3.25).

3.4.3 Dead Channels

Channels with malfunctioning readout lines are shown in Figure 3.18, left, if the problem is located inside the cryostat where no possibility for a repair is given and the channels thus have to be considered as permanently lost. In Figure 3.18, right, for the channels where

the problem is located outside the cryostat, which thus are repairable if the detector can be accessed. The big dead region on HEC C was due to a malfunctioning power supply, which is used to power the pre-amplifiers inside the cryostat. All layers of one quadrant of HEC C were affected. The impact on the energy reconstruction will be discussed briefly in Sections 3.7 and 5.2.5. On HEC A one FEB could not be read out.
In the meantime the problem was found to be caused by a faulty soldering point in the power supply. It was fixed for the affected power supply module, and all other modules were checked.

3.4.4 Noisy Channels

Channels for which the RMS of the pedestal readout value is far above the mean value of the RMS for other channels at the same η position, are shown in Figure 3.19. A cut of 5 times the RMS of the corresponding RMS distribution is applied. These channels possibly seed a noise cluster and have to be taken into account in the reconstruction procedure.

3.5 Commissioning with Cosmic Muons

Since summer of 2006, the calorimeter system of ATLAS is regularly taking data with cosmic muons. These are the first real physics signals visible in the different detectors and thus offer a broad field of commissioning studies for the calorimeters themselves, the data acquisition chain and the trigger system. In the barrel region, where the muons' incident angle is such that samples of pseudo-projective muons could be collected, a first estimate of the in-situ calorimeter uniformity and timing could even be given [102]. In the endcap however, where the muons hitting the calorimeter are highly non-projective, and especially in the HEC, where the signal-over-noise ratio for muons is not as favourable as in the electromagnetic calorimeter, the rate is much lower. In particular, much more statistics will be needed in order to extract the muon energy spectrum. Extracting the Landau distribution might not even be possible due to the huge variations of the path-length of a muon in the LAr when traversing the HEC.
A study was conducted using tracks from cosmic particles reconstructed by the tile calorimeter to select cells in the HEC. The approach was to take all HEC cells through which the track pointed to built a geometrical cluster. If the muon track was mapped correctly to the HEC cells, the expectation was that these clusters would mostly contain cells with energy deposits from the muons. This would allow to discriminate cells with muon signals from noise fluctuations. However, the energy spectrum of these clusters was not as clean as expected and not competitive with the approach of simply selecting high energy cells in the HEC. The reason for this presumably is that energy deposits from cosmic showers in the HEC are mainly due to Bremsstrahlung, catastrophic energy loss or air showers, whereas the tracks reconstructed in the tile calorimeter mostly stem from single muons. Due to the non-pointing geometry, signals of single muons seem to be difficult to find in the HEC. To verify this, the study will be further pursued.
First signal studies, however, are possible with the energy deposits from cosmic particles and were performed for the electromagnetic calorimeter in [103]. Exploiting larger energy deposits most probably caused by air-showers or catastrophic energy loss of muons, first signal studies could also be conducted in the HEC.

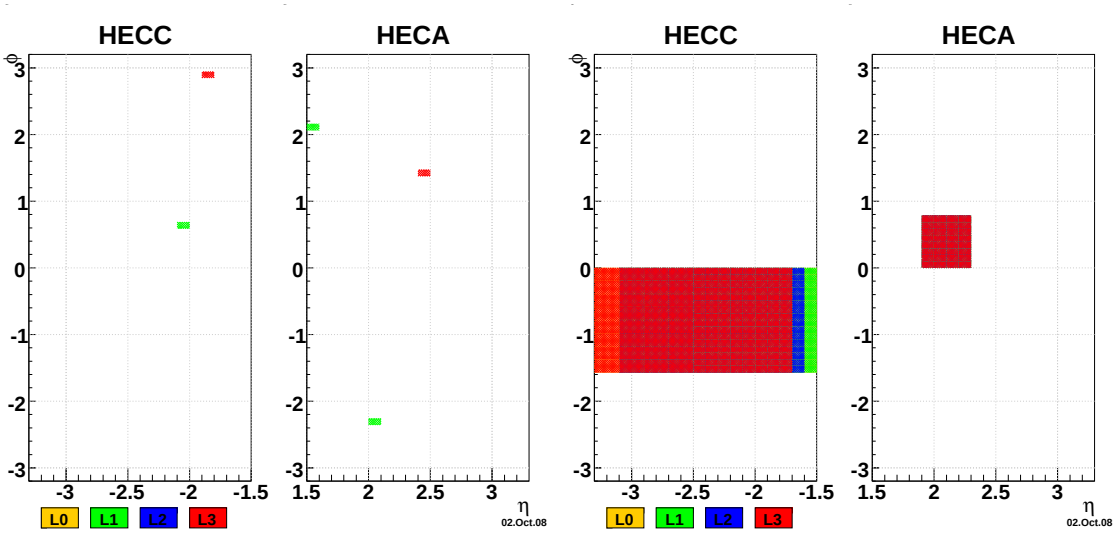

Figure 3.18: Shown are all channels in the HEC that can not be read out from the detector. The left plot shows the cases where the problem is expected to be located inside the detector. These channels are expected to be permanently lost. The right plot shows the channels for which the electronics readout was not functioning at the time. The first, second, third and fourth sampling layer is shown in yellow, green, blue and red, respectively. On HEC C this is due to a malfunctioning low-voltage power supply and on HEC A due to a malfunctioning FEB. Both problems have been fixed in the meantime.

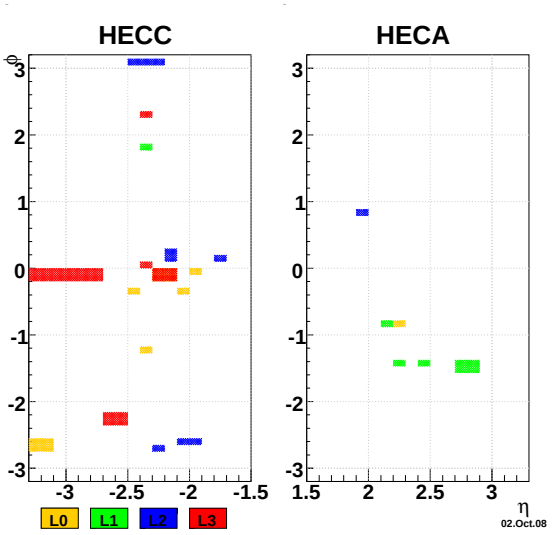

Figure 3.19: Channels with higher noise in the readout chain in the HEC. The cut applied is 5 times the RMS of the corresponding RMS distribution of similar channels in the same η region. The first, second, third and fourth sampling layer is shown in yellow, green, blue and red, respectively.

As all sub-detectors of ATLAS use the cosmic muons for commissioning studies, and data often is taken in combined mode, triggers stream of nearly all sub-detectors are available. In the studies presented here, triggers from the muon system were not used, as the rate is relatively high and the trigger thresholds are well below energies visible in the HEC. The most promising trigger streams are the level-1 calorimeter trigger (L1Calo) and the trigger supplied by the minimum-bias scintillators between the barrel and the endcap calorimeters (MBTS).

3.5.1 Signal Studies with the First Real Physics Pulses

The aim of this study was to obtain a first impression of the precision of the pulse shape prediction in the HEC readout electronics. As the muons arrive asynchronously[1] with respect to the trigger in the different detector cells, an iterative method was used to find the correct timing. This iterative procedure exploits the time information given by the OFCs.
The amplitude at the maximum (A_{Max}) and the difference between assumed and reconstructed time (Δt) are given by the weighted sums over the pedestal subtracted samples, using the two sets of OFCs (a_j and b_j):

$$A_{Max} = \sum_{j=1}^{N_{samples}} a_j(s_j - p); \qquad A_{Max}\Delta t = \sum_{j=1}^{N_{samples}} b_j(s_j - p) \tag{3.3}$$

where s_j are the data samples and p is the pedestal value.
An iteration over sets of OFCs for different phases uses the time difference in Equation 3.3 to determine the phase of the subsequent step. The iteration is continued until the resulting Δt is smaller than the available time resolution of the used OFC sets. For this study sets of OFCs in 17 phases with a ~ 3 ns binning were used.
In order to compare the signal shape of the data with the predicted shape, the data were scaled by $\frac{1}{A_{Max}}$ and shifted according to the phase determined by the iterative procedure. In order to get a clean signal sample only cells with an energy of more than 5σ above the expected electronics noise (cf. Figure 2.11) or an absolute value of more than 1.5 GeV were used for the signal study. In addition to this cut in energy, the signals in the sample were classified into several categories according to their signal shape. Noisy channels, i.e. channels with fluctuations before the peak or in the undershoot were not used. Also, signals which showed a saturation of the dynamic range, either in the positive or negative dynamic range, were excluded. Signals showing the typical shape of crosstalk as shown in Figures 3.27 and 3.26 were also flagged and not used for the comparison. As shown in Figure 3.20 this selection was only passed by few events per cell, in some cases by few tens of events. For smaller values of $|\eta|$ the statistics are slightly more favourable as the cells in the HEC are significantly larger in this region.
The available statistics were not high, hence ϕ symmetry in the HEC was exploited: Per sampling layer one histogram was filled with all cells in rings of constant η. This was done for data and for predicted signal shapes and the residual between data and prediction was

[1] The timing resolution in the LAr calorimeter is good enough to resolve time-of-flight effects and effects due to cable lengths of the readout, which are optimised for signals of particles coming from the interaction point. This is why the signals from cosmic muons not coming from the interaction point are asynchronous.

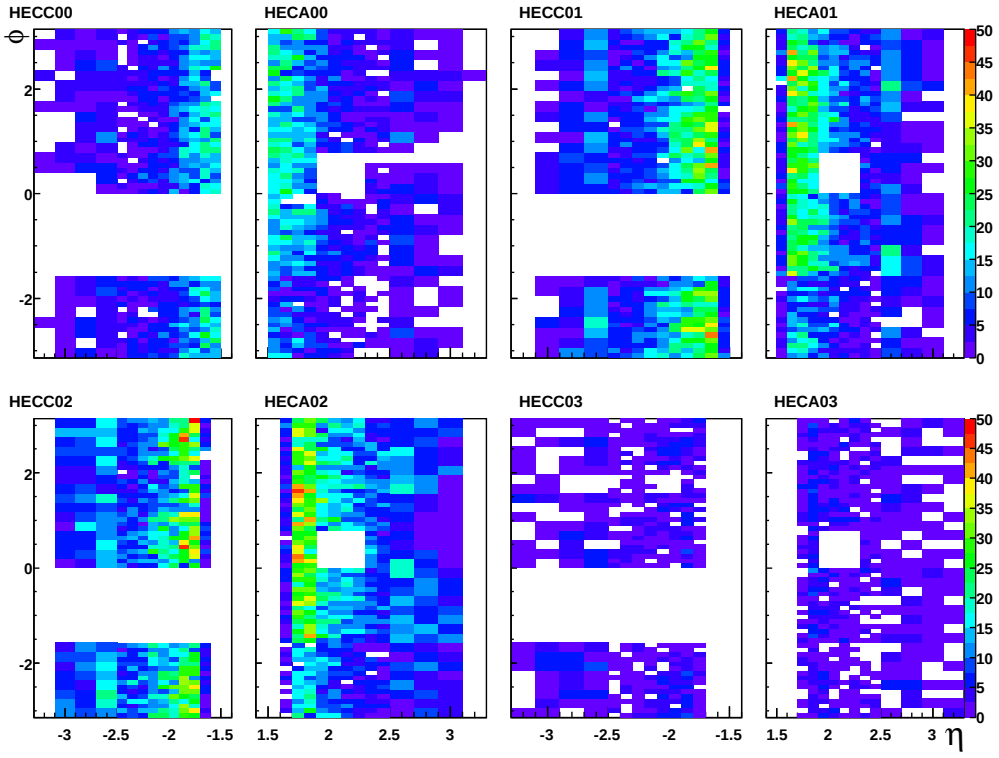

Figure 3.20: Coverage of selected good signal shapes from cosmic events in the HEC used for this study. At this run period, one quadrant of HEC C and one single FEB in HEC A was not read out.

computed. Figure 3.21 shows an example of this comparison: The red histogram shows the signal shape as obtained from data, the black from prediction. The blue histogram shows the residual, its scale is shown on the right axis. For those rings of constant η where enough statistics were available, i.e. the data histogram had at least 10 entries per bin, the residual was plotted for three different regions: In the region below the peak of the signal, i.e. below the two flanks of the signal, the residual shows a local maximum and a local minimum. The distributions for positive residual values are shown in Figure 3.22 (top) and for negative values in Figure 3.22 (middle). The residual in the region at the end of the undershoot, which actually is sensitive to the drift-time of the electrons in the liquid argon gap is shown in Figure 3.22 (bottom). In these three regions, the mean of the residual is between 3 and 5%.
For most of the channels, the residual below the rising flank of the signal was positive and negative below the falling flank. As the zero-crossing of the residual is not exactly below the peak of the signal, the residual can not be explained by a systematic shift between data and predicted shape.

The residual at the end of the undershoot was already seen in test-beam data. It could successfully be reduced by adapting the drift time in the model of the shape prediction. The predicted shapes used here were modelled with a LAr temperature of 92K, as used in the test beam. This value, however, is not correct for ATLAS conditions, where the LAr is sub-cooled to about 89K. The related parameter in the model will be adapted in

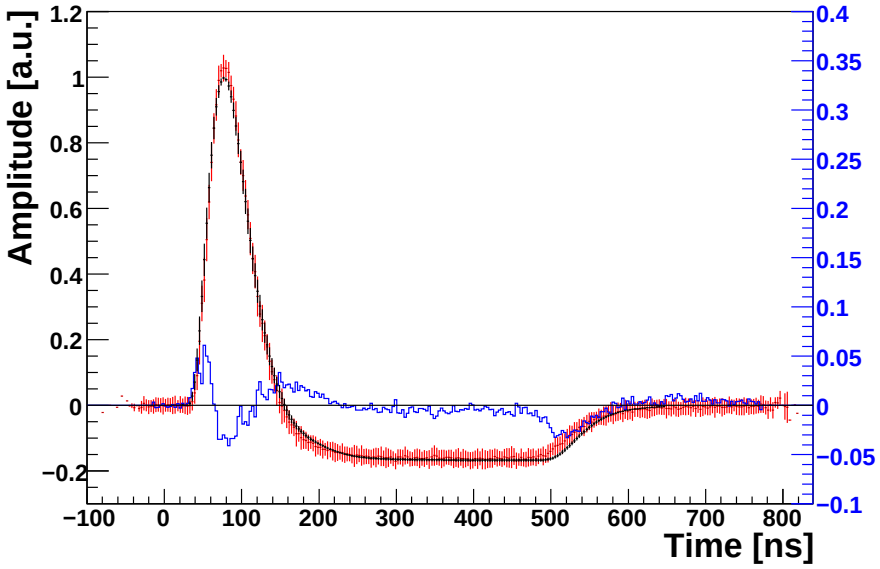

Figure 3.21: The red histogram shows the signal shape as obtained from data, the black from prediction. The blue histogram shows the residual, its scale is shown at the right axis. In order to accumulate enough statistics, all cells in a ϕ ring for one η bin (here $-1.6 < \eta < -1.5$) and one layer (here HEC C sampling layer 0) are filled in the histograms.

the next iteration of shape prediction and it is expected that the resulting change of the drift-time ($\mathcal{O}(-9$ ns)) will reduce the residual at this position.
In order to get an estimate of how well the amplitude and time is predicted by the use of the iterative OFC method, both data and predicted shape were fitted around the peak (65-95 ns) with a polynomial of second order (cf. Figure 3.23). Again, if statistics were enough, the amplitude and the position of the maximum of the fit were extracted and compared. Figure 3.24, left (right), shows the distribution of the so-obtained amplitude (time), respectively. The time is well within the available resolution with the 3 ns binning used here. The amplitude obtained by the iterative method is too low[2] by about 2%.

3.5.2 Discussion of Residuals in Pulse Shape Prediction

The success of the amplitude/energy reconstruction using the technique of optimal filtering (OF) relies on a precise knowledge of the signal shape and of the noise auto-correlation matrix. The noise is measured from data as described above and hence is well known. However, the signal shape prediction is unavoidably imperfect to a certain level. The residual difference between the pulse shape prediction and the true signal shape hence introduces a systematic bias in the reconstructed amplitudes. As shown in [104, 105] this error is independent of the pulse amplitude and depends only on the shape and amplitude of the residuals.
The mathematical properties of the OF reconstruction lead to the situation where upon

[2]Note, the data shape was normalised with the amplitude obtained from the iterative OFC method, a too high peak hence indicates that the normalisation factor was too low.

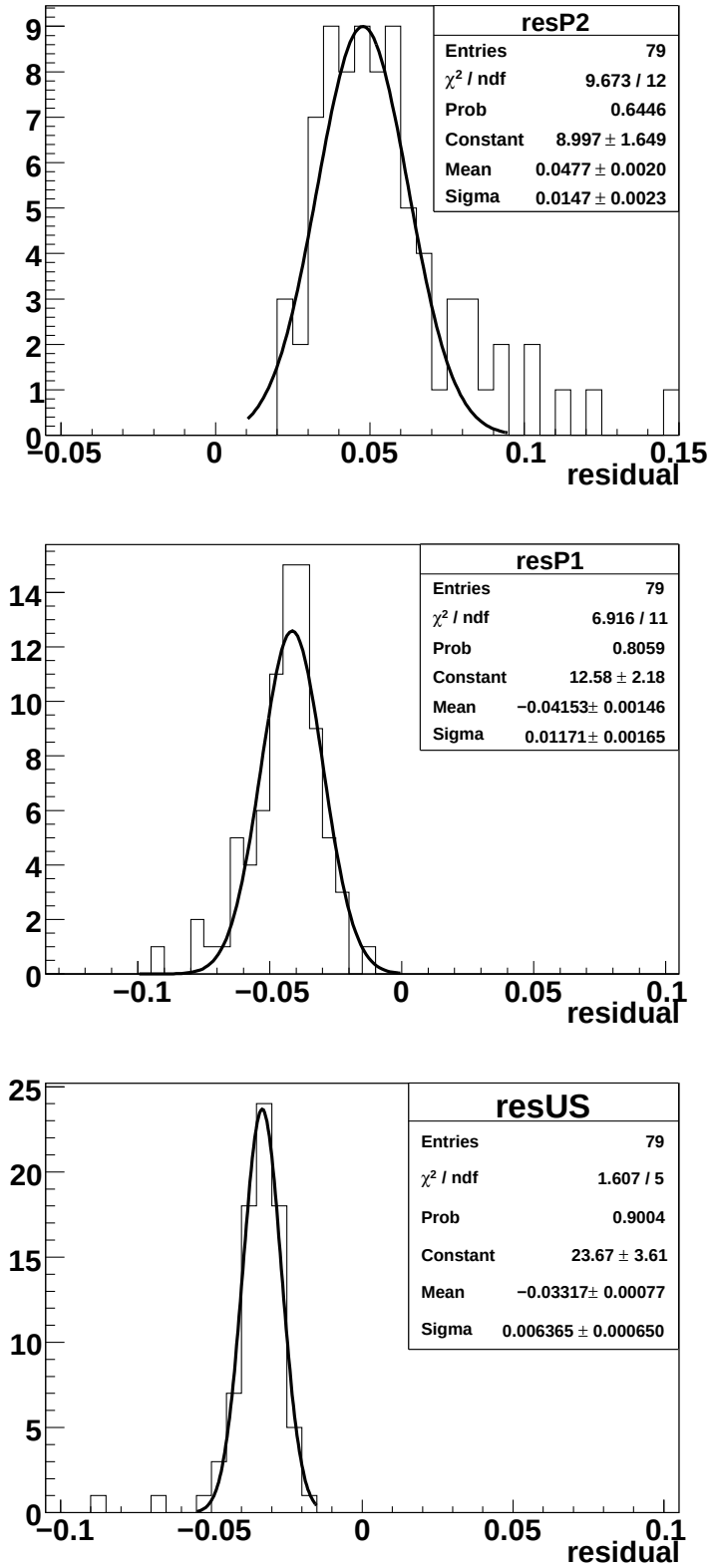

Figure 3.22: Typical residual difference of predicted shape vs. data shape at different positions of the signal. Local maximum of the residual below the peak (top) and local minimum of the residual below the beak (middle) and the residual at the end of the undershoot (bottom).

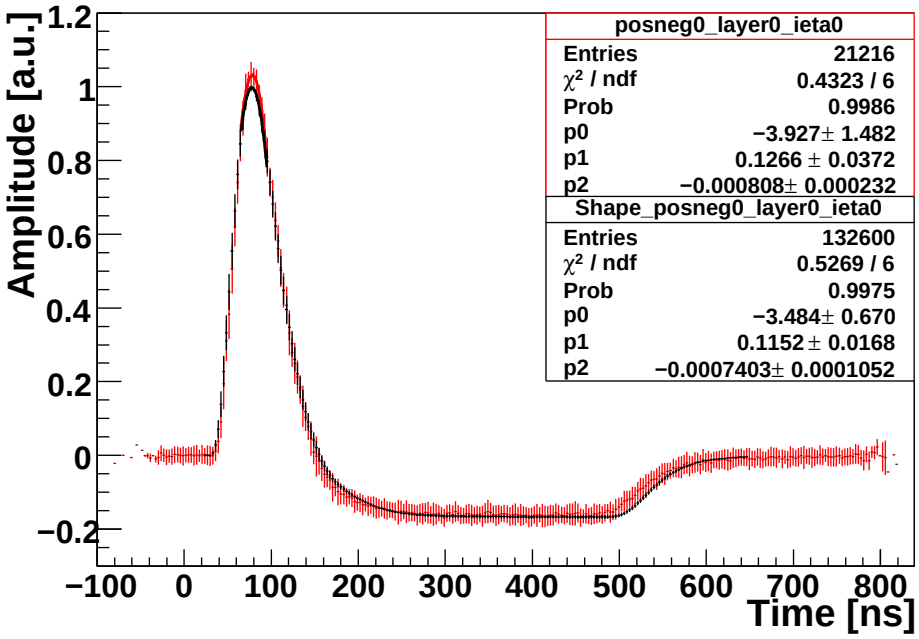

Figure 3.23: The red histogram shows the signal shape as obtained from data, the black from prediction. Both were fitted with a second order polynomial around the peak (65-95 ns). The statistic boxes show the fit parameters. In order to accumulate enough statistics, all cells in a ϕ ring for one η bin (here $-1.6 < \eta < -1.5$) and one layer (here HEC C sampling layer 0) are filled in the histograms.

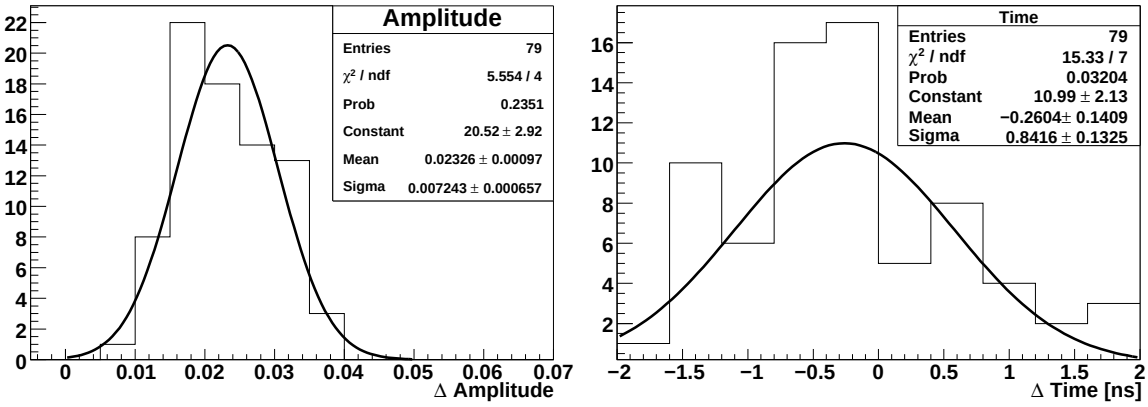

Figure 3.24: Distribution of the amplitude (left) and time (right) difference between measured and predicted signal shape as obtained form a fit in the peak region (65-95 ns).

application on the OFCs to the samples some information about the signal is lost. Hence it is not possible to correctly evaluate neither the residuals nor the bias introduced by the method without making further assumptions. However, a method to obtain the exact shape of the ionisation pulse by the use of pseudo-residuals from well-timed data was presented in [105].
For the cosmic data analysed here, the situation is even more complicated. The timing of the asynchronously arriving cosmic signals was obtained by an iterative procedure which in turn possibly introduces a bias in addition to the bias intrinsic to the signal reconstruction with the method of OF, even if the timing is known perfectly. The above-mentioned residuals and the difference between the reconstructed and the predicted amplitude have to be understood as a combination of the residuals in the signal shape prediction and the bias of the optimal filtering method as well as in the iteration procedure. These three contributions are not distinguishable by the method used here. But as they are independent at first order, the residuals, the amplitude and the timing difference shown here can be considered as an upper limit. The impact on the reconstructed energy is expected to be smaller, but an exact quantification can not be given with the method used here. Once a sample with larger statistics is available, the method proposed in [105] could be applied and the exact shape of the ionisation signal could be extracted, allowing for a more precise study of the impact to energy reconstruction.

3.5.3 Pathological Shapes in Cosmic Events

Looking at the signal shapes from cosmic events, also some pathological channels were detected. It was already mentioned in Section 3.4.2 that some channels were found to show distortions on the signal shape. In the case where the distortion is not only due to problems in the calibration lines, but rather in the readout lines, the measured calibration pulse shapes were used in the prediction of the expected signal shape. Although with only very limited statistics, Figure 3.25 is a nice example of such a case. For channels with faulty termination resistors a reflection is seen in the calibration pulse, just behind the peak (cf. right plot in Figure 3.4). This feature hence also shows up in the predicted signal shape. Even for distorted signal shapes, the procedure of predicting the signal shape and reconstructing the signal amplitude and timing by the use of an iterative application on OFCs seems to work. This is indicated by the correct scaling and timing of the data shown in the figure. Due to a lack of statistics it is not yet possible to estimate the quality of this procedure for distorted channels in detail.

In Section 3.3.1 the signature of crosstalk was briefly discussed. During the analysis of cosmic data some channels were found to show signals with a shape similar to the one expected from crosstalk. Figures 3.26 and 3.27 show the typical shape of these events. The amplitude of these signals was reaching up to 3000 ADC counts in MEDIUM gain. With the expected level of some percent of resistive crosstalk and some per-mil of capacitive crosstalk, these signals hinted to be caused by some unusual feature.

Looking at the η-ϕ distribution of cells that showed this type of signals (cf. Figures 3.28 and 3.29), it was evident that (with the exception of one cell) they are in regions with known high voltage problems.

These cells did not always show the crosstalk-like signals, but were also found to show signals with the expected shape (blue histogram in Figure 3.30). These channels also showed signals with a very small undershoot only (red histogram in Figure 3.30), but of

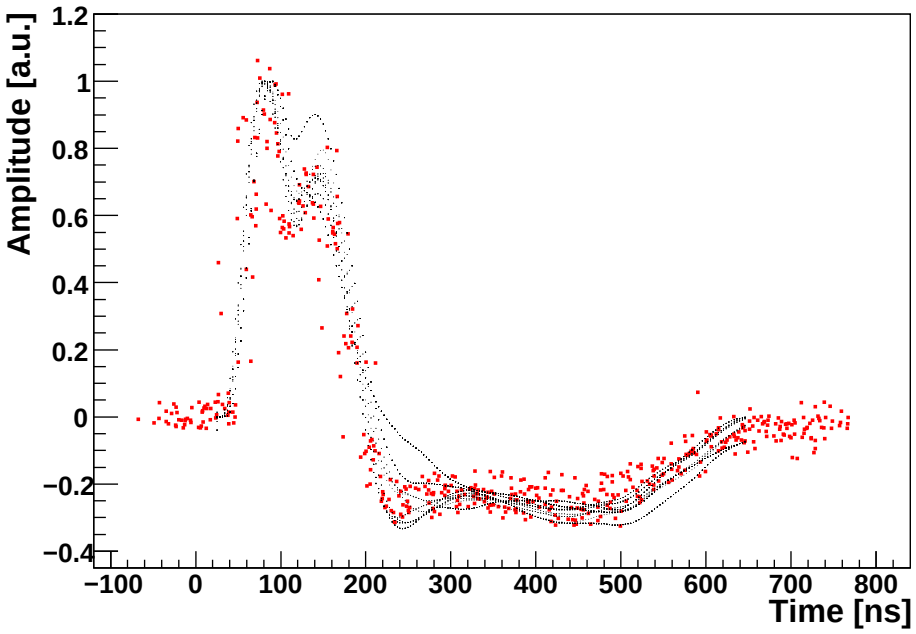

Figure 3.25: Predicted (black) vs. measured (red) signal shape in readout channels with reflection. The scaling and timing of the data indicates, the procedure of predicting the signal shape and reconstructing the signal amplitude and timing by the use of an iterative application on OFCs seems to work even for distorted signal shapes.

very high amplitude, often saturating the LOW gain. The latter signal shape is a typical example of the response of the shaper to a Dirac-like input signal.

These observations and the correlation to regions of high voltage shorts indicated, that the observed signals could stem from high voltage discharges close to the anode, as the undershoot is very short. The same features were also observed in the EM barrel calorimeter, but up to now it was not possible to prove the mechanism which generates these signals.

Even if no exact explanation of the observed signals can be given, the regional correlation with known high voltage problems is striking and it has to be expected that the high voltage problems could be correlated with this signal response.

In assuming a correlation with high voltage problems, the map of cells with the signal shapes mentioned here could provide first η information about the locations of the high voltage shorts, as the high voltage lines themselves are only binned in ϕ and supply the cells in all η bins for a given value of ϕ. Once this correlation is established, it will be possible to apply cell specific high voltage corrections as the field variations are understood for different positions of the short [99].

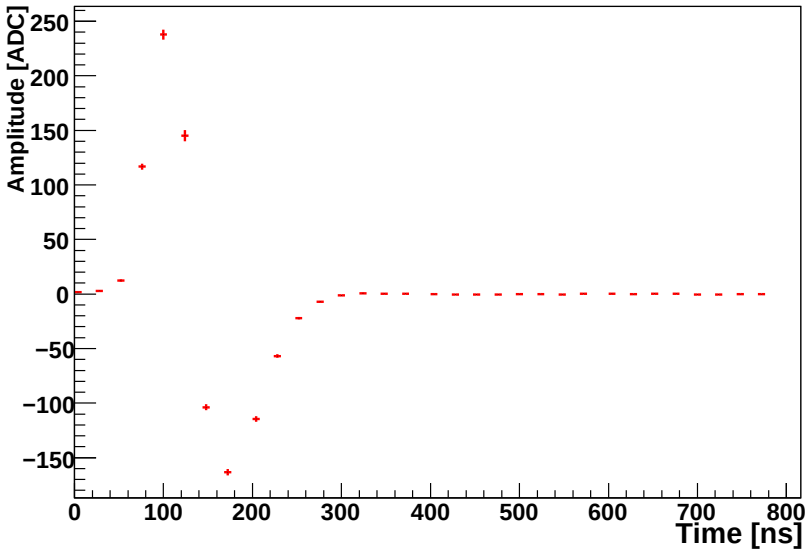

Figure 3.26: Typical shape of enhanced resistive crosstalk. These shapes are found in the regions of known high voltage problems (cf. Figure 3.28) and could give first η information of the high voltage problems.

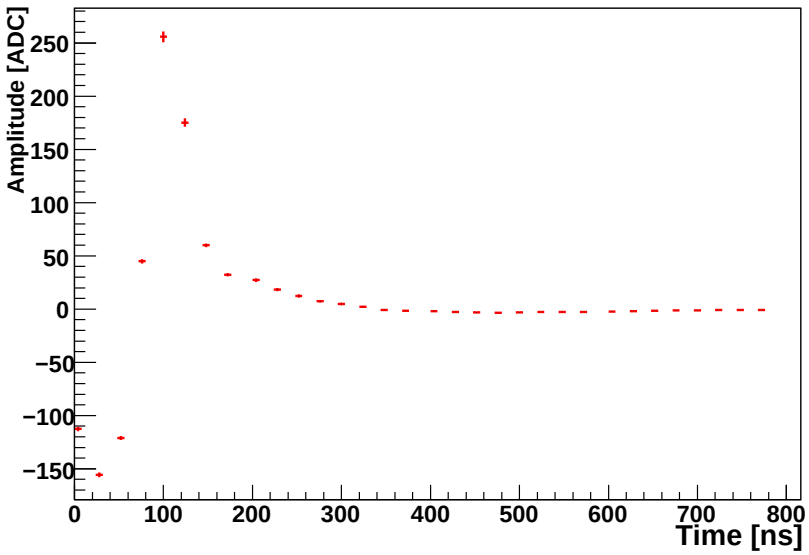

Figure 3.27: Typical shape of enhanced capacitive crosstalk. These shapes are found in the regions of known high voltage problems (cf. Figure 3.29) and could give first η information of the high voltage problems.

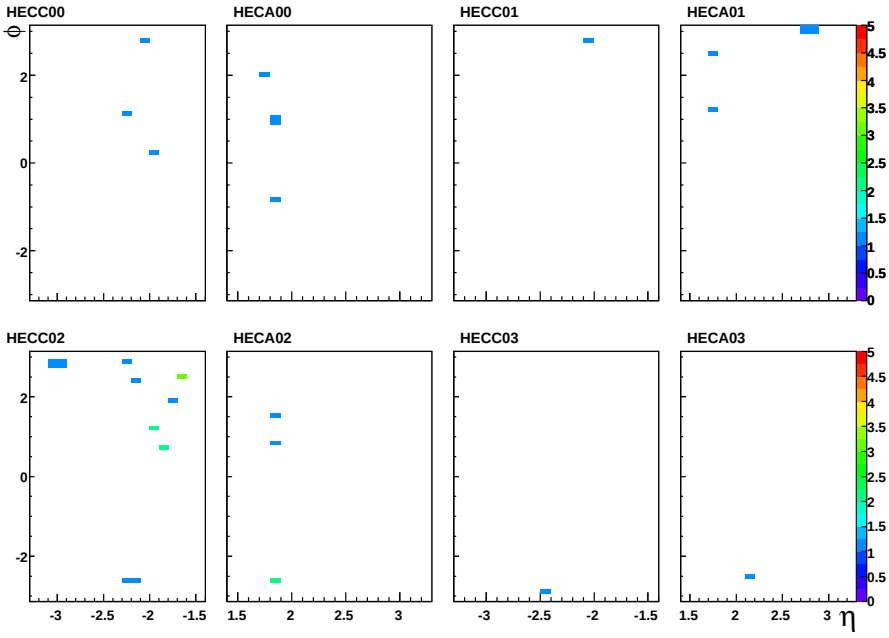

Figure 3.28: η-ϕ distribution of channels showing enhanced resistive crosstalk (cf. Figure 3.26). These channels are located in the regions of known high voltage problems (cf. Figure 3.15).

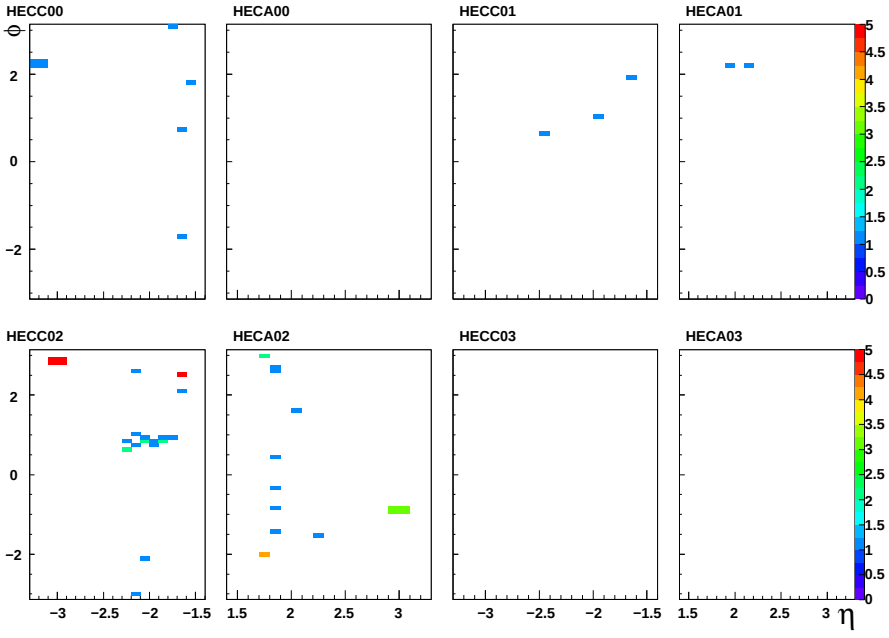

Figure 3.29: η-ϕ distribution of channels showing enhanced capacitive crosstalk (cf. Figure 3.27). These channels are located in the regions of known high voltage problems (cf. Figure 3.15).

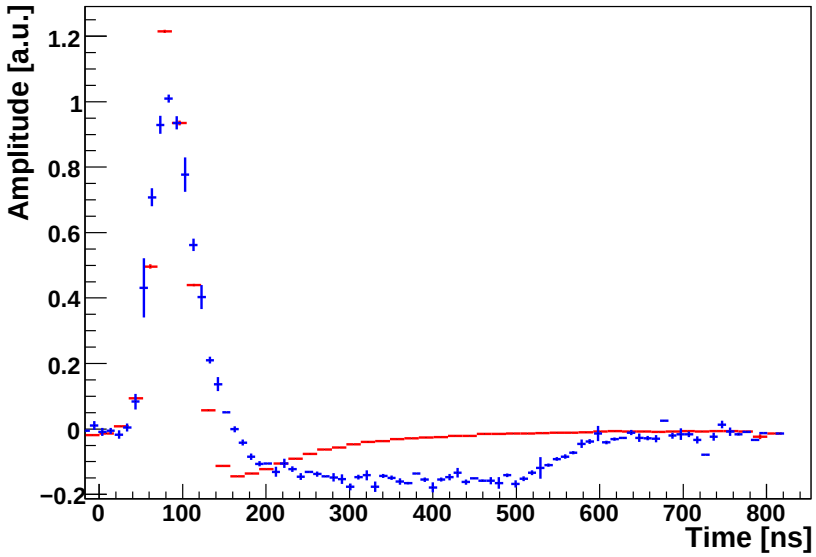

Figure 3.30: Typical shape for channels with high voltage problems. Red without physics signal, possibly caused by a high voltage discharge, blue with cosmic signal.

3.6 First Beam Events

On September 10^{th} 2008 LHC was circulating beams at the injection energy of 450 GeV for the first time. In the course of beam commissioning the beams were dumped on collimators located about 140 m in a straight line from the interaction point of ATLAS. The cascade of particles, mainly pions and muons, reached ATLAS and could be detected by the different sub-detectors. A simple and robust trigger supplied by electrostatic beam pick-up detectors (BPTX) was used to trigger the readout. A run (86 events with 26 real beam splash events[3] arriving from the C-side, $z < 0$) was taken in stable enough data taking conditions.

Figure 3.31 shows the accumulated energy deposited in the two endcaps of the HEC. In some cells several TeV were accumulated during this run. However the absolute value of the energy has to be taken with a grain of salt, as the timing was not optimal for the HEC. A dedicated set of OFCs with 33 phases was used to reconstruct the energy as good as possible.

Looking at the ϕ distribution of the cell energy as shown in Figure 3.32 for the outermost η bin in the first sampling layer of the HEC[4], a eight-fold structure is clearly visible. It is due to the material of the toroidal endcap magnet as sketched in Figure 3.33. The top to bottom asymmetry is explained by the amount of material encountered by the particles, it is higher in the lower hemicycle around the beam-axis. Additional material encountered by the particles along their path through ATLAS is also explaining the lower response of

[3]For the 86 triggered events a correlation between activity in the detector and bunch arrival time information from the accelerator showed that only 26 events were indeed beam splash events.

[4]The ϕ index on the x-axis is staring at the physical zero of ϕ in the ATLAS coordinate system 0-31 (32-64) hence is the upper (lower) half of the HEC wheels.

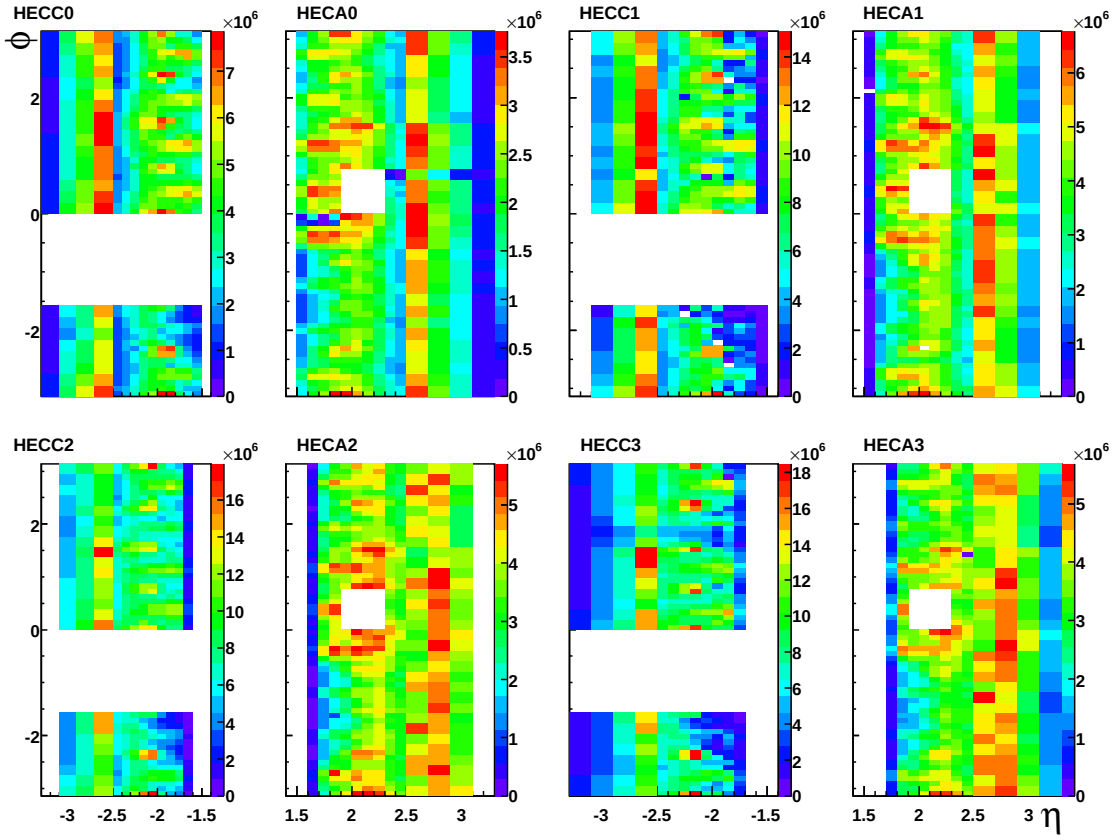

Figure 3.31: The accumulated cell energy in the η-ϕ plane of HEC for 86 single beam events where the beam was hitting a collimator on the c-side about 140 m before the interaction point. The periodic structure slightly visible on side C is due to the material in the endcap toroid magnets. At the time of this run, one quadrant of HEC C was not read out.

HEC A as compared to HEC C.
By scaling the response on side C to the response on side A, it was possible to compare the cell response assuming ϕ symmetry of the material distribution between the endcaps of ATLAS. Comparing the so normalised cell response over several bins in η, one could confirm the lower response in channels with reduced HV. In particular it was possible to find all but one channel in which the high voltage problems are expected to cause a reduction of the signal of more than 20%. The available statistics did not allow for a tagging of channels with smaller reduction in the response.

3.7 Influence of the Dead Power Supply in HEC C

As mentioned above and clearly visible in Figures 3.18, 3.20, 3.31 one quadrant of HEC C was not read out for some time due to a problem in the respective power supply, delivering the operational power to the pre-amplifiers in the HEC. In the affected region

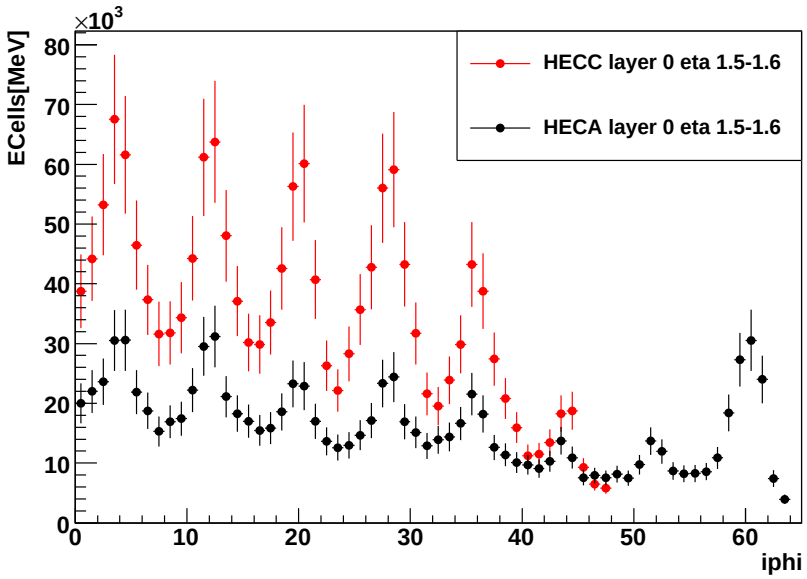

Figure 3.32: The cell energy vs. the phi index of the HEC A (C) modules is shown in black (red) for 85 single beam events where the beam was hitting a collimator about 140 m before the interaction point. The periodic structure is due to the material in the endcap toroid magnets (cf. Figure 3.33). The decrease for high phi indices (hence the lower half of the HEC wheels) is caused by additional material in the lower hemicycle around the beam-axis. At the time of this run, one quadrant of HEC C and one single FEB was not read out.

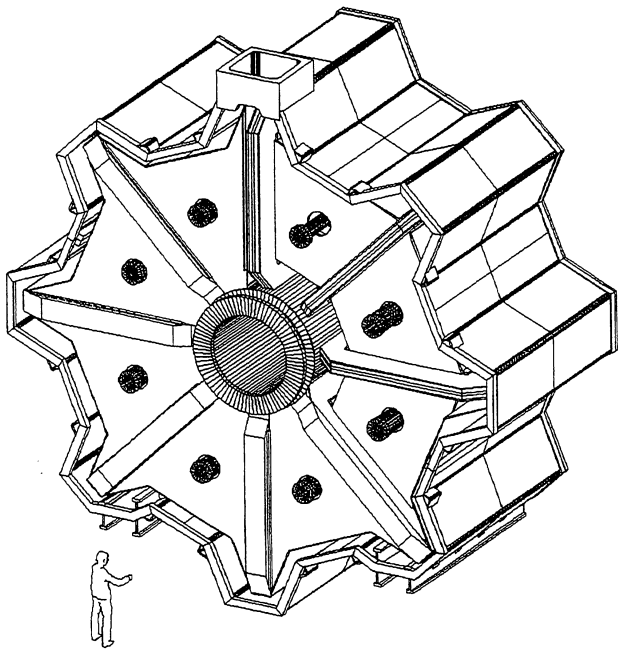

Figure 3.33: Sketch of an ATLAS endcap toroid [106].

of $-3.2 < \eta < -1.5$ and $-\frac{\pi}{2} < \phi < 0$ only the electromagnetic calorimeter coverage was given by the EMEC, and none of the sampling layers of the HEC could be read out.
As a consequence the energy measurement in this region had to be expected to be derogated. Using the information of the electromagnetic samplings, it was possible to get an estimate of the activity in this region. Tagging events with this signature thus was possible. Not only the energy of jets pointing to this region is expected to be underestimated, but also the reconstructed $E_{\mathrm{T}}^{\mathrm{miss}}$ is affected. Both its absolute value as even more severe its direction.
As the $E_{\mathrm{T}}^{\mathrm{miss}}$ will be used in the later presented top quark analysis, a small study, estimating the effect of this dead region to the resolution of $E_{\mathrm{T}}^{\mathrm{miss}}$ has been done. Figure 3.34 shows the difference of generated and reconstructed $E_{\mathrm{T}}^{\mathrm{miss}}$ on a simulated $t\bar{t}$ dataset, as function of the sum of the clusters E_{T} in the electromagnetic samplings of the affected region. The black histogram shows the case for the nominal detector configuration, the red histogram shows the detector configuration in which the quadrant of HEC C is not read out. Looking at the error bars representing the spread in the respective bin, it is clearly visible that the $E_{\mathrm{T}}^{\mathrm{miss}}$ resolution starts to degrade if more than 60 GeV are deposited in the affected region.

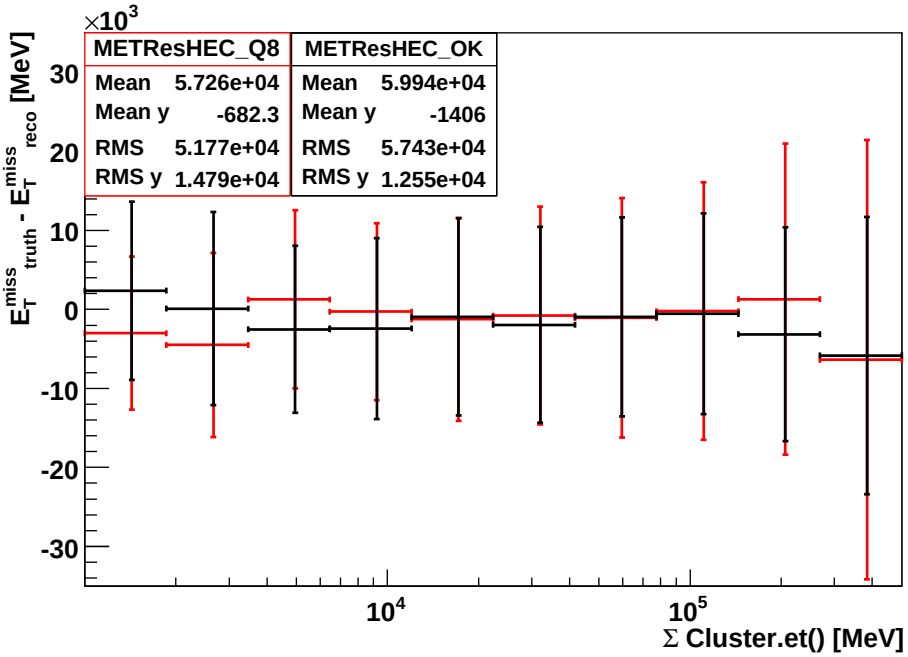

Figure 3.34: $E_{\mathrm{T}}^{\mathrm{miss}}$ resolution in simulated $t\bar{t}$ events with one HEC quadrant (Q8) off (red) and all quadrants on in black. The plot shows the difference between true and reconstructed $E_{\mathrm{T}}^{\mathrm{miss}}$ as function of activity (sum of cluster E_{T}) in the electromagnetic samplings of the relevant region.

Chapter 4

Physics Objects Reconstruction and Calibration

In Section 2.3 the *physics objects* were mentioned which are needed as a basis to perform physics analysis and thus have to be reconstructed in the detector. Describing the electronics readout in the calorimeter system, the previous Chapter 3 gave an example for electronic signal generation and processing in ATLAS. The electronics signals of the different subsystems have to be combined and the physics objects have to be derived in offline reconstruction algorithms. Athena [107] is the software framework of ATLAS which handles this task. Based on GAUDI [108,109], it is object-oriented, written in `C++` and steered with Python scripts. It is further interfaced with the analysis framework ROOT [110].
This chapter will give a brief overview of the reconstruction and calibration of physics objects. As in the preceding chapter, the emphasis will be on topics related to calorimetry, namely the energy reconstruction and calibration. There will be a particular focus on jet reconstruction and calibration, as it will be important in the top quark analysis presented in the following chapter.

4.1 Energy Reconstruction

Perturbative QCD describes jets as a manifestation of scattered partons, which after undergoing fragmentation are measured as collimated sets of hadrons in the detector. In physics analysis it is fundamental to be able to deduce the energy of the incident partons from the signals readout in the detector. This involves calibration of the readout signals, jet reconstruction and calibration of the physics objects. For many analyses, the uncertainties in this chain are the main source of systematic errors.
In the previous chapter (3) methods and relevant issues of signal calibration were discussed. On the basis of this electronics calibration, further steps are necessary in order to arrive at a complete calibration of the physics objects. This chapter will give a brief overview of the techniques used in ATLAS and will concentrate on the local calibration approach. Especially the non-compensating nature of the calorimeters in ATLAS necessitates a careful calibration for hadronic showers in the detector, but also jet level calibrations are of importance in order to be able to interpret the kinematics of jets as representations of the scattered partons.

The ultimate goal is to arrive at a level of calibration where the jet represents the momentum of the initially scattered partons. This is done in several steps: First, detector effects are corrected for in order to a achieve a scale at which the energy deposited in a calorimeter cell is correctly measured. In a next step, effects on jet level are addressed in order to arrive at a calibration scale at particle level, i.e. the reconstructed objects represent the final state particles after fragmentation (hadronisation) (cf. Section 4.2.1 and 4.2.2).
In a further step, physics effects such as clustering, fragmentation, initial state radiation (ISR), final state radiation (FSR) and the influence of the underlying events (UE) are accounted for. Ideally this leads to the final calibration scale at parton level. As these physics effects mostly depend on the nature and topology of the specific scattering process and the following decay, the final level of calibration is usually done with the help of *in-situ* calibration methods (cf. Section 4.3.1).

4.1.1 Clustering

Particles hitting the calorimeter mostly leave energy deposits in many cells, therefore it is necessary to build 3D cell groups in order to correctly assign the multiple energy deposits to the particle they stem from. Several methods are used, reaching from fixed sets of calorimeter cells, so called *calorimeter towers* to sophisticated clustering algorithms [111]. The *sliding window* algorithm uses a rectangular window of cells which is shifted such that the contained energy builds a local maximum. The fixed size of the resulting clusters simplifies calibration. However, the varying shape of particle showers and correspondence of particles to clusters is better accounted for in the technique of *topological clustering* [111]. It is therefore briefly discussed here.

Topological clusters are dynamically built by means of a decision based on the ratio of measured signal over expected noise, i.e. three cuts on the signal-over-noise-ratio ($|E/\sigma|$) are used. Cells are selected as cluster seeds if they pass a noise threshold cut. An iterative procedure adds neighbours of these seeds to the cluster if they pass the respective cut which is mainly used to suppress noise. Finally, cells in the perimeter of the cluster are included if they in turn pass the corresponding cut. The last cut often is very low in order not to cut into the tails of hadronic showers. For topological clustering it therefore is important to have a good knowledge of the expected noise, both the electronics and the pile-up contribution (cf. Figures 2.11, 2.12).
In test-beam analysis [112] it was found that the set of $|E/\sigma|$ cuts best suited for a compromise with good noise suppression while still effectively reconstructing low energy deposits is (4/2/0).
In the high multiplicity of LHC events, this clustering algorithm often leads to clusters which are growing over the borders of the actual showers. An additional step is therefore necessary to restore the possibility of identifying showers by individual particles. For this reason, clusters with more than one local maximum are re-grouped in a *cluster splitting* procedure.
Finally, one ends up with a list of 3D energy blobs which for di-jet samples correspond to about 1.6 stable particles[1]. The topological clusters thereby conserve the shape and

[1]This is close to the expectation of 4/3, as 1/2 of the stable particles in jets are photons from π^0 decays usually ending up in one cluster.

structure of the actual calorimeter shower to a good extent and allow for the study of the substructure of higher level objects i.e. the jets. As an example, figure 4.1 shows the cells in the different calorimeter layers which are included in a topological cluster, induced by a 163 GeV pion.

Independent of the method, the massless four-vectors of clusters or towers are then used

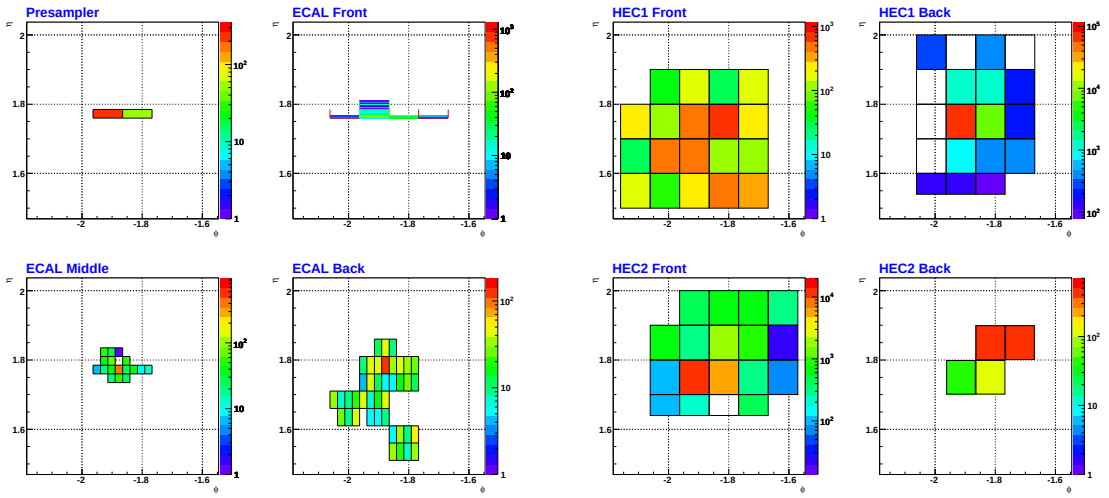

Figure 4.1: Example of a topological cluster in the EMEC and HEC using the set of thresholds (4,2,0) induced by a 163 GeV pion. The cells included in the cluster for the different sampling layers are shown, starting with the presampler and the three electromagnetic layers (left) and including cells in all four layers of the hadronic endcap. The colour code shows the energy in the cells in MeV on a logarithmic scale. The cells in white show negative energy content as they are noise induced.

as an input collection of proto-jets for the jet algorithms.

4.1.2 Jet-Making

As the final state partons initially produced in the proton-proton collisions hadronise directly after production, they leave their energy in the detector in multiple energy depositions spread around their initial direction (the above-mentioned clusters are meant to represent these on reconstruction level). The aim of jet making thus is to collect possibly all of these energy depositions and re-group them, building a jet, i.e. a massive four-vector, in a manner best representing the particle's four-vector. Jets, depending on the calibration procedure involved, are hence meant to be the reconstruction-level representation of either the hadrons or the initial partons (cf. Section 4.3). However, it should be reminded, that the observation of the initial partons is not possible due to the confinement of the strongly interacting particles. The recombination mechanisms during the parton shower hence complicate the definition of parton level jets which from a theoretical point of view often even are looked at as an ill-defined concept.

The four-vectors of the aforementioned towers or clusters are used as input objects (proto-jets) for jet-making algorithms. For the combination of proto-jets to a final jet, several

algorithms are known - a brief overview shall be given focusing on the ATLAS implementations.
From a theoretical viewpoint jet algorithms are required to be *collinear safe*, i.e. a jet algorithm should be giving the same result if one specific proto-jet were split up into two proto-jets carrying the same transverse momentum. They are further requested to be *infrared safe*, meaning that the addition of any soft particle should not alter the number of jets produced. Lastly, it is desired that the jet making results in the same hard process topology irrespective of the input object order, be it parton-, particle- or detector level objects (*order independence*). Two classes of jet algorithms are common in ATLAS, the fixed cone type and the sequential recombination type algorithms. As input they take any collection of four-vectors, be it generator or detector level objects.

Cone-Type Algorithms In ATLAS the cone-type jet algorithm is implemented as an iterative seeded fixed cone with split merge procedure:
The input collection is first ordered by decreasing transverse momentum p_{T}. If the highest p_{T} object exceeds the threshold $p_{\mathrm{T}\,seed}$, then all objects within $\Delta R < R_{cone}$ are combined with the seed. The four-vector sum of the now combined objects defines a new direction, along which the cone is aligned and the ΔR scan is repeated in order to collect further objects. This loop is iterated until the direction does not change with the subsequent iteration step. The cone now is regarded as stable and classified as jet. The whole procedure is repeated with all available seeds in the input collection.

As a result one ends up with a list of jets which possibly share constituents, i.e. objects of the input collection. Updating the direction of the cone after each iteration leads to cases in which objects formerly included in a cone are lost in the next iteration if they fail to fulfil the $\Delta R < R_{cone}$ requirement.
This algorithm thus is not *infrared safe* which partially can be recovered in the *split and merge* procedure: In the case of constituent sharing, jets are either merged or split in two, depending on the energy fraction of the shared constituents with regard to the less energetic jet.

Kt-Type Algorithms As standard implementation of a *sequential recombination type* algorithm ATLAS uses the kt-algorithm [113, 114, 115]. The kt-algorithm has several modes of operation and can be used on the basis of different recombination schemes (E, p_{T} , p_{T}^2 , E_{T} or E_{T}^2). Common to all flavours of the kt-algorithm is the principle of computing a distance measure both for pairs ij ($d_{i,j}$) of input entities with regard to each other and for each entity with regard to the beam axis ($d_{i,B}$).

$$d_{i,j} = min(k_i^{2p}, k_j^{2p}) \cdot \frac{\Delta R_{i,j}^2}{\mathbf{R}^2} \tag{4.1}$$

$$d_{i,B} = k_i^2 \tag{4.2}$$

where k is E, p_{T} , p_{T}^2 , E_{T} or E_{T}^2 depending on the recombination scheme chosen and p is 1 in the common case and -1 in the case of *anti-kt* [116]. The input objects are combined to jets, using mode dependent criteria for the values of d_{ij} and d_{iB}:

In the **inclusive mode**, object i and j are combined to form the new object k, if d_{min} is of the type d_{ij}, and in the input list i and j are replaced by k. If d_{min} is of the type d_{iB} then i is classified as a jet itself and removed from the input list. This procedure is repeated until the input list is empty and thus all input objects either have ended up in a jet or have become a jet themselves.

The **exclusive mode** is meant to separate the hard scattering process from the beam remnant or to select a specific event topology. It therefore has cut-off criteria which stop the iteration either if $d_{min} > d_{cut}$ or once the given number of jets has been found:
As before, d_{min} is computed and if $d_{min} > d_{cut}$ all remaining objects in the input list are classified as jets. If d_{min} is of the type d_{ij} then again i and j are combined to form k and in the input list i and j are replaced by k. If now d_{min} is of type d_{iB} then i is classified as a beam-jet, i.e. interpreted as a jet stemming from the proton remnant and hence discarded. This procedure is repeated until either the input list is empty or the required number of jets has been found.

If $p < 0$, especially if $p = -1$ the algorithm is referred to as **anti-kt**. In this case d_{ij} for soft particles is big and thus hard particles govern the combination decision. In particular soft particles cluster with hard ones rather than among each other. This has a significant influence on the jet shape; the jet boundary in this case is resilient with regard to soft particles, but flexible with regard to hard particles and thus offers very intuitive jet shapes and topologies.

The kt-algorithm does not feature constituent sharing between jets in any of its modes and is therefore *infrared safe*; furthermore, no seeds are being used and hence it also is *collinear safe*. These arguments are intuitive but might also be claimed for some of the cone-type algorithms, which actually do not fulfil these criteria. It is thus worth mentioning that the infrared and collinear safety of the kt-algorithm to all orders can be shown on theoretical ground.

4.2 Detector Level Calibration

4.2.1 EM Scale Calibration in ATLAS

As a first step of calibration the response of a calorimeter, the sampling fraction which is defined as the energy deposited in the active material over the sum of energies deposited in active and the absorber material, has to be known. The so defined sampling fraction is a geometry and material dependent property and hence varies with geometry and used material in the different calorimeters.
In the EMB, the sampling fraction is of the order of 16 - 20%, and as consequence of the accordion geometry varies with ϕ. The sampling fraction in the EMEC is of the order of 7 - 10% [117], and as the accordion is oriented perpendicular to the one in the EMB, varies with η. The simple geometry in the HEC modules keeps the sampling fraction constant in each wheel. In the HEC front wheel it is 4.4% and 2.2% in the rear wheel, where the absorber plates are twice as thick. In the case of the FCal it is difficult to extract the sampling fraction, as the geometry is not pointing at all and the sampling fraction is strongly dependent on the particles' incident angle, it is in the order of 1%. In order to correctly take into account all these variations and in order to measure the response of

the ATLAS calorimeters, modules of the different calorimeters were exposed to particle beams of known energy and with known particle content. The calorimeter response was studied and proportionality constants were deduced [69,70,71,72,73,74,75,76]. In the case of purely electromagnetic showers these constants are independent of the beam energy, the derived calibration scale therefore is referred to as *electromagnetic (em) scale*. It is expected to be the valid energy scale for showers initiated by photons and electrons.

4.2.2 Method of the Hadronic Calibration in ATLAS

The calorimeter response for hadronic showers (π) differs from the one for electromagnetic showers (e). The ratio e/π thus is an intrinsic property of each calorimeter and usually energy-independent. In the case of e/π< 1, as given for the calorimeters in ATLAS, the calorimeter is referred to as being *non-compensating*.
Several effects contribute to this lowered response in the case of hadron showers: Muons and neutrinos produced in decay channels of the weak interaction leave the calorimeter with practically no energy deposition. Together with parts of hadronic showers which are not fully contained in the calorimeter this constitutes the *leakage energy*.
The energy of particles stopped in the insensitive absorber layers, energy deposited in the breaking of nuclear bindings as well as a fraction of the neutrons produced in the nuclear reactions not contributing to the signal, constitute what usually is referred to as *invisible energy*.
Aiming at a full calibration of the calorimeter, the methods of hadronic calibration try to recover these losses. In ATLAS two different approaches are used: in the global methods reconstructed hadronic final state objects are subject to calibration, whereas the local method derives weights to calibrate detector level objects. In both methods it is fundamental to find observables discriminating showers predominantly consisting of electromagnetic particles from hadron showers as it is intended to apply the hadronic calibration to the latter only.

4.2.3 Global Methods

As mentioned before, the global methods are based on physics objects, namely jets. In most studies QCD di-jet samples reconstructed on electromagnetic scale with the seeded cone ($R_{cone} = 0.7$) algorithm were used [118, 119] with both towers and clusters used as input. The jets then are matched to truth jets, i.e. jets using stable MC generator particles as input, with the matching requirement of $\Delta R(\eta, \phi) < 0.2$.
To apply the calibration the matched jets are decomposed into energy deposits at cell level, which are then to be weighted with the corresponding calibration constant.
For classification into electromagnetic and hadronic showers, the energy density based method[2] exploits the fact that the former are observed to be much more compact and have a higher energy density while the latter are broader and less dense.
In order to actually derive the weights, the detector volume is divided into typical regions

[2] A similar method, the layer (longitudinal) weighting method is based on the observation that the electromagnetic fraction of hadronic showers depends on the depth of the shower.

and representative weights are computed by minimising:

$$\chi^2 = \sum_e \left(\frac{E^{(e)} - E^{(e)}_{truth}}{E^{(e)}_{truth}} \right)^2 , \tag{4.3}$$

where the sum runs over all events e, $E = \sum_i w_i E_i$ is the sum over all weighted cells i in the jet and $E^{(e)}_{truth}$ is energy of the matched truth jet.
An additional scaling factor as function of η and E_{T} then is applied in order to compensate remaining nonlinearities due to gaps and cracks in the detector as well as to accommodate differences in the used jet algorithms.
The result is a parametrised weighting function for a specific jet algorithm[3] consisting of cell energy density dependent calibration constants and additional final scale factors based on a specific physics sample.

4.2.4 Local Hadron Calibration

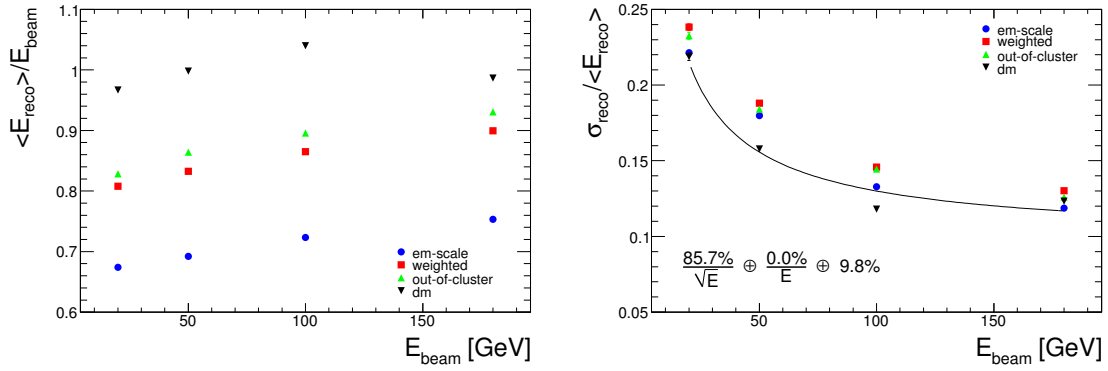

Figure 4.2: Validation of local hadron calibration in test beam measurements. Ratio (fitted mean) of reconstructed energy over the beam energy (left) and fitted resolution σ/E of the reconstructed energy (right) as function of the beam energy [120]. The different calibration steps are shown by the colour code: em-scale (blue), after hadronic weighting (red), after out-of-cluster corrections (green) and after dead-material corrections (black).

In contrast to the previously discussed global methods, the *local hadron calibration* is a bottom-up approach and aims at a calibration on detector object level by factorising the different calibration steps before the actual reconstruction of physics objects. In ATLAS local hadron calibration is done on top of topological clustering, exploiting the advantage of topological clusters conserving the shower structure. The relevant steps are shortly reviewed in the following. A detailed description is given in [120].

[3] with specific parameters e.g. $\Delta R = 0.7$, and specific input collection, e.g. calorimeter towers.

Classification

The classification into hadronic or electromagnetic clusters is done with the use of *cluster moments*. These are observables describing the shape and structure of clusters. Detailed MC simulations (using GEANT4 [121]) of charged and neutral pions impinging the detector are used to populate a phase-space spanned by four cluster observables[4]:
The observables are the cluster depth in the calorimeter λ, the energy density ρ, the cluster energy E_{clus} and the pseudo-rapidity of the cluster $|\eta_{clus}|$. In the case where the probability of finding a neutral pion in the respective phase-space bin exceeds 0.5, the cluster is classified as electromagnetic, otherwise as hadronic[5].

Weighting

As a result of GEANT4 simulations, *calibration hits* are objects which subdivide energy deposits in the calorimeter cells into visible electromagnetic, visible hadronic, invisible and escaped energy deposits. Calibration weights as $w_i = \left\langle E_{cell}^{true}/E_{cell}^{reco} \right\rangle$ can thus be derived from this detailed information, which are similar to the aforementioned weighting used in the global calibration methods. The weights are derived for each η region and sampling layer and for bins in cluster energy ($E_{cluster}$) and cell energy density (ρ_{cells}).

Out-Of-Cluster Corrections

As mentioned before, clusters are dynamically built objects based on the signal-over-noise ratio. In this procedure, energy deposits in cells sometimes are peculated in clusters if they fail the required thresholds. To recover these losses, out-of-cluster corrections are applied. In order to derive these out-of-cluster corrections the association of energy deposits outside clusters to nearby clusters has to be established and look-up tables are filled with the corresponding weights. This is done with the information available in *calibration hits*, assigning the fractional energy of each energy deposit to all clusters within the angular range but proportional to their total energy.
Similar to the weighting procedure, the so derived out-of-cluster corrections are then applied to the reconstructed clusters, depending on E_{clus}, $|\eta_{clus}|$, cluster depth λ and the clusters isolation. Out-of-cluster corrections can only account for those cases, where a signal cluster is present. On jet level additional corrections are needed for lost low-energy particles.

Dead Material Corrections

The local scope of this method brings about the necessity to correct for energy deposits in non-instrumented detector regions, the so-called *dead material corrections*[6]. In order to derive the corrections again *calibration hits* are used to assign energy deposited in

[4] Two other methods, the cone and the layer method were also studied in ATLAS , but are currently not in use [120].

[5] Noise clusters can have negative energy and are classified as unknown.

[6] For 20 GeV single pions these corrections, depending on the η region, can make up to 30-70% of the initial energy.

upstream material, the calorimeter crack and cryostat walls as well as leakage energy to the reconstructed clusters. For some of these regions, correlations with specific calorimeter samplings can be exploited in order to correctly assign the dead material energy to the respective clusters[7]. For other regions, however, no significant correlations are at hand and the lost energy has to be assigned according to look-up tables binned in E_{clus}, $|\eta_{clus}|$ and cluster depth λ.
As in the case of weighting and out-of-cluster corrections, the dead material corrections are applied to reconstructed clusters according for the respective bins in the look-up tables.

Figure 4.2 shows an example of the linearity (left) and resolution (right) achieved with local hadron calibration on test beam data. The initial *electromagnetic* scale is shown in blue, the scale after application of the hadronic weights is shown in red. Finally, the scale after the application of out-of-cluster and dead-material corrections is shown in green and black, respectively.

4.3 Jet Level Calibration

Even the local calibration approach calls for some corrections on jet level, as they are genuine jet-level features. Misclassification of clusters e.g. leads to an underestimation of the energy response of roughly 3% for jets with a p_{T} of 150 GeV [119]. Another effect are particles not ending up in the jet, be it due to jet acceptance or because their signal is below the threshold for clustering. For a jet of 150 GeV p_{T} , it is estimated that the latter constitutes a 3% effect while particles bent out of the jet acceptance by the magnetic field are estimated to cause a 2% effect [119][8].
The aim is to find universal methods to calibrate on jet level, independent of the precedent detector level calibration. Several methods have been developed and are under study. They can be divided into two classes: With the first type, jets are calibrated to particle level, i.e. the energy of the particles after hadronisation is recovered. A method exploiting jet shape variables which is currently under development is an example thereof. These methods tend to be independent of the physics process and are meant to deal with the aforementioned jet-level features. The second type are methods to calibrate the jets to parton level, i.e. at the level of the interaction before hadronisation. This is the case for most in-situ methods which use a specific physics channel or decay topology. These methods are sensitive to quark and gluon content, the parton momentum scale and multiple parton interactions and therefore are physics-sample dependent.
In addition, methods using information from the tracking system of ATLAS have been studied. So-called energy flow methods, for example, match particle tracks measured in the tracking detectors to the jets measured in the calorimeter system and hence combine the momentum and energy measurement of the different detector systems. In order to correctly calibrate jets induced by heavy flavour quarks, which show a lower response in the calorimeter due to their leptonic decays, methods using soft leptons to tag these jets are under study. A detailed overview can be found in [119].

[7] e.g. for the outer cryostat wall between the last LAr and first Tile sampling the geometrical mean of the deposited energy in these samplings is used.

[8] An additional effect might be caused by the fact that local hadron calibration is based on simulations of *single* particles for which the response might slightly differ from the case of a LHC event with high multiplicity.

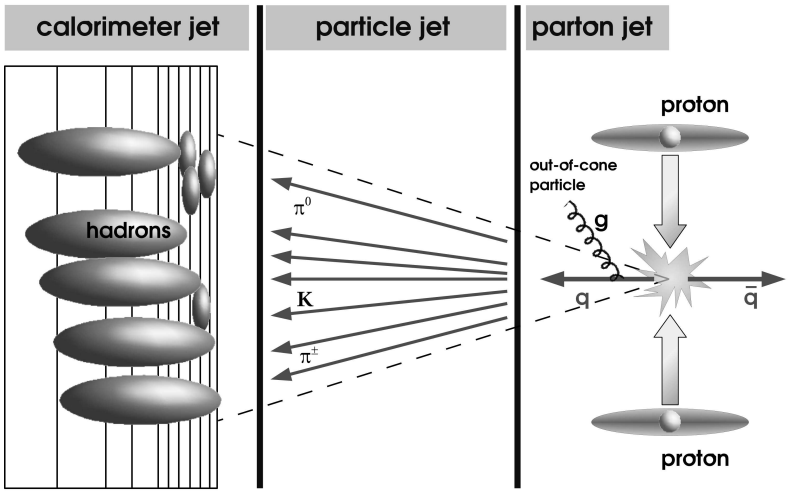

Figure 4.3: Schematic of the jet energy scale corrections, taking energy measurements on the calorimeter level to the particle or the parton level [122].

4.3.1 In-Situ Calibration

In order to validate the jet energy scale, several *in-situ* calibration approaches have been prepared in ATLAS. With first data it will be important to validate the response uniformity throughout the calorimeter. Di-jet events from processes which at leading order are two-body decays are a good testing ground, as the two jets are expected to be balanced in p_{T}. In reality, more than one jet per side might be found and hence subtle studies need to be performed [119], their principle idea being to look at p_{T} balance and jet rates to validate the uniformity both in η and ϕ. In a further step, the electromagnetic scale can be related to the hadronic scale using γ or $Z \to \ell\ell$ plus jets events requiring p_{T} balance of the hadronic and the electromagnetic side. For very high jet energies methods have been proposed which use leading jets in QCD multi-jet events and balance those jets against the remaining jets (which are expected to be calibrated with the former methods).
In the $t\bar{t}$ channel these methods however can not be applied directly - not only because of the more complex event topology, but also because of the jets in these events are of different origins and hence of different nature. Jets from light quarks, as well as from b quarks and from gluons are present and as they show different fragmentation behaviour and neutrino content, the resulting calibration factors will differ by a few percent. Also the underlying event in a $t\bar{t}$ event is expected to be different from the one in di-jet events. The use of the $W \to jj$ from the top quark decay itself therefore seems to be an appropriate in-situ calibration. Two methods have been shown in [119], a template method which uses template histograms with different energy scales α and various relative energy resolutions β. The χ^2 between the template histograms and the data is then minimised in the (α, β) bins to find the appropriate scaling constants. The template method is intended to measure the bare jet energy scale, i.e. the level of energy calibration in the respective jets.
As an alternative, the iterative method measures the effective jet energy scale which does not reflect the bare jet energy scale, but will lead to W boson and top quark masses with the correct values. It was used in the analysis presented here and will be briefly described.

Iterative Method for Light Jet Energy Scale in $W \to jj$

The precise knowledge of the W boson mass is taken as a reference in order to extract the jet energy scale for light jets in the top decay.
In the approximation of massless jets, the invariant mass of the two-jet system with energies E_1 and E_2 and an opening angle Θ_{jj} can be written as:

$$M_{jj} = \sqrt{2E_1E_2(1 - cos(\Theta_{jj}))} \tag{4.4}$$

As the angle between the two jets in the hadronic W decay is measured without significant bias for most jet-jet pairs, any deviation of M_{jj} stems mainly from the energy mis-calibration.

The mean value of the invariant jet-jet mass distribution would match the PDG W boson mass value if the jet energy scale were exact. In order to scale the actual jet energy scale, the factors K(E1) and K(E2) are introduced:

$$M_W^{PDG} = \sqrt{2(K(E_1)E_1)(K(E_2)E_2) \times (1 - cos(\Theta_{jj}))} = \sqrt{K(E_1)K(E_2)}\ M_{jj} \tag{4.5}$$

If the jet calibration is taken to be independent of the jet energy (K = K(E1) = K(E2)), the scale factor K can be written as $K = M_W^{PDG}/M_{jj}$. This simplified rescaling results in an effective jet energy scale, taking into account all biases introduced in the jet selection. In order to better reflect the expected dependency of the calorimeter response on jet energy and jet pseudo-rapidity, for different bins of these quantities, invariant mass distributions of the jet pairs are built and the W mass is extracted.
The rescaling is repeated in I iterations, and at each iteration j the rescaling factor in bin i (K_i^j) is extracted and applied in the subsequent iteration, each time resulting in a further rescaled mass spectrum. The final calibration function thus is:

$$K_i = \prod_{j=1,I} K_i^j \tag{4.6}$$

4.4 $E_{\mathrm{T}}^{\mathrm{miss}}$ Reconstruction

In order to reconstruct the missing transverse energy ($E_{\mathrm{T}}^{\mathrm{miss}}$), the sum of the transverse energy of five components is determined: The energy of cells in identified electron or photon clusters; the energy of cells inside jets; the energy of cells in topological clusters, outside identified objects; the momenta of muons reconstructed in the muon spectrometer; and corrections for energy deposited in non instrumented regions such as the cryostats. The vector balancing this sum in the transverse plane then defines $E_{\mathrm{T}}^{\mathrm{miss}}$.
The sum of the transverse energy in the lepton plus jets decay channel of the $t\bar{t}$ system is about 500 GeV, which gives a typical $E_{\mathrm{T}}^{\mathrm{miss}}$ resolution of the order of 10 GeV [119].

4.5 Electron Reconstruction

With information of the calorimeters and inner tracker of ATLAS, electron candidates are reconstructed and identified in the pseudo-rapidity range $|\eta| < 2.5$. Several reconstruction

algorithms are used to classify the electron candidates.
For the standard reconstruction of electrons [65], a seed cluster in the electromagnetic calorimeter is required. A loosely matching track is searched for among all tracks reconstructed in the inner detector. If a photon conversion is reconstructed in the inner detector, the electron candidate is dismissed. Shower-shape variables, combined reconstruction properties, such as the ratio of energy (measured in the calorimeter) to momentum (measured in the inner detector), the difference between the coordinates η and ϕ reconstructed by the cluster and the track extrapolated into the calorimeter, and the ratio of high-threshold transition radiation hits to low-threshold hits on the track, are used to identify electrons. With these variables, an electron candidate is defined as a `ElectronTight` identified by the `egamma` algorithm: By requiring tight track-matching criteria and a tight cut on the energy-momentum ratio, by explicitly requiring a hit in the vertexing-layer, to further reject photon conversions, and finally by requiring a high ratio between high-threshold and low-threshold hits in the TRT detector (to further reject the background from charged hadrons).
For further cuts on the isolation, the electron isolation is measured based on energy reconstructed in the calorimeters: the additional transverse energy E_{T} of objects reconstructed in a cone with radius $\Delta R = 0.2$ around the electron axis is required to be less than 6 GeV. For electrons with a p_{T} above 20 GeV and $|\eta| < 2.5$ outside the crack region, the average identification efficiency in $t\bar{t}$ events is about 67%, with a purity of about 97% [119]. The expected electron fake rate, defined as the rate at which an object that is not associated with a true electron is mis-identified as an electron, is in the order of $\mathcal{O}(10^{-5})$ [123, 119, 124].

4.6 Muon Reconstruction

Muons are reconstructed in the pseudo-rapidity range of $|\eta| < 2.5$, using information from the muon spectrometer and the inner detector. The muon reconstruction [119, 65] is performed using e.g. the `StacoMuon` algorithm, it defines muons using a statistical combination of the muon chambers and the tracker information. First track segments are built in each of the three muon spectrometer layers, and then they are linked together to form tracks. These tracks are extrapolated to the beam line, accounting for both multiple scattering and energy loss in the calorimeter. The muon spectrometer tracks are then paired with inner detector tracks to identify combined muons. The match χ^2, defined as the difference between outer and inner track vectors are weighted by their combined covariance matrix.
Also the muon isolation is measured based on energy reconstructed in the calorimeters: the additional transverse energy E_{T} of objects reconstructed in a cone with radius $\Delta R = 0.2$ around the muon is required to be less than 6 GeV. For muons with a p_{T} above 20 GeV, the average reconstruction efficiency in $t\bar{t}$ events is 88%. The fake rate, defined as the rate at which an object that is not associated with a true muon is mis-identified as a muon, is 0.1 ± 0.01 % [119].

Chapter 5

Top Quark Mass Reconstruction with Local Hadron Calibration

In the following chapter an analysis of $t\bar{t}$ decays in the 'lepton plus jets' channel shall be discussed. It is intended to be applied to the first collision data available for ATLAS. The integrated luminosity chosen for this study thus was 145 pb^{-1}, which corresponds to the integrated luminosity expected to be accumulated during the first physics run of LHC at a centre of mass energy of 10 TeV scheduled for fall 2009. For the very early data the detector will not yet be fully understood and calibrated in detail, and the early analysis methods are thus required to be rather simple and robust. Also, some of the physics object reconstruction methods will not yet be understood in detail and will not be performing at the desired level. Particularly b-tagging algorithms are not used in this analysis for this reason.
The analysis was performed within the ATLAS software framework Athena release 14.5.2. The analysis package itself was coded in `AthenaROOTAcess` and is available at [125].
In the so called 'lepton plus jets' decay channel of the $t\bar{t}$ system, one of W bosons decays leptonically while the W boson of the other top quark decays hadronically. This decay channel is an obvious choice for such an early analysis: The lepton offers a rather clean trigger signature for the event, and hence facilitates background suppression. For the actual measurement, the top quark decaying into jets only is used, as all its decay products are directly reconstructible - in contrast to the neutrino in the leptonic decay channel.
In this analysis, the distribution of the invariant mass of the three jets constituting the top quark candidate is used as estimator for the top quark mass. The interpretation of its peak as top quark mass is expected to correspond to the pole mass of the top quark. However, as sketched in Chapter 1, the mass of a quark is convention-dependent and intrinsically ambiguous.
The method used here for reconstructing the top quark is based on simple cuts and is similar to the one that was proposed in [126, 127]. After cleaning the sample with event selection cuts, for each event the top quark candidate is chosen by selecting the jet triplet which has the largest p_{T}.
The $t\bar{t}$ events are selected by requiring an isolated lepton, cuts on the jet multiplicity and a cut on $E_{\text{T}}^{\text{miss}}$, corresponding to the neutrino. In the following, the different datasets used for this analysis will be presented: Namely the signal process, where the $t\bar{t}$ system decays into a electron or a muon, the corresponding neutrinos and jets, and several other

processes which also pass the selection cuts and hence have to be treated as background. In particular the decays of the $t\bar{t}$ system into a τ lepton, its neutrino and jets, the di-leptonic $t\bar{t}$ decay and the all-hadronic $t\bar{t}$ decay are important background.

5.1 Monte Carlo Datasets

As mentioned in Chapter 1, the relevant physics processes can be described using a factorisation ansatz, separating the interaction into a short distance part, the hard scattering process, and a long distance part, which is represented by PDFs. This allows the use of Monte Carlo (MC) generators to simulate data. For this analysis, a set of simulated data was used, representing the relevant physics processes both in the signal and background decay channels, which had been simulated with MC generators.
The leading order programs Alpgen [49] (version 2.13 and CTEQ6L1 [37] as PDF) and AcerMC [47,48] (version 3.5) as well as the next-to-leading order program Mc@nlo [1] [50] (version 3.31 and CTEQ6M as PDF) were used for the generation of the hard process of the different samples. The parton showering and hadronisation as well as the underlying event was then simulated using Herwig [23], Jimmy [128] (version 6.510 and CTEQ6L1 as PDF) and Pythia [22] (version 6.417 and CTEQ6L1 as PDF).
The different datasets were simulated at different orders and thus with different cross-sections. This was correctly taken into account by a matching scheme and the use of K-factors. A short overview over the MC generators and this procedure has been given in Section 1.3.
Finally, the response of the detector to the generated physics particles was simulated in a detector simulation using Geant4 [121]. This procedure results in datasets for different physics channels and detector configurations on which the standard algorithms for reconstruction of physics objects are applied (cf. Chapter 4).
For all datasets the input parameters were set according to the values in [129][2], in particular the mass of the top quark was set to 172.5 GeV and for the W boson to 80.403 GeV. In the current schedule for LHC start-up, it is foreseen to start with colliding proton beams at a centre-of-mass energy of 10 TeV. For this reason, the datasets hence were simulated with the corresponding energy and cross-sections. In addition, the detector configuration for the datasets used here represents the status of ATLAS in fall 2008, when one quadrant of HEC C could not be read out (see Section 3.7). Even though the problem is now fixed, the datasets allowed the study to be performed in a realistic, or hopefully even pessimistic detector configuration. The datasets as produced in the `mc08` simulation campaign in ATLAS which were used in this study are listed in Table 5.1. The generators used as well as a short description will be given in the following.

5.1.1 Signal Simulation

With Mc@nlo, the $t\bar{t}$ production was simulated using next-to-leading order calculations, which include diagrams with one additional parton in the final state. The parton density

[1] All events produced by Mc@nlo carry a weight of $\pm$ 1 to allow for a correct modelling of the full phase space (cf. Sec. 1.3). This weight has to be taken into account when filling the histograms. The error bars in the shown histograms represent the appropriate sum-of-weights error.

[2] for the bottom/charm quarks, each generator's (each process's) default values were used, rather than the PDG values

function used was CTEQ6M. Hadronisation and underlying event were simulated using Herwig and Jimmy, respectively. At generator level no cuts were applied, except for lepton flavour selection in order to be able to subdivide the sample into separate datasets depending on the decay of the W boson. This way one 'not-all-hadronic' dataset, containing events of the all leptonic and the lepton plus jets decay channel, and an 'all-hadronic' dataset, containing the events of the all hadronic decay channel, was available. The two datasets of the $t\bar{t}$ production contain both signal and background events: In the case of the 'non-hadronic' dataset, the events with a W decaying into an electron or a muon are regarded as signal events. However, the events where the W decays into a τ or where both W decay leptonically have to be regarded as physics background. The events with a τ in the final state pass the selection criteria only if the τ can be mis-reconstructed as an electron or muon, i.e if the τ decays leptonically.
Like the signal events, the di-leptonic events also have a sizable $E_{\mathrm{T}}^{\mathrm{miss}}$ signature stemming from the two neutrinos but usually show a lower jet multiplicity. These events only pass the jet requirements if a jet is faked by an electron or if the ISR/FSR or the underlying event are such that additional jets are found. In the case of the decay into two τs, the hadronic τ decay could also cause an additional jet to be found.
Events where both Ws decay hadronically pass the selection cuts, if one of the jets fakes an electron and if the neutrinos from a semi-leptonic decay of a heavy-flavour quark are able to pass the $E_{\mathrm{T}}^{\mathrm{miss}}$ requirement.

5.1.2 Physics Background Simulation

Single Top Quark Production

The different single top quark production processes were briefly sketched in Chapter 1. In the case of the s-channel and t-channel, with a leptonic decay of the W, the lepton and $E_{\mathrm{T}}^{\mathrm{miss}}$ criteria are fulfilled. However, the jet multiplicity of these events is too low, such that the jet requirements are passed only if the ISR/FSR or the underlying event are such that additional jets are found.
In the case of the Wt-channel with a leptonic decay of the associated W boson the signature is the same as for signal events, however the jet multiplicity is only three and again an additional jet from ISR/FSR or from the underlying event is necessary to pass all selection criteria.
At LHC the Wt-channel contributes about 77%, the t-channel about 20% and the s-channel[3] with 3% to the total cross-section of single top production. As shown in Table 1.2 these fractions vary slightly depending on the centre of mass energy at which LHC is operating. The AcerMC matrix element generator was used for the simulation of single top quark production, again followed by a hadronisation simulation with Pythia using CTEQ6M. The t-channel generation method is based on a method combining LO and tree level NLO diagrams. The s-channel and Wt-channel are generated at LO accuracy only. For all three production channels, W bosons were forced to decay leptonically at generator level in order to select the relevant background topology. Particularly for the case of Wt-channel, either the associated W bosons or the W bosons from top quark decay were forced to decay leptonically and no di-leptonic events are included.

[3]For this channel no data set was available hence it could not be included in this study.

Inclusive $W \to \ell\nu$ and $Z \to \ell\ell$ Plus Jets Decays

The most important background process is W boson production associated with multiple hard gluon radiation of the initial/final state partons. If the W decays leptonically the lepton and $E_{\mathrm{T}}^{\mathrm{miss}}$ criteria are met and due to the gluon radiation the jet multiplicity can be high enough to pass the selection cuts.
The contribution of $Z \to \ell\ell$ + n jets events is non-negligible only when there is at least one jet in addition to the Z, and the $E_{\mathrm{T}}^{\mathrm{miss}}$ is either mis-reconstructed or coming from the decay of the τ or a semi-leptonic decay of a heavy-flavour quark. Events with $W \to jj$ and $Z \to \ell\ell$ plus jets production have been simulated using the Alpgen generator. Herwig has been used for the simulation of the fragmentation and the hadronisation and Jimmy for the underlying event. In order to separate the samples such that each has a given number of partons, the MLM [130] algorithm has been used to match the parton shower and the matrix element calculations. A fraction of this background contains heavy quarks. This background is treated separately in Alpgen by producing W+$b\bar{b}$ and W+$c\bar{c}$ (plus light jets) samples.

Di-Boson Processes

Di-boson events produced with light jets can also be a background to the $t\bar{t}$ signal, if one boson decays leptonically and additional jets from the underlying event or ISR/FSR are found. WW, WZ and ZZ processes with all decay modes have been generated with Herwig and a filter was applied to select those events with an electron or a muon with $p_{\mathrm{T}} > 10$ GeV. WW events with the W boson decaying leptonically into final states with two electrons, an electron (muon) and a τ-lepton or two τ-leptons have been generated with Mc@nlo, and Herwig was used for the hadronisation and fragmentation.

QCD Processes

QCD multi-jet processes can pass the selection cuts, if the lepton criteria are fulfilled by an electron or muon from a semi-leptonic decay of a heavy-flavour quark or if jets fake electrons (e.g. pions) or muons (punch-through). And if the $E_{\mathrm{T}}^{\mathrm{miss}}$ criteria are fulfilled either by the corresponding neutrino in the semi-leptonic decay of a heavy-flavour quark or if the $E_{\mathrm{T}}^{\mathrm{miss}}$ is mis-reconstructed. These events hence are background to $t\bar{t}$ analysis and have to be taken into account. The level of QCD multi-jet background has large uncertainties with the currently available generation tools, which are based on a leading order description: Pythia has been used to generate these events with the same matching as used for the W plus jets samples. Given the large cross-section for this process, the simulation of these events is very CPU intense and in the current ATLAS production QCD was simulated only for a very low integrated luminosity. For the same reason, at the TeVatron experiments QCD background was extracted from collision data rather than from simulation. With the even higher cross-sections at LHC this will also be the way to obtain reliable values for ATLAS. On studies using simulated data only rough estimates can be given, especially for QCD processes at low momentum transfer.
As these samples had an integrated luminosity in the order of 0.006 to 0.1 pb^{-1} and hence corresponded to less than one per-mil of the needed integrated luminosity of 145 pb^{-1}, a small study on generator level was done in combination with an estimate of the lepton

fake rate obtained from the available fully simulated datasets. It will be presented in Section 5.2.7.

5.2 Event Selection

As shown in Figure 1.6 the events to be reconstructed show a final state with two b quark jets, two light quark jets from the W boson decay and one electron or muon with the corresponding neutrino. In the following the cuts used for selecting this topology are explained. The definition of the different physics objects and the reconstruction algorithms used, have been discussed in Chapter 4.

5.2.1 Trigger

In order to trigger the events to be analysed, a lepton trigger is the obvious choice, as it has the highest background suppression. In early data taking, the trigger menus will not be fine-tuned, therefore the triggers chosen for this study were relatively loose. The electron channel was triggered using the trigger menu of the event filter `EF_e20_loose`, which requires an electron with an E_{T} of 20 GeV. The muon channel was triggered using the trigger menu `EF_mu20`, which requires a muon with an E_{T} of 20 GeV.
For both channels the trigger efficiency shows a turn-on curve, and at a p_{T} of about 30 GeV for the reconstructed leptons the plateau is reached. For electrons the efficiency then is about 97%, for muons about 90%. This difference is explained by the difference in acceptance of the two trigger systems: The acceptance of the muon trigger system is more limited than the one of the electron trigger. For $|\eta|$ less than 1.0 the muon trigger coverage is approximately 80% as some cracks, needed to accommodate inner-detector and calorimeter services, are present; hence the muon trigger is less efficient.

5.2.2 Lepton Selection

Exactly one lepton with a p_{T} of more than 20 GeV within the pseudo-rapidity range of $|\eta| < 2.5$ was required as the first event selection cut. In the case of muons, the reconstructed muon with the `StacoMuon` algorithm was used. The `StacoMuon` algorithm is using a combination of inner detector and muon system information. In the case of electrons, the reconstructed electron was required to fulfil the tight isolation criterion `ElectronTight` of the electron reconstruction algorithm `egamma`. The transverse energy reconstructed in a cone of $\Delta R < 0.2$ around the lepton direction was not allowed to exceed 6 GeV. This cut corresponds to the trigger selection and is used especially to reduce background from the all-hadronic decay channel of the $t\bar{t}$ system as well as to suppress QCD background. In order to reduce the background due to semi-leptonic decays of heavy-flavour quarks, muons overlapping with a jet ($\Delta R < 0.4$) where not accepted in this selection step.

5.2.3 Jet Selection

At least 4 jets with a p_{T} of more than 20 GeV, three of which also pass the p_{T} cut of 40 GeV were required to pass the event selection. The jets used were reconstructed with

Process	sample	σ [pb]	K-factor	σ x K-factor [pb]	preselection eff
$t\bar{t}$ Mc@nlo r541	105200	202.86	1.07	217.06	0.72092
$t\bar{t}$ Mc@nlo r579	105200	202.86	1.07	217.06	0.72387
$t\bar{t}$ NC@NLO all had	105204	170.74	1.07	182.69	0.81563
$t\bar{t}$ Mc@nlo (m_t 160,fastsim)	106203	295.96	1.06	313.72	0.71594
$t\bar{t}$ Mc@nlo (m_t 170,fastsim)	106201	220.66	1.06	233.9	0.72395
$t\bar{t}$ Mc@nlo (m_t 180,fastsim)	106202	166.82	1.06	176.83	0.72838
Single top Wt (non-hadronic)	105500	14.41	0.99	14.27	0.64706
Single top t-chan (non-hadronic)	105502	41.42	0.98	40.59	0.52704
Single top s-chan (non-hadronic)	105501	dataset not available			
$W \to e\nu$ +2 parton	107682	676.1	1.22	824.84	0.45939
$W \to e\nu$ +3 parton	107683	205.3	1.22	250.47	0.56062
$W \to e\nu$ +4 parton	107684	57.45	1.22	70.09	0.61793
$W \to e\nu$ +5 parton	107685	17.86	1.22	21.79	0.68923
$W \to \mu\nu$ +2 parton	107692	682.5	1.22	832.65	0.24508
$W \to \mu\nu$ +3 parton	107693	203.9	1.22	248.76	0.62576
$W \to \mu\nu$ +4 parton	107694	57	1.22	69.54	0.76311
$W \to \mu\nu$ +5 parton	107695	17.59	1.22	21.46	0.82943
$W \to \tau\nu$ +2 parton	107702	672.8	1.22	820.82	0.09270
$W \to \tau\nu$ +3 parton	107703	204.58	1.22	249.59	0.18255
$W \to \tau\nu$ +4 parton	107704	56.79	1.22	69.28	0.28683
$W \to \tau\nu$ +5 parton	107705	18.37	1.22	22.41	0.36086
$Z \to ee$ +2 parton	107652	62.3	1.22	76.01	0.74891
$Z \to ee$ +3 parton	107653	18.76	1.22	22.89	0.83056
$Z \to ee$ +4 parton	107654	4.97	1.22	6.06	0.90233
$Z \to ee$ +5 parton	107655	1.43	1.22	1.74	0.95600
$Z \to \mu\mu$ +2 parton	107662	63.5	1.22	77.47	0.32136
$Z \to \mu\mu$ +3 parton	107663	18.7	1.22	22.81	0.75324
$Z \to \mu\mu$ +4 parton	107664	4.99	1.22	6.09	0.89955
$Z \to \mu\mu$ +5 parton	107665	1.37	1.22	1.67	0.94414
$Z \to \tau\tau$ +2 parton	107672	62.63	1.22	76.41	0.24215
$Z \to \tau\tau$ +3 parton	107673	18.86	1.22	23.01	0.39468
$Z \to \tau\tau$ +4 parton	107674	4.98	1.22	6.08	0.55038
$Z \to \tau\tau$ +5 parton	107675	1.39	1.22	1.7	0.64198
($W \to b\bar{b}$ or $W \to c\bar{c}$)+0 parton	106280	5.13	1.22	6.26	0.25200
($W \to b\bar{b}$ or $W \to c\bar{c}$)+1 parton	106281	5.01	1.22	6.11	0.47243
($W \to b\bar{b}$ or $W \to c\bar{c}$)+2 parton	106282	2.89	1.22	3.53	0.57523
($W \to b\bar{b}$ or $W \to c\bar{c}$)+3 parton	106283	1.61	1.22	1.96	0.64600
WW	105985	15.62	1.69	26.4	0.45693
ZZ	105986	1.36	1.42	1.93	0.57970
WZ	105987	4.87	1.81	8.82	0.49405
Pythia jetjet E_T 35-70	105011	5.62e7	1	56152200	0.04739
Pythia jetjet E_T 70-140	105012	3.24e6	1	3241570	0.14041
Pythia jetjet E_T 140-280	105013	1.51e5	1	150900	0.24123
Pythia jetjet E_T 280-560	105014	5.18e3	1	5178.61	0.29228
Pythia jetjet E_T 560-1120	105015	1.12e2	1	111.95	0.29173

Table 5.1: Data sets used within this analysis. The cross-sections, K-factors and the efficiencies of the preselection are shown [131]. The cross-sections of the samples include the respective branching ratio, the MLM matching efficiency and generator filter efficiency (if any).

the Kt4 (Anti-Kt4) algorithm on local hadron calibrated clusters (cf. Section 4.1.2). Jets overlapping with electrons were marked and not considered in this event selection cut. Also, for the later reconstruction of the top quark candidates, jets with a $\Delta R < 0.4$ to a selected electron or muon where not used, as electron and jet reconstruction are not exclusive in ATLAS. The same rejection was used for muons, too, in order to avoid a non-equal treatment of the two decay channels.

5.2.4 $E_{\mathrm{T}}^{\mathrm{miss}}$ Selection

Especially in order to reduce QCD background, a missing transverse energy of more than 20 GeV was required as a further event selection cut.
The used MC samples were simulated with a detector configuration in which a part of the calorimeter was not read out as this was really the case for the first couple of months of ATLAS operation. This naturally has an impact on the $E_{\mathrm{T}}^{\mathrm{miss}}$ reconstruction, especially on the direction and $E_{\mathrm{T}}^{\mathrm{miss}}$ resolution. As shown in Section 3.7, the $E_{\mathrm{T}}^{\mathrm{miss}}$ reconstruction, however, is good enough to keep this selection cut. The top quark reconstruction itself is not affected as only the hadronically decaying top quark is reconstructed for which the $E_{\mathrm{T}}^{\mathrm{miss}}$ object itself is of no use.

5.2.5 HEC Region Cut

Events with activity in the region of $-3.2 < \eta < -1.5$ and $-\frac{\pi}{2} < \phi < 0$, where the HEC was not read out (cf. Section 3.7), had to be rejected as a jet pointing to this region would not have been correctly reconstructed. The electromagnetic calorimeter, however, was read out in this region, and only the information of the hadronic calorimeter was not available. Using the energy measured in the electromagnetic samplings, it was possible to tag events with such a topology. In particular, the event was rejected if a jet with a p_{T} of more than 10 GeV was found within the region.

5.2.6 Cut Flow

In accordance with the ATLAS computing model and in order to facilitate data handling, the MC samples available as Analysis Object Data (AODs) on the grid where skimmed and Derived Physics Data (DPDs) were produced. The skimming included a preselection based on the same type of criteria as in the event selection, but with largely relaxed cut values. The preselection required one lepton with a p_{T} of more than 10 GeV, three jets with a p_{T} above 10 GeV, two of which also pass a p_{T} of 20 GeV. Due to the dead region in the HEC, no $E_{\mathrm{T}}^{\mathrm{miss}}$ cut was required in the preselection. The efficiency of the preselection is shown in Table 5.1. Using the standard model cross-sections, a sample corresponding to an integrated luminosity of 145 pb^{-1} was mixed from the DPDs, correctly taking into account the efficiencies of the preselection. Figure 5.1 shows the effect of the applied selection cuts for the different samples. The selection efficiency for each of the samples is shown in Figure 5.2. The signal channels again are the $t\bar{t}$ decays into jets plus electron or muon. The histogram labelled *tau* contains both the lepton plus jet and di-leptonic $t\bar{t}$ decays in the τ channel, whereas the di-lepton channel here is defined as the $t\bar{t}$ decay into muons and electrons only.

The trigger requirement and the lepton cut clearly show a strong reduction of the all-hadronic $t\bar{t}$ decay and the QCD background. The first jet cut, requiring at least 4 jets with a p_{T} of more than 20 GeV effectively reduces the W/Z plus jets as well as the di-boson background. With a smaller but still important efficiency, this background is further reduced by the second jet cut, requiring at least three jets with a p_{T} of more than 40 GeV. The jet cuts also have some reduction efficiency on the non-signal $t\bar{t}$ decay channels (di-leptonic and τ plus jets) and the single-top samples. The $E_{\mathrm{T}}^{\mathrm{miss}}$ cut is effective mainly for the QCD and all-hadronic $t\bar{t}$ decay. Even though the cut does not suppress the other background processes more than the signal, and thus is a loss from a statistical point of view, it is beneficial from the viewpoint of systematics as it selects a better-defined topology. Lastly, the HEC region cut obviously reduces the statistics but treats all samples nearly equally.

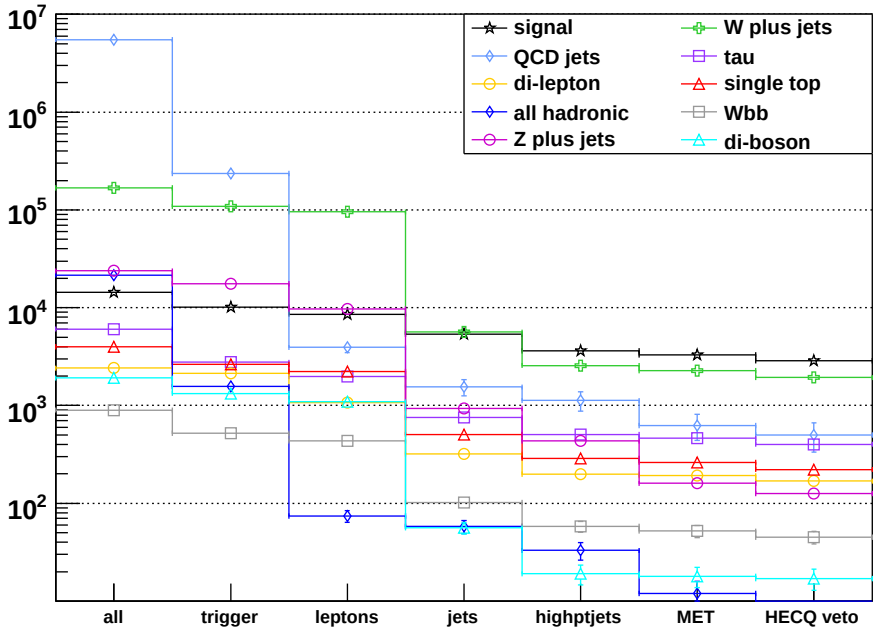

Figure 5.1: The number of events after applied cuts are shown for the different sets of signal and background samples, mixed in accordance with the SM cross-section for 145 pb^{-1}. The number of events in the first bin are the events after preselection. The events in the second bin either passed the muon or the electron trigger. The third bin shows events passing the lepton cut, with either an isolated muon, or an isolated electron. The fourth (fifth) bin shows the events passing the first (second) jet cut. Finally, the last two bins show the events passing the $E_{\mathrm{T}}^{\mathrm{miss}}$ and HEC region cut, respectively. As throughout this chapter, the signal events are lepton plus jet $t\bar{t}$ decays in the electron or muon channel, only. The histogram labelled tau contains the lepton plus jet and di-leptonic $t\bar{t}$ decays in the τ channel. The histogram labelled $QCDjets$ includes QCD processes in which the highest-energy jets have an E_{T} in the range of 140 to 1120 GeV. The error bars show the statistical error.

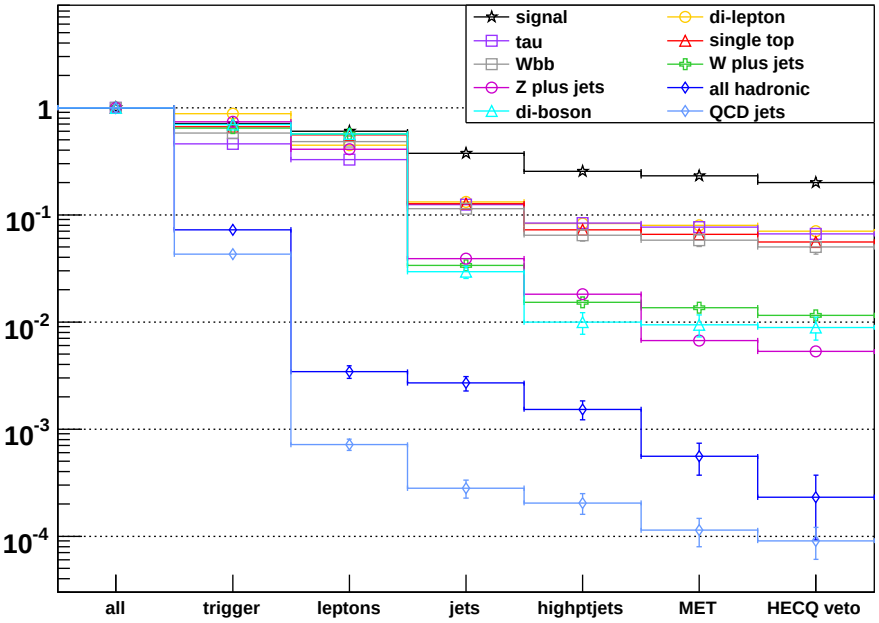

Figure 5.2: Same as Figure 5.1, but here each histogram is normalised to the first bin and thus is showing the selection efficiency of the different samples. The error bars show the binomial errors.

5.2.7 Event Selection for QCD Processes

The cuts used in the analysis presented here strongly reduce background from QCD processes - in particular, no event of the available fully simulated samples in which the E_{T} of the most energetic jets was below 140 GeV passed the event selection. The fully simulated samples hence could not be used to estimate the background coming from these processes. Instead, a small study on generator level was done.
Using ten million events generated with Pythia, the lepton fake rate can be estimated by comparing to lepton rates in full simulation: The selection cuts were emulated by an event filter on generator particle level. For the QCD processes in which the E_{T} of the most energetic jets was above 140 GeV, the efficiency of the truth filter was found to be compatible with the event selection performed on the fully simulated samples. For the processes with jets below 140 GeV, fewer events passed the lepton selection cut in the truth filter than for the selection on the fully simulated samples. It was found to be caused by the fact that the truth filter only selected real leptons, i.e. mostly non-prompt leptons from the decays of heavy-flavour quarks, whereas in the case of the selection on fully simulated samples, also leptons faked by jets were selected. From this finding it was possible to get an estimate of the fake rate:
The heavy-flavour decays are symmetrical enough (decay into muons vs electrons), to allow to perform the truth study only for one flavour, i.e. electrons and extrapolate to the case of the muons. Even though, for the fully simulated sample with jets with an E_{T} in the

range of 70 to 140 GeV, no event passed all selection cuts, enough events passed the lepton cut only. The difference between the number of events that passed the lepton selection in the fully simulated sample and the number of events that passed the lepton selection in the truth filter was taken as an estimate of the fake rate. The events passing the truth lepton filter were events with real leptons and in order to be comparable with the real leptons reconstructed in the detector and passing the selection on the full simulation, were scaled by the reconstruction efficiency of 0.67(0.88) [119] for electrons (muons). This resulted in an estimate of the fake rate of 4.5(5.3) 10^{-5} for electrons (muons). The numbers are comparable to the ones expected in [123] and more detailed studies, e.g. [119, 124].
The selection on generator level was now modified such that no lepton, but instead an additional jet was required. The number of events passing this selection was scaled by the respective fake rate, reducing the time for generation of Pythia events by a factor of 4.5(5.3) 10^5. Here the assumption is, that the $E_{\mathrm{T}}^{\mathrm{miss}}$ cut is independent of the lepton cut. This allowed for an estimate of how many events from QCD processes would pass the event selection for an integrated luminosity of 145 pb^{-1}:
The event selection used in this analysis requires six objects with a total p_{T} of 180 GeV. Hence it is expected that the most important background contributions come from processes with a momentum transfer in the hard process of above 90 GeV per parton. The first QCD sample to contribute is expected to be the one with jets with an E_{T} in the range of 70 to 140 GeV.
No real leptons passed the filter in the sample with jets in the range of E_{T} 35 to 70 GeV. Also, the number of events with fake leptons was small 0.03(0.04) events were expected for the electrons(muons). This sample and samples with even lower momentum transfer hence were not considered as relevant background. For sample with the highest-energy jets with an E_{T} in the range of 70 to 140 GeV, 630(827) real and 70(83) fake electrons (muons) are expected. For the samples with the highest-energy jets with an E_{T} in the range of 140 to 1120 GeV, the events that passed the selection of the fully simulated samples were scaled to the needed integrated luminosity. For these samples, no fake leptons are expected. These samples contribute to the background with 251(320) events from electrons(muons). As the exact cut flow is only known for these samples, in Figure 5.1 and 5.2 only they are included.
In order to correctly mix these events into the invariant mass spectrum, the lepton cut was replaced by requiring an additional jet also for the fully simulated sample with the highest-energy jets in the range of E_{T} 140 to 280 GeV. This way enough events passed the selection cuts and the resulting histogram was fitted with a Chebychev polynomial. The so obtained shape of the QCD background then was used to draw the wanted number of QCD background events with the correct shape. They then were added to the invariant mass spectrum.

5.3 Top Quark Reconstruction

5.3.1 Method of Top Quark Reconstruction

The (hadronic) top mass is reconstructed as follows: Jet triplets are built from all permutations of the jets passing the selection cuts. The jet triplet for each permutation is built by the four-vector sum of the three jets. The permutation which results in the triplet with the highest value of p_{T} is taken as the top quark candidate. On signal generator level, this

method chooses the correct combination in about 50% of the cases. The next probable case is the combination of the jets stemming from the W boson with the b jet from the leptonically decaying top quark. Considering jet mis-reconstruction and jet multiplicity, the topology is more complex and the probability of choosing the right combination of jets decreases further. In the events passing the selection cuts, there are on average five jets and hence ten combinations. For this case the probability of choosing the right combination has been estimated to be in the order of 25% in [127] and thus remains considerably better than random. However, a significant combinatorial background which also carries some top quark information has to be expected.
The invariant mass spectrum of the selected jet triplets is cleaned by the following purification cut: Of the three possible permutations of selecting two jets out of the jets in the triplet, at least one jet pair is required to have an invariant mass in the range of $M_W^{PDG} \pm 20$ GeV.
An estimate of the top quark mass is extracted from the invariant mass spectrum by using a χ^2 fitting procedure. The fit is parametrised by the convolution of a Gaussian and a 4^{th} order Chebychev polynomial. In Figure 5.3 (5.4) the invariant mass spectrum of the top quark candidates is shown for the electron (muon) channel, respectively. The Gaussian part of the fit is shown in red, the Chebychev in green. The invariant mass distribution is split into the combinatorial background (signal only) shown in magenta, the top mass dependent physics background in cyan, the background from QCD processes in gray and the remaining physics background in blue. All background contributions are summed up, building the green histogram.
It is clearly visible that the fit shows some weakness in describing the background, which particularly in the muon channel is peaking close to the signal. In samples with higher integrated luminosity it is possible to improve the situation by allowing higher orders of the Chebychev polynomial. In the case presented here, it is not advisable as the higher-order Chebychev polynomial then starts to follow the statistical fluctuations in the tail of the distribution.
In order to estimate the goodness of the fit, a histogram containing the events where the reconstructed top quark candidate was matched to the generated top quark with $\Delta R < 0.2$ is shown in red. It was fitted by a simple Gaussian, shown in blue. The statistics boxes in Figures 5.3, 5.4 show the resulting fit parameters.
Looking at the difference especially of the mean value of the two Gaussians, it is evident that the background peaking just below the signal leads to a residual shift to lower values. The systematic effects of the fitting procedure will be further discussed in Section 5.7.3.

5.4 W Reconstruction

For reconstructing the W boson, several methods have been proposed and studied. The W signal has an additional combinatorial background due to the three-fold ambiguity in choosing the di-jet pair out of the jet triplet selected as top quark candidate.
One possibility is to choose the di-jet pair which in turn result in the object with the highest p_{T}. However, this method was found to be overestimating the W boson mass by several GeV[4].

[4]For the standard selection cuts used her, the resulting W mass was 84.32 ± 1.80 GeV and even the Gaussian fit to the distribution of the matched W boson candidates had a mean of 82.79 ± 0.68 GeV.

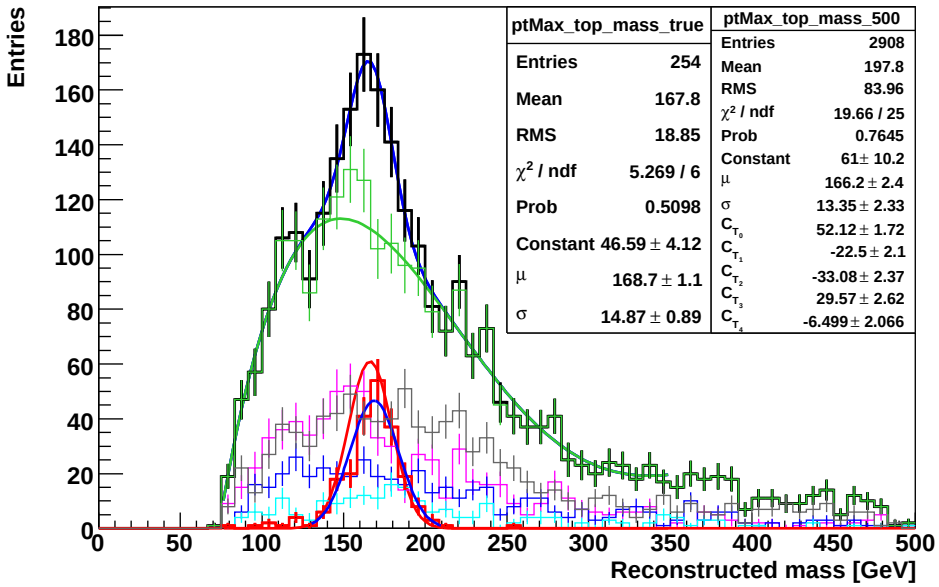

Figure 5.3: Invariant mass spectrum of jet triplet maximising p_{T} for local hadron calibrated Kt4 jets in the electron channel. The data after the purification cut (see text) is shown in black, the total background in green. The combinatorial background is shown in magenta, the top mass dependent physics background in cyan, the background from QCD processes in gray and the remaining background in blue. The red histogram shows the events where the four-vector of the reconstructed top quark was matched to the generated top quark with $\Delta R < 0.2$. The fit function is shown in blue, the green curve shows the Chebychev and the red curve Gaussian part. The respective fit parameters for the fit to the histogram of the invariant mass spectrum are shown in the right statistics box. Here μ (σ) is the mean (width) of the Gaussian and $\mathrm{C}_{\mathrm{T}_{0-4}}$ are the parameters of the Chebychev part. The left statistics box shows the parameters of a Gaussian fit (blue curve) to the red histogram containing the matched events.

The method chosen here is the following: The three jets constituting the triplet are first boosted back to the centre-of-mass frame of the top quark candidate. Then out of the three permutations of selecting two jets out of jet triplet, the one di-jet combination in which the two jets have the minimal distance in ΔR is chosen as W boson candidate[5]. This method showed better results than the one where ΔR between the jets is minimised in the lab system.
Again, an estimate for the W mass is obtained by fitting the invariant mass spectrum with a function parametrised by the convolution of a Gaussian and a 4^{th} order Chebychev polynomial. In Figure 5.5 (5.6) the invariant mass spectrum of the W boson candidates is shown for the electron (muon) channel, respectively. The combinatorial background is shown in magenta, the background from QCD processes in gray and the remaining physics

[5] A variation of this method chooses the jet with the highest momentum in the CMS of the top quark candidate as b jet and uses the remaining two to build the W boson candidate. It selects nearly the same topology and also shows nearly the same performance but is less intuitive and thus not applied here.

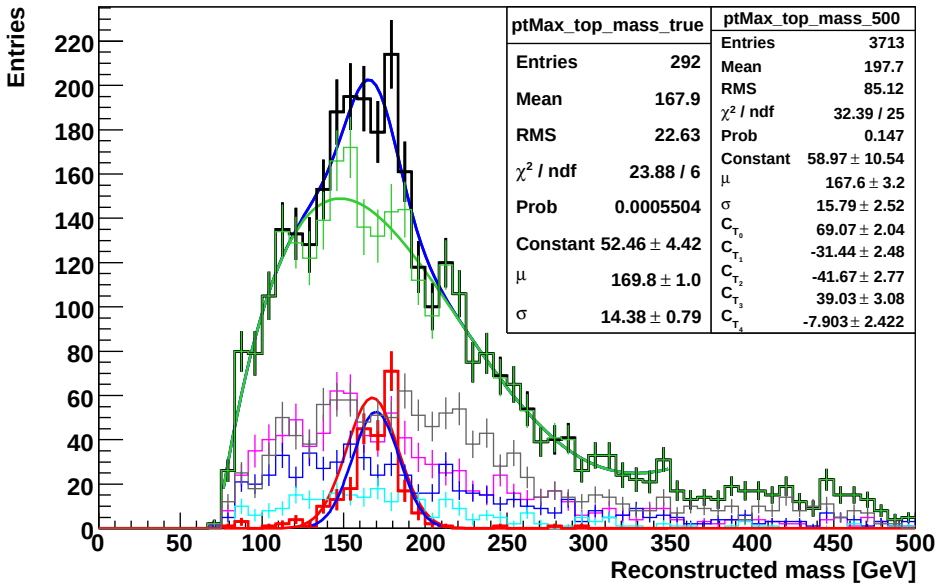

Figure 5.4: Invariant mass spectrum of jet triplet maximising p_{T} for local hadron calibrated Kt4 jets in the muon channel. The data after the purification cut (see text) is shown in black, the total background in green. The combinatorial background is shown in magenta, the top mass dependent physics background in cyan, the background from QCD processes in gray and the remaining background in blue. The red histogram shows the events where the four-vector of the reconstructed top quark was matched to the generated top quark with $\Delta R < 0.2$. The fit function is shown in blue, the green curve shows the Chebychev and the red curve Gaussian part. The respective fit parameters for the fit to the histogram of the invariant mass spectrum are shown in the right statistics box. Here μ (σ) is the mean (width) of the Gaussian and $\mathrm{C}_{\mathrm{T}_{0-4}}$ are the parameters of the Chebychev part. The left statistics box shows the parameters of a Gaussian fit (blue curve) to the red histogram containing the matched events.

background in blue. All background contributions are summed up in the green histogram. A histogram containing the events where the jets constituting the reconstructed W boson candidate were matched to the generated light quarks from the W decay with $\Delta R < 0.2$ is shown in red, which again was fitted by a simple Gaussian, shown in blue. The statistics boxes in Figures 5.5, 5.6 show the resulting fit parameters. In the electron channel a binning effect resulting in a 'chimney' of the combinatorial background close to the signal peak somehow degrades the fit result and its probability. A similar effect is also present in the case of the muon channel but outside the signal region.

5.5 Iterative In-Situ Calibration

The iterative in-situ calibration method as described in Section 4.3.1 was then applied and the jets constituting the W boson candidate were filled into 10 histograms, according

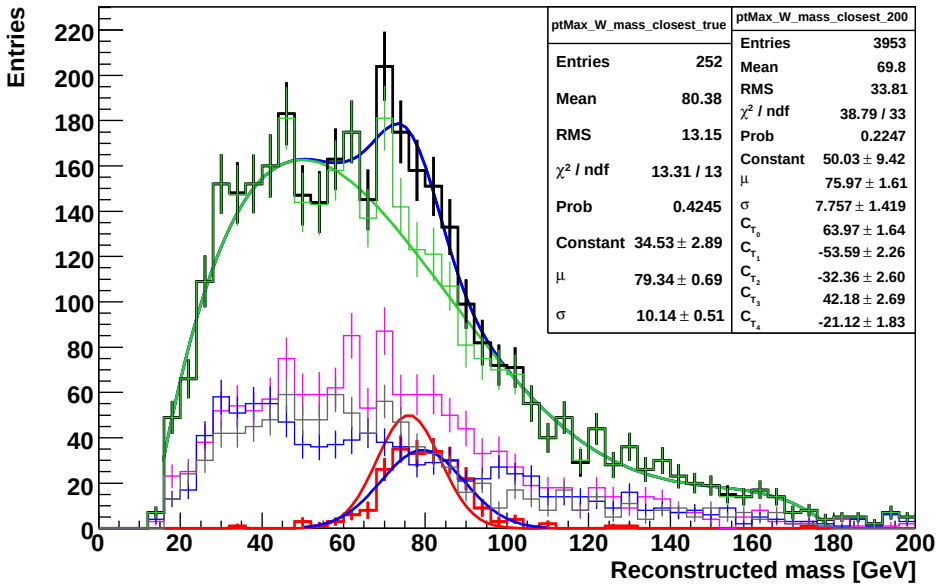

Figure 5.5: Invariant mass spectrum of the two jets of the selected jet triplet, which after a boost to the top quark candidates CMS are closest in ΔR for local hadron calibrated Kt4 jets in the electron channel. The data is shown in black, the total background in green. The combinatorial background is shown in magenta, the background from QCD processes in gray and the remaining physics background in blue. The red histogram shows the events where the reconstructed jets were matched to the generated light quarks with $\Delta R < 0.2$. The fit function is shown in blue, the green curve shows its Chebychev and the red curve its Gaussian part. The respective fit parameters for the fit to the histogram of the invariant mass spectrum are shown in the right statistics box. Here μ (σ) is the mean (width) of the Gaussian and $C_{T_{0-4}}$ are the parameters of the Chebychev part. The left statistics box shows the parameters of a Gaussian fit (blue curve) to the red histogram containing the matched events.

to their energy. The histograms were chosen such that they covered the range from 50 to 400 GeV in logarithmically spaced bins. For each of the histograms, the aforementioned fit was used and the resulting mean value of the Gaussian part was filled into a calibration histogram, which was used to apply an energy dependent calibration of all jets in the subsequent step. After ten iterations the calibration function was extracted as product of all prevenient iteration steps. Figure 5.7 shows this calibration function (red), the first iteration (black) and the last iteration (blue). As expected, the final calibration function closely follows the first iteration, but due to higher order effects is not the same. The flatness of the 9^{th} iteration shows the convergence of the procedure.
With more statistics it will be possible to use this method not only binned in energy, but e.g. also in pseudo-rapidity.

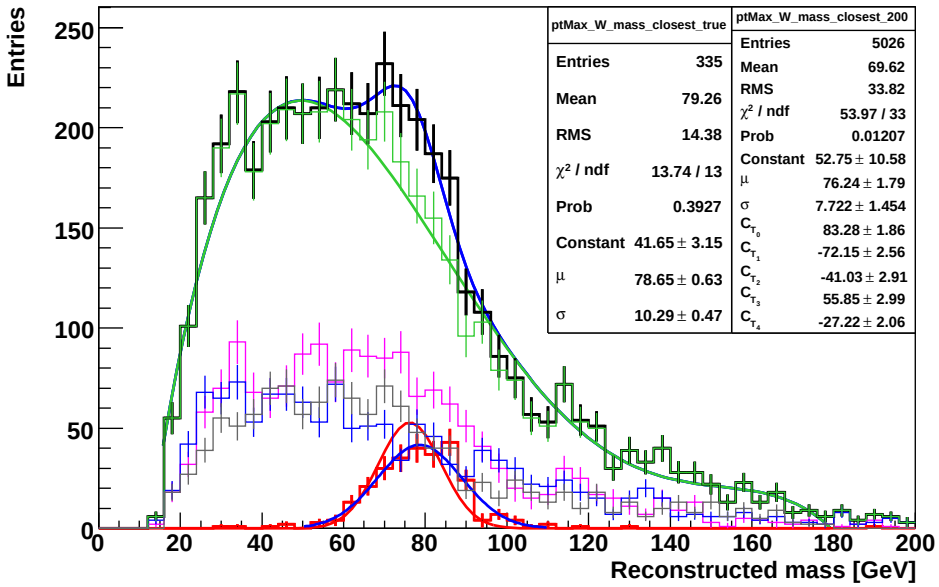

Figure 5.6: Invariant mass spectrum of the two jets of the selected jet triplet, which after a boost to the top quark candidates CMS are closest in ΔR for local hadron calibrated Kt4 jets in the muon channel. The data is shown in black, the total background in green. The combinatorial background is shown in magenta, and the physics background in blue. The red histogram shows the events where the reconstructed jets were matched to the generated light quarks with $\Delta R < 0.2$. The fit function is shown in blue, the green curve shows its Chebychev and the red curve its Gaussian part. The respective fit parameters for the fit to the histogram of the invariant mass spectrum are shown in the right statistics box. Here μ (σ) is the mean (width) of the Gaussian part and $C_{T_{0-4}}$ are the parameters of the Chebychev. The left statistics box shows the parameters of a Gaussian fit (blue curve) to the red histogram containing the matched events.

5.5.1 Top Quark and W Boson Mass Spectrum after In-Situ Calibration

The calibration function obtained in the previous section was then applied to calibrate all the jets of the analysed sample and again candidates for the top quark and the W boson were reconstructed as described before.
The resulting invariant mass spectra are shown in Figures 5.8, 5.9, 5.10, 5.11. In the case of the W reconstruction the extracted estimate for the mass is close to the PDG value, as expected. In the case of the top quark, the extracted mean value was shifted from 166.23 ± 2.41 to 167.22 ± 2.38 GeV (167.62 ± 3.22 to 167.53 ± 3.11 GeV) for the electron (muon) channel. The width of the Gaussian was shifted from 13.35 ± 2.33 to 13.39 ± 2.31 GeV (15.79 ± 2.52 to 17.63 ± 3.01 GeV) for the electron (muon) channel. This is still within the statistical errors of the fit, which shows that the initial calibration was good with respect to the precision achievable at the statistics used here by the in-situ calibration method. Especially in the case of a initial jet energy scale mis-calibration, the in-situ method shows a much bigger effect (see Section 5.7.1). In the case of a deliberate

rescaling of the jet energy, the in-situ method allows to recover the jet energy scale to a good extent, as will be shown in the following.

5.6 Purity and Efficiency of the Reconstruction Method

In order to get an estimate of the efficiency and purity with which the generated top quarks are actually selected and reconstructed in this analysis, the following definitions are used: The *efficiency* is defined as the number of events in which the reconstructed top quark candidate was matched to the generated top quark with $\Delta R < 0.2$ divided by the number of tops generated for the respective decay channel and the used integrated luminosity. For the electron (muon) channel the so-defined efficiency is 2.9% (3.4%).
The *purity* of the method is defined as the fraction of events in which the reconstructed top quark candidate was matched to the generated top quark with $\Delta R < 0.2$ over the number of events selected in a window of $\pm 2\sigma$ around the reconstructed mass value, i.e. the mean value of the Gaussian part of the fit to the invariant mass spectrum. For the electron (muon) channel the so-defined purity is 27.6% (22.1%).
An estimate for the yield or the discriminating power of the used fit function can be given by looking at the fraction of events under the Gaussian part of the fit within a window of $\pm 2\sigma$ around its mean value over the number of events in which the reconstructed top quark candidate was matched to the generated top quark with $\Delta R < 0.2$. This value ideally is 1, a value larger than 1 indicates an overestimation of the Gaussian part, a number smaller then 1 an underestimation, respectively. For the electron (muon) channel the fraction is 92.1% (91.6%).

5.7 Systematics

In order to estimate the systematic effects influencing the reconstruction method, several parameters of the method were varied. Table 5.3 shows the variations of the reconstructed top quark and W boson mass with the different variations on the jet energy scale, the used jet algorithm and the jet selection cuts. The different variations and their impact on the reconstructed mass will be discussed in the following.

5.7.1 Jet Energy Scale and Calibration

As the top quark candidates in the analysis performed here are reconstructed from three jets, a possible jet energy scale mis-calibration could systematically influence the result. In order to estimate the effect of a mis-calibrated jet energy scale, the analysis was performed with a rescaled jet energy: All jets were scaled up (down) to 105 (95)% and the analysis described in the previous section was performed again. Figure 5.12 shows as an example the effect of a rescaling of the jet energy on the reconstructed top mass in the electron channel. Figure 5.13 shows the effect on the reconstructed mass of the W boson, if the jets were scaled down to 95%. It is clearly visible that the mean of the fit follows the difference in jet energy scale, for both the top quark and the W boson reconstruction.
Due to the difference in composition and especially because of the possible semi-leptonic

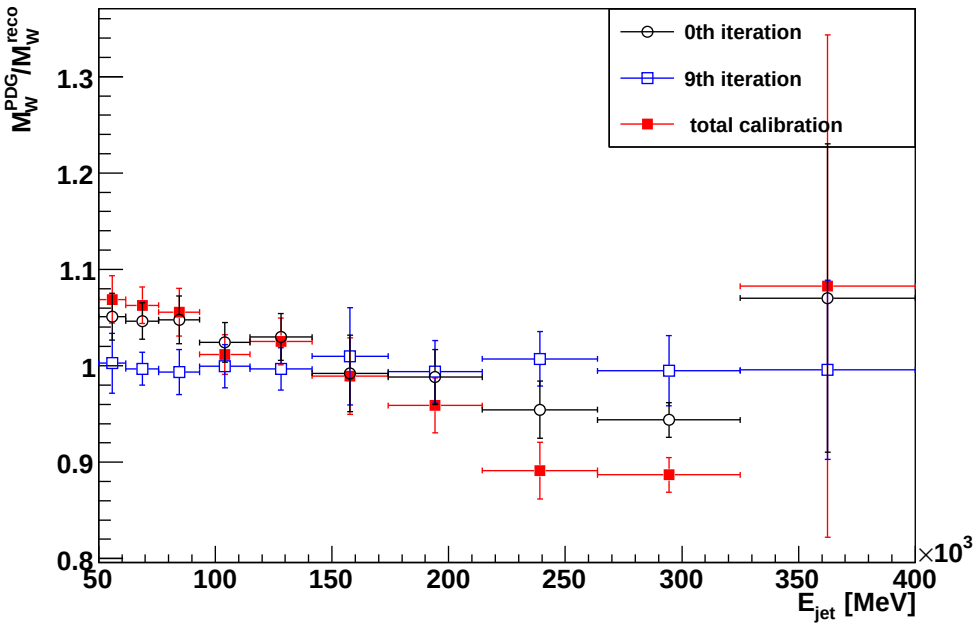

Figure 5.7: In-situ calibration function after 9 iterations shown in red, the first iteration is shown in black, the last is shown in blue. The error bars show the relative errors of the fit in the different bins of the first iteration.

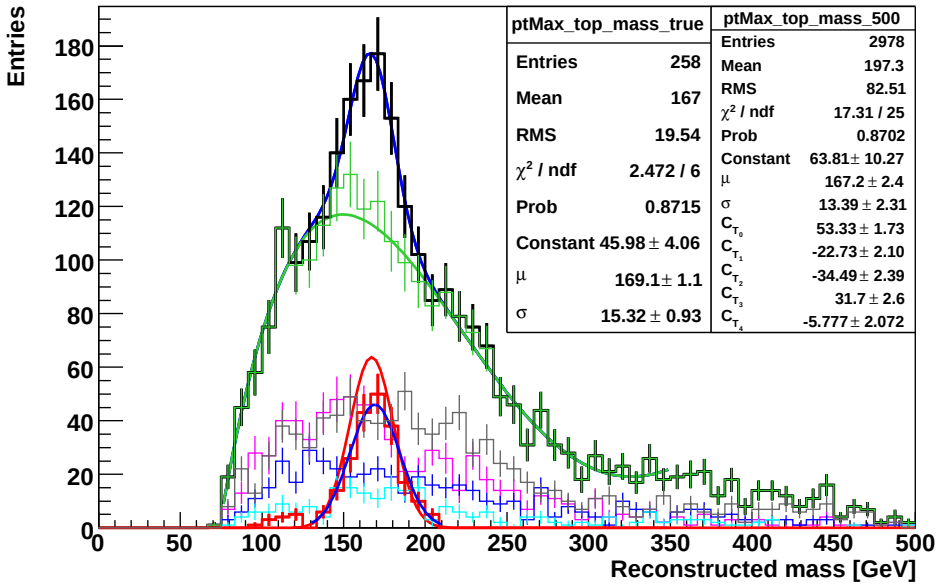

Figure 5.8: Invariant mass spectrum of the top quark candidates for the electron channel as in Figure 5.3 but after application of the in-situ calibration shown in Figure 5.7.

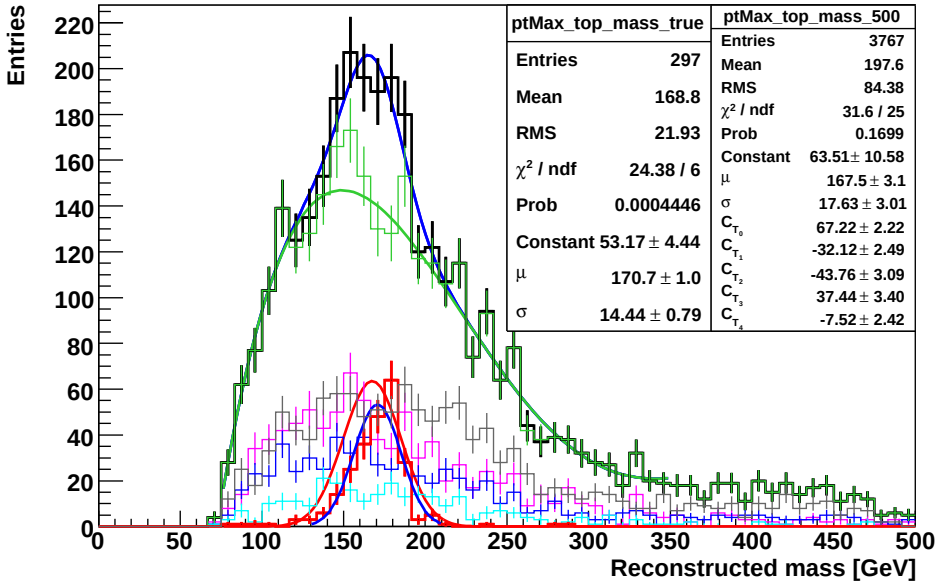

Figure 5.9: Invariant mass spectrum of the top quark candidates for the muon channel as in Figure 5.4 but after application of the in-situ calibration shown in Figure 5.7.

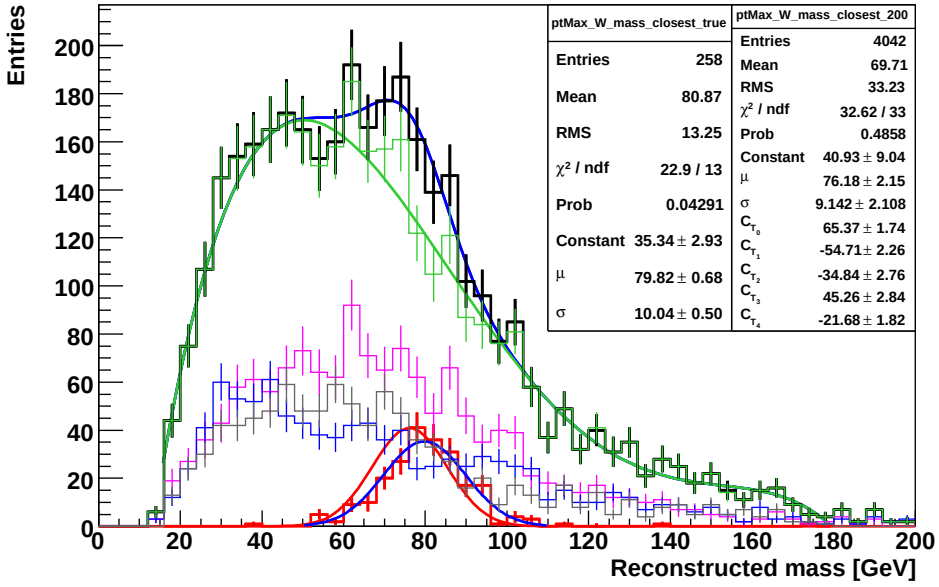

Figure 5.10: Invariant mass spectrum of the W candidates for the electron channel as in Figure 5.5 but after application of the in-situ calibration shown in Figure 5.7.

decays, the b jet energy scale usually differs from the light jet energy scale. For this reason the same rescaling exercise was done for the b jets alone. Here not all, but only the jets, which were matched to a b quark where rescaled. The effect of this variation is visible for the top quark reconstruction, too. However, as expected, the W boson reconstruction does not follow the variation of the b jet energy scale as much.
The application of the in-situ calibration successfully recovers the effect of the light jet energy rescaling for the reconstructed top quark (cf. Figure 5.14). However, the variations of the b jet energy scale are not recovered to the same extent. This is expected, as the in-situ calibration is using the jets of the W boson candidate as reference and hence, with the exception of mis-reconstruction, sets the jet energy scale for the light jets only. For the b jets it can only account for a residual mis-calibration, which is not heavy-flavour jet specific.
The jet energy scale in the case of the default cuts is shown in Figure 5.16. The fraction of energy of the reconstructed jet versus the generated quark stemming from the W boson decay is shown for two scenarios. First, the quarks were matched with $\Delta R < 0.2$ to the best possible matching jet in the event (green). This should give an estimate of the level of jet calibration in the specific topology selected by the event selection. Then the match was done with respect to the very jets selected by the reconstruction algorithm to build the W boson candidates (black). One expects an additional bias in this case, as the phase space is further reduced due to the jet selection in choosing the W boson candidates.
When the iterative in-situ calibration method was introduced in Section 4.3.1, it was mentioned that this method does not really measure the mere jet energy scale, but rather an *effective jet energy scale*, which comprises all other biases introduced by the whole chain of the analysis method, as it is aiming at a correction of the value of the extracted W boson mass. This includes biases by the selection and reconstruction decisions, as well as the fitting procedure.
Looking at Figure 5.17, this can clearly be seen. Upon application of the in-situ calibration function, the jet energy scale is significantly changed and now tends to follow the shape of the calibration function itself (cf. Figure 5.7).

5.7.2 Jet p_{T} Cut in Event Selection

As explained above, in the event selection, two cuts on the p_{T} of jets are applied. These cuts select a specific topology and might also systematically bias the reconstruction. In order to estimate this effect, the 2^{nd} jet p_{T} cut in the standard analysis set to 40 GeV was relaxed or hardened to 30 and 50 GeV, respectively, and the analysis was performed again. As this cut has a strong impact on the topology of the selected events, the background shape also varies visibly. In Figures 5.15 this is shown as example for the top mass reconstruction in the muon channel. Table 5.3 again summarises the effect on the reconstructed top quark and W boson mass if the 2^{nd} selection cut on the jet p_{T} is varied.
The variations of the jet p_{T} cut were found to change the topology and hence the shape of the background to an extent that the fits to the invariant mass spectrum of the reconstructed W candidates used in the in-situ calibration show large errors. As this is directly influencing the extraction of the in-situ calibration function, it is also spoiling the effect of the in-situ calibration and diminishes the recovery potential of the jet energy scale by this method.
This variation of the cut is thus not taken as a systematic error, but as a variation of the

analysis method, which would have to be studied separately. The dependence of the jet p_{T} cuts due jet energy scale effects is taken into account by the variation of the jet energy scale.

5.7.3 Fit and Combinatorics

As mentioned above and as evident from some of the invariant mass spectra of the reconstructed top quark candidate shown here, the parametrisation of the fitting function used here sometimes unsatisfactory masters the description of the background. The peaking background is often not correctly fitted with the here used Chebychev polynomial.
Especially the peaking character of the background just below the region of the signal peak, at slightly lower value, influences the fitting. Particularly the Gaussian part of the fitting function is shifted to lower values with regard to the matched four-vectors, because it tends to absorb a significant part of the background. For samples with higher integrated luminosity, a Chebychev polynomial of 7^{th} order significantly improves the situation. However, this is not applicable to the statistics available here, as the Chebychev polynomial then follows the statistical fluctuations in the tail of the invariant mass distributions.
In order to get an estimate of the bias introduced by this fitting procedure, some ensemble tests were done and the order of the Chebychev polynomial was varied. Comparing the mean of the Gaussian part of the fit to the whole invariant mass spectrum with the one of the fit of the matched four-vectors gives some estimate about this bias. The difference between the mean values is about 3.2 GeV and varies between 0.5 and 5.9 GeV.
In order to disentangle this effect from the level of calibration of the reconstructed jets, a small study was carried out using jets from generator particles on three samples with different generated top masses (160, 170, 180 GeV). Here, the difference between the mean of the Gaussian fit to the matched four-vectors and the mean of the Gaussian part of the whole invariant mass spectrum had a mean of 1.47 GeV and varied between 0.2 and 2.8 GeV.

5.7.4 Background

In the predicted rate of the physics background there is a large uncertainty, especially as the LHC will be operating at new kinematic regions for which the cross-sections are not yet measured and for which the Monte Carlo generators hence are not yet tuned. Ultimately the background rates can be obtained from data. For example, the ratio (Z plus jets)/(W plus jets) has a much-reduced theoretical uncertainty and is better described by Monte Carlo as the absolute rate of W plus jets. One will be able to measure the Z plus jets rate in the data using the leptonic decay of the Z and hence it will be possible to determine the W plus jets rate. In order to obtain a good estimate of the QCD background ratio, it will have to be extracted from data for the aforementioned reasons. Not only is the QCD difficult to predict in the new kinematic region of LHC, but also the computing power needed is tremendous due to the high cross-section of the QCD processes.
In order to estimate the systematic effect of an over- or underestimation of the background rate on the results of this analysis, the background contribution was varied up and down. In one set the background was scaled up by a factor 150% and in another set, the background was scaled down by a factor 50%. This was done independently once for the background

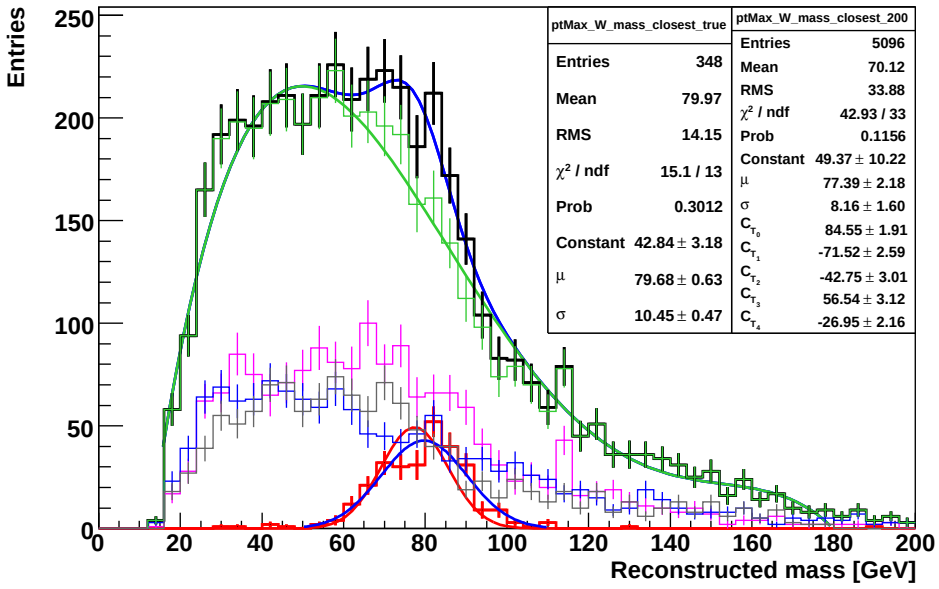

Figure 5.11: Invariant mass spectrum of the W candidates for the muon channel as in Figure 5.6 but after application of the in-situ calibration shown in Figure 5.7.

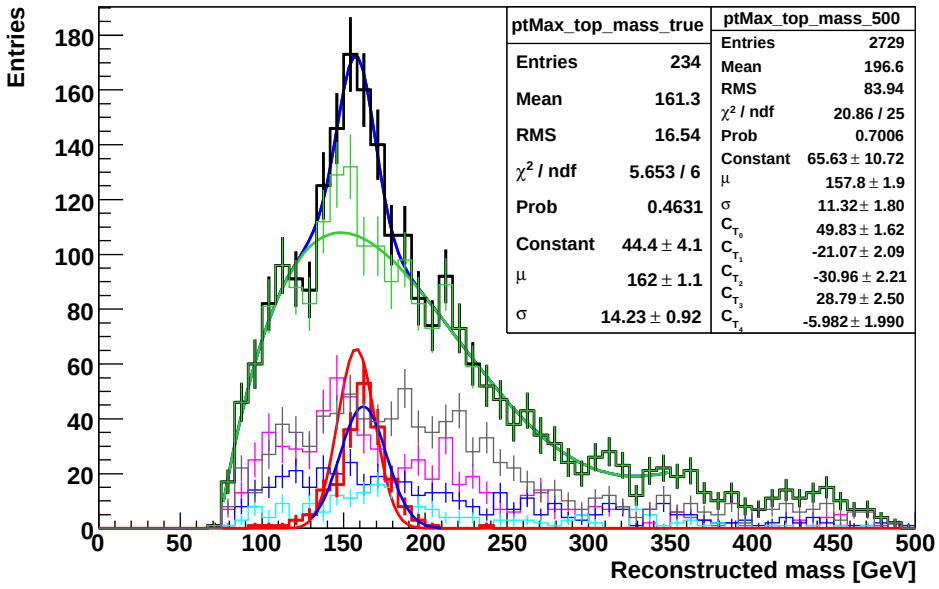

Figure 5.12: Invariant mass spectrum of the top quark candidates for the electron channel as in Figure 5.3 but after rescaling the jet energies with 95%.

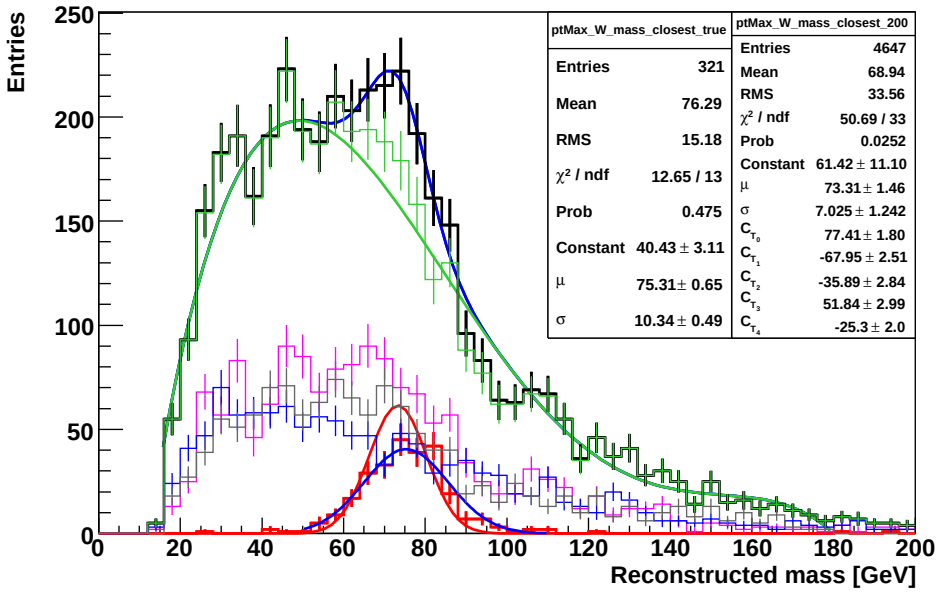

Figure 5.13: Invariant mass spectrum of the W candidates for the muon channel as in Figure 5.6 but after rescaling the jet energies with 95%.

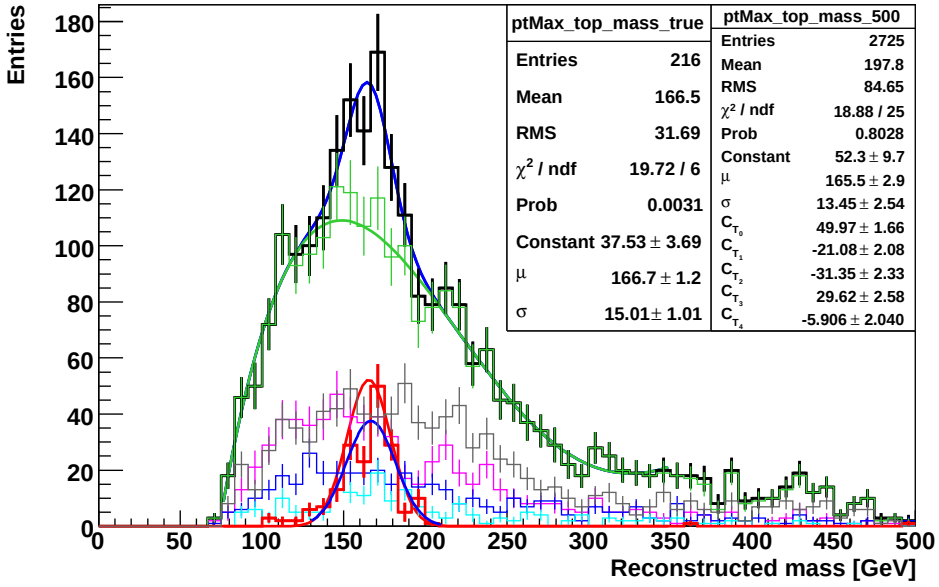

Figure 5.14: Invariant mass spectrum of the top quark candidates for the electron channel as in Figure 5.12 after rescaling the jet energy with 95% and application of the in-situ calibration shown in Figure 5.7.

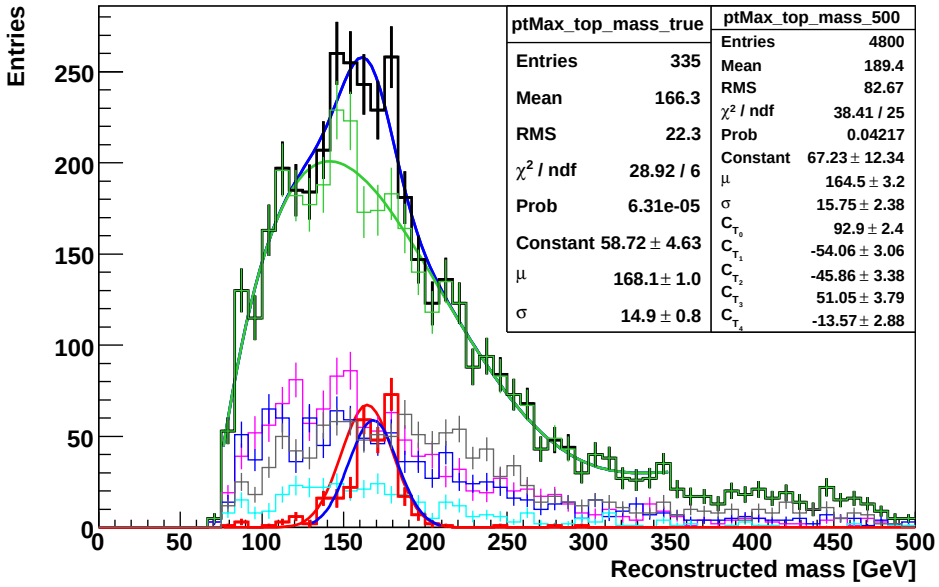

Figure 5.15: Invariant mass spectrum of the top quark candidates for the muon channel as in Figure 5.4 but here the 2^{nd} p_{T} cut used in the events election for the jets was lowered to 30 GeV.

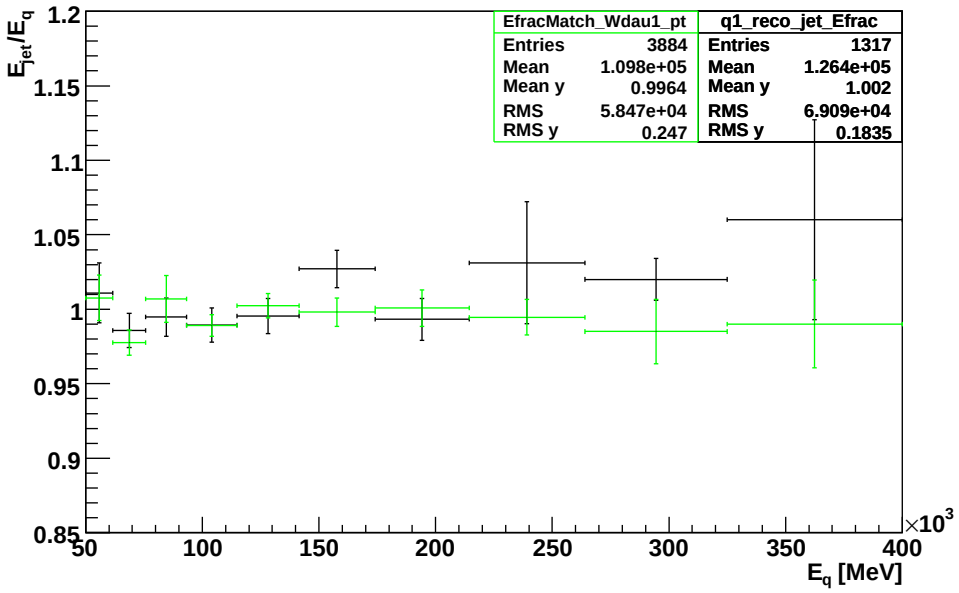

Figure 5.16: Fraction of energy of the reconstructed jet vs the generated quark steming from the W boson decay. The quarks were matched with $\Delta R < 0.2$ to the jets used as W boson candidate (black) or the best possible matching jet (green).

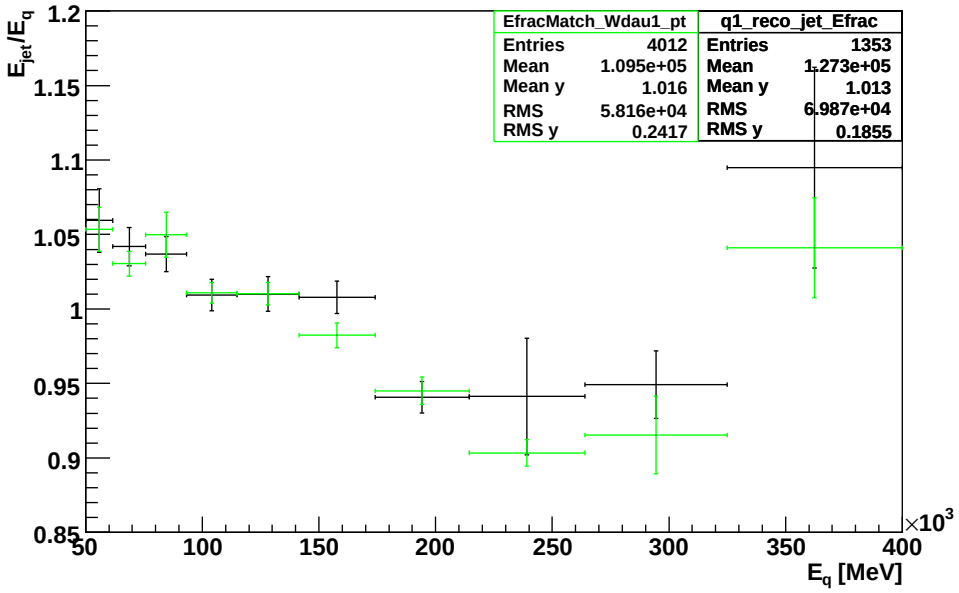

Figure 5.17: Fraction of energy of the reconstructed jet vs the generated quark steming from the W boson decay, same as in Figure 5.16, but after application of the in-situ calibration. This plot nicely demonstrates, that the in-situ calibration results in an effective JES rather than a measurement of the real JES.

from QCD processes and once for all other physics backgrounds. The variations of the reconstructed mass values are summarised in Table 5.2. As the main background in the dataset used in this analysis is combinatorial, the effect of a rescaled physics background is not very large. With higher statistics, the combinatorial background is expected to decrease and the physics background will become more important.

5.7.5 Summary of Systematic Effects

After the different parameters of the analysis have been varied, the overall systematic error has to be determined:
Both the deliberate rescaling of the light and the b jet energy scale results in a systematic variation of the reconstructed top mass value. Rescaling the light jet energy scale by $\pm 5\%$ results in a variation of the top mass value of ± 8.47 (± 9.05) GeV in the electron (muon) channel.
A variation of the b jet energy scale as expected has a smaller effect. The reconstructed top mass varies by ± 2.58 (± 2.99) GeV in the electron (muon) channel.

$$\sigma_{systJES}^{electron} = \pm(8.47 \oplus 2.58) = \pm 8.85 \text{ GeV}$$

$$\sigma_{systJES}^{muon} = \pm(9.05 \oplus 2.99) = \pm 9.53 \text{ GeV}$$

As shown in Table 5.5, the systematic error on the jet energy scale is decreased significantly by the in-situ calibration method. This was expected and is particularly prominent in the

	Gaussian fit parameters [GeV]			
	before in-situ calibration		after in-situ calibration	
	mean (μ)	width (σ)	mean (μ)	width (σ)
	local hadron calibrated Kt4 jets			
m_t electron	166.23 ± 2.41	13.35 ± 2.33	167.22 ± 2.38	13.39 ± 2.31
m_t muon	167.62 ± 3.22	15.79 ± 2.52	167.53 ± 3.11	17.63 ± 3.01
m_W electron	75.97 ± 1.61	7.76 ± 1.42	76.18 ± 2.15	9.14 ± 2.11
m_W muon	76.24 ± 1.79	7.72 ± 1.45	77.39 ± 2.18	8.16 ± 1.60
	QCD background scaled up by 150%			
m_t electron	166.15 ± 2.58	13.73 ± 2.36	167.09 ± 2.53	13.79 ± 2.33
m_t muon	167.50 ± 3.40	16.33 ± 2.74	167.59 ± 3.36	18.40 ± 3.42
	QCD background scaled down by 50%			
m_t electron	166.28 ± 2.40	12.90 ± 2.40	167.36 ± 2.36	12.93 ± 2.42
m_t muon	167.89 ± 3.20	15.35 ± 2.57	167.58 ± 3.10	17.06 ± 2.96
	non-QCD physics background scaled up by 150%			
m_t electron	166.30 ± 2.44	12.99 ± 2.39	167.26 ± 2.46	13.11 ± 2.46
m_t muon	167.11 ± 3.23	15.45 ± 2.39	167.27 ± 3.10	17.16 ± 2.88
	non-QCD physics background scaled down by 50%			
m_t electron	166.12 ± 2.45	13.70 ± 2.32	167.21 ± 2.38	13.66 ± 2.26
m_t muon	168.11 ± 3.34	16.20 ± 2.78	167.78 ± 3.26	18.21 ± 3.33
	all physics background scaled up by 150%			
m_t electron	166.23 ± 2.63	13.41 ± 2.43	167.11 ± 2.61	13.58 ± 2.48
m_t muon	166.96 ± 3.45	15.94 ± 2.55	167.32 ± 3.34	17.82 ± 3.20
	all physics background scaled down by 50%			
m_t electron	166.18 ± 2.45	13.30 ± 2.51	167.31 ± 2.39	13.26 ± 2.40
m_t muon	168.36 ± 3.32	15.69 ± 2.81	167.85 ± 3.27	17.55 ± 3.25

Table 5.2: Fit results of top quark mass measurement in different variations of the background contributions. Before (left column) and after (right column) the application of the in-situ calibration.

case of variations of the light jet energy scale. However, due to the non-linear correlations in the in-situ calibration method, the systematic error of the light jet energy scale now is no longer symmetric, but rather shows a shift in one direction of -1.56 (-0.78) GeV in the electron (muon) channel. This indicates that the method is over-compensating the induced shifts by rescaling the jet energy scale.
The b jet energy scale variations are not causing an asymmetric bias, as the in-situ calibration method by construction aims at a calibration of the light jets only. Merely non heavy-flavour-specific mis-calibrations of the b jets could be recovered by this method. The remaining systematic error of the b jet energy scale is ±1.83 (±3.95) GeV in the electron (muon) channel.
The bias of the fitting procedure has been estimated to cause a positive shift of +3.2 ± 2.7 GeV. As this shift is known to 1 σ only, it is not applied as correction, but rather treated as an additional systematic, positive error of 3 GeV.
The independent variations of the QCD and the non-QCD physics background as well as a simultaneous variation of both contributions shows only little influence on the reconstructed top mass value. It thus is not considered in the computation of the overall

	Gaussian fit parameters [GeV]			
	before in-situ calibration		after in-situ calibration	
	mean (μ)	width (σ)	mean (μ)	width (σ)
	local hadron calibrated Kt4 jets			
	mean (μ)	width (σ)	mean (μ)	width (σ)
	local hadron calibrated Kt4 jets			
m_t electron	166.23 ± 2.41	13.35 ± 2.33	167.22 ± 2.38	13.39 ± 2.31
m_t muon	167.62 ± 3.22	15.79 ± 2.52	167.53 ± 3.11	17.63 ± 3.01
m_W electron	75.97 ± 1.61	7.76 ± 1.42	76.18 ± 2.15	9.14 ± 2.11
m_W muon	76.24 ± 1.79	7.72 ± 1.45	77.39 ± 2.18	8.16 ± 1.60
	local hadron calibrated AntiKt4 jets			
m_t electron	162.10 ± 2.22	13.83 ± 1.94	166.36 ± 2.44	16.16 ± 2.22
m_t muon	168.74 ± 3.38	14.61 ± 4.33	170.79 ± 3.29	15.62 ± 3.73
m_W electron	74.47 ± 1.75	7.42 ± 1.44	76.93 ± 1.47	6.39 ± 1.53
m_W muon	73.45 ± 1.90	8.12 ± 1.36	75.55 ± 1.92	7.96 ± 1.52
	rescaled jet energy 95%			
m_t electron	157.83 ± 1.91	11.32 ± 1.80	165.51 ± 2.85	13.45 ± 2.54
m_t muon	157.88 ± 2.68	13.82 ± 2.23	166.00 ± 3.56	17.21 ± 4.01
m_W electron	72.92 ± 1.56	8.10 ± 1.19	76.56 ± 1.62	7.65 ± 1.60
m_W muon	73.31 ± 1.46	7.02 ± 1.24	76.13 ± 2.44	8.12 ± 1.97
	rescaled jet energy 105%			
m_t electron	174.77 ± 2.39	11.85 ± 2.48	165.82 ± 2.37	14.07 ± 2.28
m_t muon	175.98 ± 3.60	18.06 ± 3.97	167.57 ± 3.46	16.93 ± 3.34
m_W electron	78.97 ± 2.09	8.47 ± 1.78	76.45 ± 1.87	7.76 ± 1.57
m_W muon	79.77 ± 2.20	8.44 ± 1.69	78.91 ± 2.20	5.96 ± 1.90
	rescaled b jet energy 95%			
m_t electron	162.93 ± 2.13	11.23 ± 2.15	164.36 ± 2.42	14.05 ± 2.13
m_t muon	165.43 ± 2.75	14.26 ± 2.26	165.03 ± 2.84	16.05 ± 2.77
m_W electron	75.60 ± 1.64	7.80 ± 1.45	76.59 ± 1.99	8.97 ± 1.96
m_W muon	75.68 ± 1.97	7.89 ± 1.54	77.41 ± 1.99	7.87 ± 1.47
	rescaled b jet energy 105%			
m_t electron	168.08 ± 2.43	13.92 ± 2.15	168.02 ± 2.51	14.17 ± 2.28
m_t muon	171.41 ± 3.54	15.73 ± 3.11	172.93 ± 3.30	15.93 ± 3.22
m_W electron	76.20 ± 1.57	7.64 ± 1.37	75.91 ± 2.06	8.48 ± 1.96
m_W muon	76.77 ± 1.94	7.72 ± 1.57	78.05 ± 2.49	7.40 ± 1.87
	2nd jet p_T cut at 30 GeV			
m_t electron	165.11 ± 2.30	12.30 ± 2.36	164.97 ± 2.34	13.51 ± 2.38
m_t muon	164.47 ± 3.17	15.75 ± 2.38	164.97 ± 3.72	17.45 ± 3.00
m_W electron	74.45 ± 1.84	6.94 ± 1.48	74.90 ± 2.19	6.94 ± 1.70
m_W muon	74.74 ± 1.79	7.99 ± 1.55	76.45 ± 2.42	7.85 ± 1.88
	2nd jet p_T cut at 50 GeV			
m_t electron	169.52 ± 2.73	13.53 ± 2.44	168.07 ± 2.55	12.51 ± 2.98
m_t muon	169.14 ± 3.38	16.93 ± 2.92	166.33 ± 3.64	17.86 ± 3.57
m_W electron	78.39 ± 1.94	8.09 ± 1.58	78.53 ± 2.52	8.72 ± 2.05
m_W muon	77.63 ± 2.12	7.42 ± 1.56	77.41 ± 1.65	6.05 ± 1.26

Table 5.3: Fit results of top quark W boson mass measurement in different variations of the jet energy and the jet selection cuts. Before (left column) and after (right column) the application of the in-situ calibration.

	Gaussian fit parameters [GeV]			
	before in-situ calibration		after in-situ calibration	
	mean (μ)	width (σ)	mean (μ)	width (σ)
	local hadron calibrated Kt4 jets			
m_t electron	166.23 ± 2.41	13.35 ± 2.33	167.22 ± 2.38	13.39 ± 2.31
m_t muon	167.62 ± 3.22	15.79 ± 2.52	167.53 ± 3.11	17.63 ± 3.01
	local hadron calibrated AntiKt4 jets			
Δm_t electron	-4.13	0.48	-0.86	2.77
Δm_t muon	1.12	-1.18	3.26	-2.01
	rescaled jet energy 95%			
Δm_t electron	-8.4	-2.03	-1.71	0.06
Δm_t muon	-9.74	-1.97	-1.53	-0.42
	rescaled jet energy 105%			
Δm_t electron	8.54	-1.5	-1.40	0.68
Δm_t muon	8.36	2.27	0.04	-0.7
	rescaled b jet energy 95%			
Δm_t electron	-3.30	-2.12	-2.86	0.66
Δm_t muon	-2.19	-1.53	-2.50	-1.58
	rescaled b jet energy 105%			
Δm_t electron	1.85	0.57	0.80	0.78
Δm_t muon	3.79	-0.06	5.40	-1.7
	2^{nd} jet p_T cut at 30 GeV			
Δm_t electron	-1.12	-1.05	-2.25	0.12
Δm_t muon	-3.15	-0.04	-2.56	-0.18
	2^{nd} jet p_T cut at 50 GeV			
Δm_t electron	3.29	0.18	0.85	-0.88
Δm_t muon	1.52	1.14	-1.20	0.23
	QCD background scaled up by 150%			
Δm_t electron	-0.08	0.38	-0.13	0.40
Δm_t muon	-0.12	0.54	0.06	0.77
	QCD background scaled down by 50%			
Δm_t electron	0.05	-0.45	0.14	-0.46
Δm_t muon	0.27	-0.44	0.05	-0.57
	non-QCD physics background scaled up by 150%			
Δm_t electron	0.07	-0.36	0.04	-0.28
Δm_t muon	-0.51	-0.34	-0.26	-0.47
	non-QCD physics background scaled down by 50%			
Δm_t electron	-0.11	0.35	-0.01	0.27
Δm_t muon	0.49	0.41	0.25	0.58
	all physics background scaled up by 150%			
Δm_t electron	0	0.06	-0.11	0.19
Δm_t muon	-0.66	0.15	-0.21	0.19
	all physics background scaled down by 50%			
Δm_t electron	-0.05	-0.05	0.09	-0.13
Δm_t muon	0.74	-0.10	0.32	-0.08

Table 5.4: Summary of impact of the different variation of systematic effects.

systematic error.
When changing the chosen jet algorithm, and using the Anti-Kt instead of the Kt algorithm, the mean value of the reconstructed mass was shifted by at most 4.13 (1.12) GeV in the electron (muon) channel. The average of 2.63 GeV is taken as a typical value for the variation caused by the jet algorithms and also added as an additional symmetric systematic error.
In order to obtain an overall systematic error, the different contributions: The error of the light and of the b jet energy scale, the fit uncertainty and the uncertainty due to the choice of the jet algorithm, are added in quadrature:

$$\sigma^{electron}_{syst\ tot} = \begin{matrix}+(8.47 \oplus 2.58 \oplus 3 \oplus 2.63) \\ -(8.47 \oplus 2.58 \oplus 0 \oplus 2.63)\end{matrix} = \begin{matrix}+9.71 \\ -9.24\end{matrix} \text{ GeV}$$

$$\sigma^{muon}_{syst\ tot} = \begin{matrix}+(9.05 \oplus 2.99 \oplus 3 \oplus 2.63) \\ -(9.05 \oplus 2.99 \oplus 0 \oplus 2.63)\end{matrix} = \begin{matrix}+10.33 \\ -9.89\end{matrix} \text{ GeV}$$

and after application of the in-situ calibration it decreases to:

$$\sigma^{electron}_{syst\ tot\ ISC} = \begin{matrix}+(0 \oplus 1.83 \oplus 3 \oplus 2.05) \\ -(-1.56 \oplus 1.83 \oplus 0 \oplus 2.05)\end{matrix} = \begin{matrix}+4.07 \\ -3.16\end{matrix} \text{ GeV}$$

$$\sigma^{muon}_{syst\ tot\ ISC} = \begin{matrix}+(0 \oplus 3.95 \oplus 3 \oplus 2.05) \\ -(-0.78 \oplus 3.95 \oplus 0 \oplus 2.05)\end{matrix} = \begin{matrix}+5.37 \\ -4.28\end{matrix} \text{ GeV}$$

	mean (μ) Gaussian fit [GeV]	
	before in-situ calibration	after in-situ calibration
	standard analysis	
m_t electron	166.23 ± 2.41	167.22 ± 2.38
m_t muon	167.62 ± 3.22	167.53 ± 3.11
	Δmean (μ)	Δmean (μ)
	jet energy scale	
Δm_t electron	± 8.47	- 1.56
Δm_t muon	± 9.05	- 0.78
	b jet energy scale	
Δm_t electron	± 2.58	± 1.83
Δm_t muon	± 2.99	± 3.95
	QCD background variation	
Δm_t electron	± 0.06	± 0.14
Δm_t muon	± 0.19	± 0.06
	non-QCD background variation	
Δm_t electron	± 0.09	± 0.02
Δm_t muon	± 0.50	± 0.25
	simultaneous background variation	
Δm_t electron	± 0.02	± 0.10
Δm_t muon	± 0.70	± 0.27
	jet algorithm	
Δm_t	± 2.63	± 2.05
	fit uncertainty	
Δm_t	+ 3.2 ± 2.7	

Table 5.5: Summary of the systematic errors.

5.8 Results

On simulated data with an integrated luminosity of 145 pb^{-1}, the top quark mass was reconstructed in the lepton plus jets decay channel. Using local hadron calibrated jets the mass was found to be

$$m_t^{electron} = 166.23 \pm (2.41)_{stat} \, (^{+9.71}_{-9.24})_{syst} \ GeV$$

in the electron channel, and

$$m_t^{muon} = 167.62 \pm (3.22)_{stat} \, (^{+10.33}_{-9.89})_{syst} \ GeV$$

in the muon channel. Applying an iterative in-situ calibration method, the systematic error on the jet energy scale was reduced. This resulted in a mass of

$$m_t^{electron} = 167.22 \pm (2.38)_{stat} \, (^{+4.07}_{-3.16})_{syst} \ GeV$$

in the electron channel, and

$$m_t^{muon} = 167.53 \pm (3.11)_{stat} \, (^{+5.37}_{-4.28})_{syst} \ GeV$$

in the muon channel.
This is compatible with the input top mass value of 172.5 GeV. Before the application of the in-situ calibration, the dominant errors are the light jet energy scale and the combinatorial background, which causes a large uncertainty in the fitting procedure. After application of the in-situ calibration, only the latter remains dominant. The peaking character of this background just below the region of the signal peak, at slightly lower value, could explain the systematically too low values for the reconstructed top quark mass. The Gaussian part of the fitting function is shifted to lower values, because it tends to absorb a significant part of the background.
With samples of higher statistics the combinatorial background is expected to decrease and the fitting procedure is expected to become more stable.

Chapter 6

Conclusion

Detector Commissioning

During the electronics commissioning phase the hadronic endcap calorimeter was found to be in good shape for data taking. The number of dead or distorted channels was found to to be at an acceptable level and to meet the requirements as defined in the technical design report [78].
First signal shape studies using signals from cosmic muons showed that the measured pulse shape has a residual of less than 5% with respect to the predicted pulse shapes. This number has to be taken as an upper limit as the statistics were limited and the comparison had to be done relying on asynchronous data and averaging over several cells. Once more statistics are available, the study will be repeated and it will be possible to obtain more detailed estimates of the quality of the shape prediction.
For some of the few pathological shapes that were found, the source is not yet clearly understood. Further investigations especially of the correlation with known high voltage problems will have to be carried out.
With first data of LHC beams dumped on beam collimators just outside the ATLAS cavern it was possible to obtain a first impression of the complete calorimeter response. However, also here limited statistics and not precisely tuned data taking conditions were limiting factors. The few channels in which the high voltage was reduced by more than 20% could be confirmed and it hence seems possible to use such data to study and test high voltage corrections.

Top Quark Commissioning Analysis

On simulated data with an integrated luminosity of 145 pb^{-1}, the top quark mass was reconstructed in the lepton plus jets decay channel. The method applied was based on simple event selection cuts. For the events passing the selection, the top quark candidate was chosen by selecting the jet triplet which has the largest p_{T}.
In order to reconstruct the W boson candidate, the three jets constituting the top quark candidate were boosted back to the centre-of-mass frame of the top quark candidate. Then, the di-jet combination, in which the two jets have the minimal distance in ΔR was chosen as W boson candidate.

The precise knowledge of the W boson mass from other measurements was taken as a reference in order to extract the jet energy scale for light jets in the top quark decay. This allowed for the iterative computation of an in-situ calibration function, which was then applied to the jets in the simulated sample.
Using local hadron calibrated Kt4 jets, the top quark mass was found to be $m_t^{\text{electron}} = 166.23 \pm (2.41)_{\text{stat}}\ (^{+9.71}_{-9.24})_{\text{syst}}$ GeV in the electron channel, and $m_t^{\text{muon}} = 167.62 \pm (3.22)_{\text{stat}}\ (^{+10.33}_{-9.89})_{\text{syst}}$ GeV in the muon channel. Applying an iterative in-situ calibration method, the systematic error on the jet energy scale was reduced. This resulted in a mass of $m_t^{\text{electron}} = 167.22 \pm (2.38)_{\text{stat}}\ (^{+4.07}_{-3.16})_{\text{syst}}$ GeV in the electron channel, and $m_t^{\text{muon}} = 167.53 \pm (3.11)_{\text{stat}}\ (^{+5.37}_{-4.28})_{\text{syst}}$ GeV in the muon channel. The obtained values are compatible with the input top mass value of 172.5 GeV. The systematic errors quoted here take into account variations of the light and the b jet energy scale as well as the fit uncertainty and the uncertainty due to the choice of the jet algorithm. Before the application of the in-situ calibration, the dominant errors are the light jet energy scale and the combinatorial background, which causes a large uncertainty in the fitting procedure. After application of the in-situ calibration, only the latter remains dominant. With samples of higher statistics, the combinatorial background is expected to decrease and the fitting procedure is expected to become more stable. At this point, the contribution from physics background is expected to become more important. An additional unknown is the QCD background for which the simulations contain a large uncertainty. Once collision data will become available, it will be possible to extract the QCD background shape from data and it will be possible to further constrain the fit.
As soon as simulated data with different top mass input values will become available, the method has to be calibrated in order to further study possible systematic biases.

Appendix A

ATLAS acronyms

ADC	Analogue-to-Digital Converter
ASIC	Application-Specific Integrated Circuit
ATLAS	A Toroidal LHC ApparatuS
BC	Bunch Crossing
BCID	Bunch-Crossing IDentification
BE	Back-End
BT	Barrel Toroid
CANbus	Controller Area Network bus
CB	Calibration Board
CERN	European Organization for Nuclear Research
COOL	ATLAS-wide conditions database
CSC	Cathode Strip Chambers
CS	Central Solenoid
CTP	Central Trigger Processor
DAC	Digital-to-Analogue Converter
DAQ	Data AcQuision system
DCS	Detector Control System
DLL	Delay Locked Loop
DSP	Digital Signal Processors
DSS	Detector Safety System
EB	Extended Barrel
EC	End-Cap
ECT	End-Cap Toroid
EF	Event Filter
ELMB	Embedded Local Monitor Board
EMB	ElectroMagnetic Barrel calorimeter
EMEC	ElectroMagnetic End-cap Calorimeter
EM	ElectroMagnetic
EST	ElectroStatic Transformer
FCal	Forward Calorimeter
FEB	Front-End Board
FECcont	Front-End Crate controller board
FEC	Front-End Crate
FE	Front-End
FIFO	First-In/First-Out
FPGA	Field-Programmable Gate Array
FSR	Final State Radiation
FT	Feed-Through
GSEL	Gain-SELector chip
HAD	HADron calorimeter
HEC	Hadronic End-cap Calorimeter
HLT	High-Level Trigger
HRL	High Resistive Layer on the HEC electrodes
HV	High Voltage
HVPS	High Voltage Power Supply
IC	Integrated Circuit
ID	Inner Detector
ISR	Initial State Radiation

ITC	Inter TileCal scintillators
JES	Jet Energy Scale
L1A	Level-1 Accept
L1Calo	Level-1 Calorimeter trigger
L1	Level-1 trigger
L2	Level-2 trigger
L2PU	Level-2 Processing Unit
L2SV	Level-2 SuperVisor
LAr	Liquid Argon
LHC	Large Hadron Collider
LV	Low Voltage
LVPS	Low Voltage Power Supply
MDT	Monitored Drift Tubes
MIP	Minimum Ionising Particle
MSSM	Minimal Symmetric extension of the SM
OFC	Optimal Filtering Coefficients
OF	Optimal Filtering
OHS	Online Histogramming Service
OTx	Optical Transmitter
PAD	readout electrodes of the LAr calorimeters
PDF	Parton Distribution Function
PLL	Phase Locked Loop
PMT	PhotoMultiplier Tube
PP	Patch Panel
PS	Presampler
PSB	Preamplification and Summing Board of the HEC cold electronics
PVSS	Prozessvisualisierungs und Steuerungs System
QCD	Quantum Chromo Dynamics
QPLL	Quarz Phase Locked Loop
ROBIN	ReadOut Buffer Module
ROB	ReadOut Buffer
ROC	ReadOut Crate
ROD	ReadOut Driver
RoIB	Region-of-Interest Builder
RoI	Region-of -Interest
RPC	Resistive Plate Chambers
SCA	Storage Capacitor Array
SCA	Switched Capacitor Array
SCT	SemiConductor Tracker
SM	Standard Model of Particle Physics
SLC	Scientific Linux CERN
SPAC	Serial Protocol for Atlas Calorimeters
SUSY	SUper SYmmetric extension of the SM
TBB	Tower Builder Board
TDAQ	Trigger and Data AcQuision
TDB	Tower Driver Board
TDR	Technical Design Report
TGC	Thin Gap Chambers
TileCal	Tile Calorimeter
TLA	Three Letter Acronym
TR	Transition Radiation
TRT	Transition Radiation Tracker
TTC	Trigger, Timing, and Control
TTCR	Trigger, Timing, and Control Receiver
TTCrx	Trigger, Timing, and Control Receiver chip
TTC	Timing, Trigger, and Control
TTCvi	Timing, Trigger, and Control VME interface module
UE	Underlying Event
USA	Underground Service Area
VME	Versa Module Eurocard
VMEbus	Versa Module Euro bus
WLS	WaveLength Shifting

List of Figures

List of Tables

Bibliography

[1] Glashow, S. L., Partial Symmetries of Weak Interactions, Nucl. Phys. **22** (1961) 579–588.

[2] Goldstone, J., Salam,A. and Weinberg, S., Broken Symmetries, Phys. Rev. **127** (1962) 965–970.

[3] Weinberg, Steven, A Model of Leptons, Phys. Rev. Lett. **19** (1967) 1264–1266.

[4] Glashow, S. L. and Iliopoulos, J. and Maiani, L., Weak Interactions with Lepton-Hadron Symmetry, Phys. Rev. D **2** (1970) 1285–1292.

[5] Georgi, H. and Glashow, S. L., Unified Weak and Electromagnetic Interactions without Neutral Currents, Phys. Rev. Lett. **28** (1972) 1494–1497.

[6] Politzer, H. D., Reliable Perturbative Results for Strong Interactions, Phys. Rev. Lett. **30** (1973) 1346–1349.

[7] Politzer, H. D., Asymptotic Freedom: An Approach to Strong Interactions, Phys. Rept. **14** (1974) 129.

[8] Gross, D. J. and Wilczek, F., Asymptotically Free Gauge Theories, Phys. Rev. D **8** (1973) 3633–3652.

[9] Amsler, C. and Doser, M., Review of Particle Physics, Phys. Lett. **B 667** (2008) 1.

[10] J. Wess and B. Zumino, Supergauge Transformations in Four-Dimensions, Nucl. Phys. **B70** (1974) 39–50.

[11] Nilles, H. P., Supersymmetry, supergravity and particle physics, Phys. Rep. **110** (1984) 1.

[12] Haber, H. E. and Kane, G. L., The search for supersymmetry: Probing physics beyond the standard model, Phys. Rep. **117** (1985) 75.

[13] M.B. Green and J.H. Schwarz, Anomaly Cancellation in Supersymmetric D=10 Gauge Theory and Superstring Theory, Phys. Lett. **B149** (1984) 117–122.

[14] Cabbibo, N., Unitary Symmetry and Leptonic Decays, Phys. Rev. Lett. **10** (1963) 531–532.

[15] Kobayashi, M. and Maskawa, T., CP Violation in the Renormalizable Theory of Weak Interaction, Prog. Theor. Phys. **49** (1973) 652–657.

[16] Arnison, G. *et al.*, Phys. Lett. B **122** (1983) 103.

[17] M. Banner *et al.*, Phys. Lett. B **122** (1983) 476.

[18] Higgs, Peter W., Broken Symmetries and the Masses of Gauge Bosons, Phys. Rev. Lett. **13** (1964) 508–509.

[19] Fritzsch, H. and Gell-Mann, Murray and Leutwyler, H., Advantages of the Color Octet Gluon Picture, Phys. Lett. **B47** (1973) 365–368.

[20] Gross, D. J. and Wilczek, Frank, ULTRAVIOLET BEHAVIOR OF NON-ABELIAN GAUGE THEORIES, Phys. Rev. Lett. **30** (1973) 1343–1346.

[21] Bethke, Siegfried, Experimental Tests of Asymptotic Freedom, Prog. Part. Nucl. Phys. **58** (2007) 351–386.

[22] Sjostrand, Torbjorn and Mrenna, Stephen and Skands, Peter, PYTHIA 6.4 physics and manual, JHEP **05** (2006) 026.

[23] Corcella, G. *et al.*, HERWIG 6.5: An event generator for hadron emission reactions with interfering gluons (including supersymmetric processes), JHEP **01** (2001) 010.

[24] Catani, S., Aspects of QCD, From the Tevatron to the LHC, Proceedings of Workshop on Physics at TeV Colliders, Les Houches, France, 7-18 Jun 1999 (2000).

[25] S. Moch and P. Uwer, Theoretical status and prospects for top-quark pair production at hadron colliders, Physical Review D (Particles and Fields) **78** (2008) 034003.

[26] Sullivan, Zack, Understanding single-top-quark production and jets at hadron colliders, Phys. Rev. D **70** (2004) 114012.

[27] John Campbell and Francesco Tramontano, Next-to-leading order corrections to Wt production and decay, Nuclear Physics B **726** (2005) 109 – 130.

[28] G.O. Dovier, Single top cross section, ATLAS internal presentation.

[29] LEP-Electroweak Working Group and the LEP Collaborations: ALEPH, DELPHI, L3 and OPAL, Electroweak Parameters of the Z^0 Resonance and the Standard Model, Phys. Lett. B **276** (1992) 247–253.

[30] Abachi, S. *et al.*, Observation of the Top Quark, Phys. Rev. Lett. **74** (1995) 2632–2637.

[31] Abe, F. *et al.*, Observation of Top Quark Production in $p\bar{p}$ Collisions with the Collider Detector at Fermilab, Phys. Rev. Lett. **74** (1995) 2626–2631.

[32] The ALEPH, DELPHI, L3, OPAL, SLD Collaborations, the LEP Electroweak Working Group, the SLD Electroweak and Heavy Flavour Groups, Precision Electroweak Measurements on the Z Resonance, CERN-PH-EP/2005-XXX, SLAC-R-774 (2005) 302.

[33] Tevatron Electroweak Working Group and for the CDF Collaboration and The D0 Collaboration, Combination of CDF and D0 Results on the Mass of the Top Quark.

[34] I. Bigi, On the hadronization of top quarks, Phys. Lett. **B 175** (1986) 233.

[35] Cooper-Sarkar, A. M. and Devenish, R. C. E. and De Roeck, A., Structure Functions of the Nucleon and their Interpretation, Int. J. Mod. Phys. A **13** (1998) 3385–3586.

[36] Lai, H. L. and others, Global QCD analysis of parton structure of the nucleon: CTEQ5 parton distributions, Eur. Phys. J. C **12** (2000) 375.

[37] Pumplin, J. and Stump, D. R. and Huston, J. and Lai, H. L. and Nadolsky, P. and Tung, W. K., New Generation of Parton Distributions with Uncertainties from Global QCD Analysis, J. High Energy Phys. **0207** (2002) 012.

[38] Alekhin, Sergey and Melnikov, Kirill and Petriello, Frank, Fixed target Drell-Yan data and NNLO QCD fits of parton distribution functions, Phys. Rev. **D74** (2006) 054033.

[39] Martin, A. D. and Stirling, W. J. and Thorne, R. S. and Watt, G., Update of parton distributions at NNLO, Phys. Lett. **B652** (2007) 292–299.

[40] Blumlein, Johannes and Bottcher, Helmut and Guffanti, Alberto, Non-singlet QCD analysis of deep inelastic world data at O(alpha(s)**3), Nucl. Phys. **B774** (2007) 182–207.

[41] Beneke, M. and Efthymiopoulos, I. and Mangano, M. L. Womersley, J. *et al.*, Top Quark Physics, in *Proceedings of 1999 CERN Workshop on Standard Model Physics (and more) at the LHC*, G. Altarelli and M.L. Mangano eds (2000).

[42] The ALEPH, DELPHI, L3, OPAL, SLD Collaborations, the LEP Electroweak Working Group, the SLD Electroweak and Heavy Flavour Groups, A Combination of Preliminary Electroweak Measurements and Constraints on the Standard Model, CERN-PH-EP/2004-069 (2004).

[43] The ALEPH, DELPHI, L3, OPAL, SLD Collaborations, the LEP Electroweak Working Group, the SLD Electroweak and Heavy Flavour Groups, A Combination of Preliminary Electroweak Measurements and Constraints on the Standard Model, Updated for 2005 summer conferences: `http://www.cern.ch/LEPEWWG` (2005).

[44] Precision Electroweak Measurements and Constraints on the Standard Model, (2008).

[45] The LEP Working Group for Higgs Boson Searches and Barate, R. and others, Search for the Standard Model Higgs Boson at LEP, Phys. Lett. B **565** (2003) 61–75.

[46] Slabospitsky, S. R., Event generators for top quark production and decays, PoS **TOP2006** (2006) 019.

[47] B.P. Kersevan and E. Richter-Was, The Monte Carlo event generator AcerMC version 2.0 with interfaces to PYTHIA 6.2 and HERWIG 6.5, (2004).

[48] Kersevan, B. P. and Richter-Was, E., The Monte Carlo event generator AcerMC version 1.0 with interfaces to PYTHIA 6.2 and HERWIG 6.3, Comput. Phys. Commun. **149** (2003) 142.

[49] Mangano, M. L. and others, ALPGEN, a generator for hard multiparton processes in hadronic collisions, J. High Energy Phys. **0307** (2003) 001.

[50] S. Frixione and B.R. Webber, Matching NLO QCD computations and parton shower simulations, JHEP **06** (2002) 029.

[51] Frixione, S. and Webber, B., The MC@NLO Event Generator, (2004).

[52] Frixione, S. and Nason, P. and Webber, B., Matching NLO QCD and parton showers in heavy flavour production, J. High Energy Phys. **0308** (2003) 007.

[53] Frixione, S. and Webber, B., The MC@NLO 3.1 event generator, (2005) 22.

[54] Frixione, S. and Laenen, E. and Motylinski, P. and Webber, B., Single-top production in MC@NLO, J. High Energy Phys. **0603** (2006) 092.

[55] Frixione, S. and Webber, B., The MC@NLO 3.2 event generator, (2006) 23.

[56] Catani, S. and Krauss, F. and Kuhn, R. and Webber, B. R., QCD Matix Elements + Parton Showers, J. High Energy Phys. **0111** (2001) 063.

[57] Krauss, F., Matrix Elements and Parton Showers in Hadronic Interactions, J. High Energy Phys. **0208** (2002) 015.

[58] Mangano, M. L., A Review of MLM's Prescription for Removal of Double Counting, `http://cepa.fnal.gov/patriot/mc4run2/MCTuning/061104/mlm.pdf` (2004).

[59] Mrenna, S. and Richardson, P., Matching Matrix Elements and Parton Showers with HERWIG and PYTHIA, J. High Energy Phys. **0405** (2004) 040.

[60] Lyndon Evans and Philip Bryant (editors), LHC Machine, JINST **3** (2008) S08001.

[61] Christine Vanoli, The CERN accelerator complex. Complexe des acc él érateurs du CERN, `http://cdsweb.cern.ch/record/979035`, Jun 2006.

[62] Aamodt, K. and others, The ALICE experiment at the CERN LHC, JINST **3** (2008) S08002.

[63] Alves, A. Augusto and others, The LHCb Detector at the LHC, JINST **3** (2008) S08005.

[64] The CMS Collaboration, S. Chatrchyan *et al.*, The CMS experiment at the CERN LHC, JINST **3** (2008) S08004.

[65] The ATLAS Collaboration, G. Aad *et al.*, The ATLAS Experiment at the CERN Large Hadron Collider, JINST **3** (2008) S08003.

[66] Arkani-Hamed, N. and Dimopoulos, S. K. and Dvali, G. R., The Hierarchy Problem and New Dimensions at a Millimeter, Phys. Lett. **B 429** (1998) 263–272.

[67] Georgi, H. M. and Glashow, S. L., Unity of All Elementary-Particle Forces, Phys. Rev. Lett. **32** (1974) 438–441.

[68] A. Salam, Elementary Particle Theory, Almqvist and Wiksell, Stockholm, 1968.

[69] J. Colas *et al.*, Position resolution and particle identification with the ATLAS EM calorimeter, NIM **A550** (2005) 96–115.

[70] M. Aharrouche *et al.*, Energy linearity and resolution of the ATLAS electromagnetic barrel calorimeter in an electron test-beam, NIM **A568** (2006) 601–623.

[71] M. Aharrouche *et al.*, Response Uniformity of the ATLAS liquid argon electromagnetic calorimeter, NIM **A582** (2007) 429–455.

[72] J. Pinfold *et al.*, Hadronic Calibration of the ATLAS Liquid Argon End-Cap Calorimeter in the Pseudorapidity Region $2.5 < |\eta| < 4.0$ in Beam Tests, submitted to NIM.

[73] C. Cojocaru *et al.*, Hadronic calibration of the ATLAS liquid argon end-cap calorimeter in the pseudorapidity region $1.6 < |\eta| < 1.8$ in beam tests, NIM **A531** (2004) 481–514.

[74] J. P. Archambault *et al.*, Energy Calibration of the ATLAS Liquid Argon Forward Calorimeter, JINST **3** (2008) P02002.

[75] M. Aharrouche *et al.*, Electron Performance of the ATLAS Liquid Argon Calorimeter measured at the 2004 Combined Test Beam, submitted to NIM.

[76] M. Aharrouche, The ATLAS liquid argon calorimeter: Construction, Integration, Commissioning and Combined Test beam results, contribution to XIth Vienna Conference on Instrumentation, Vienna (2007).

[77] A. E. Kiryunin *et al.*, GEANT 4 physics evaluation with testbeam data of the ATLAS hadronic end-cap calorimeter, NIM **A560** (2006) 278–290.

[78] The ATLAS Collaboration, Liquid Argon Calorimeter: Technical Design Report, 1996, CERN-LHCC-96-41.

[79] Buchanan, N. J. *et al.*, ATLAS liquid argon calorimeter front end electronics, JINST **3** (2008) P09003.

[80] D. Axen et al., Signal feedthroughs for the ATLAS barrel and endcap calorimeters, RSI **76** (2005) 063306.

[81] Bazan, A. *et al.*, ATLAS liquid argon calorimeter back end electronics, JINST **2** (2007) P06002.

[82] Buchanan, N. J. *et al.*, Design and implementation of the Front End Board for the readout of the ATLAS liquid argon calorimeters, JINST **3** (2008) P03004.

[83] Colas, J. *et al.*, Electronics calibration board for the ATLAS liquid argon calorimeters, Nucl. Instrum. Meth. **A593** (2008) 269–291.

[84] Achenbach, R. *et al.*, The ATLAS level-1 calorimeter trigger, JINST **3** (2008) P03001.

[85] Timing, Trigger and Control (TTC) Systems for the LHC, `http://ttc.web.cern.ch/TTC/intro.html`.

[86] F Hubaut *et al.*, Specifications of the Serial Protocol for the ATLAS LAr Calorimeters: The SPAC3 Protocol and Slave ASIC, `https://edms.cern.ch/file/110351/3/`, 2006, ATL-AL-ES-0005.

[87] The ATLAS Collaboration, ATLAS Technical Proposal, 1994, CERN-LHCC-94-43.

[88] Athanasios Papoulis, Signal analysis, (McGraw-Hill, 1977).

[89] W.E. Cleland and E.G. Stern, Signal processing considerations for liquid ionization calorimeters in a high rate environment, Nucl. Instrum. Meth. **A338** (1994) 467–497.

[90] J. Colas, M.Pirpstein and W.A. Wenzel, The Electro Static Transformer, Nucl. Instrum. Meth. **A294** (1990) 583 –590.

[91] Ban, J. *et al.*, Cold electronics for the liquid argon hadronic end cap calorimeter of ATLAS, Nucl. Instrum. Meth. **A556** (2006) 158–168.

[92] Kurchaninov, L. and Strizenec, P., Calibration and ionization signals in the hadronic endcap calorimeter of ATLAS, Prepared for 9th Conference on Calorimetry in High Energy Physics (CALOR 2000), Annecy, France, 9-14 Oct 2000.

[93] Wilkens, H., First experience with the readout electronics on the ATLAS EM barrel calorimeter at cold, **3** , 1966.

[94] J. Christiansen, A. Marchioro, P. Moreira and A. Sancho, TTCrx, an ASIC for Timing, Trigger and Control Distribution in LHC Experiments, IEEE Trans. Nuclear Science **Vol. 43** (1996) 1773–1777.

[95] J. Christiansen, A. Marchioro and P. Moreira, TTCrx, an ASIC for Timing, Trigger and Control Distribution in LHC Experiments, Second Workshop on Electronics for LHC Experiments, Balatonf .

[96] Manual for the TTC reciever (TTCrx), `http://ttc.web.cern.ch/TTC/TTCrx_manual3.11.pdf`.

[97] M. Aleksa et al., Construction, Assembly and Tests of the ATLAS Electromagnetic End-Cap Calorimeter, JINST **3** (2008) submitted to JINST.

[98] B. Belhorma et al., Evaporating short-circuits in the ATLAS liquid argon barrel presampler 006, ATLAS Note ATL-LARG-PUB-2005-003 (2005).

[99] M. Kazarinov, Electric Field in Shorted Subgaps of the HEC, `http://indico.cern.ch/conferenceDisplay.py?confId=29482`.

[100] B. Aubert et al., Performance of the ATLAS electromagnetic calorimeter end-cap module 0, NIM **A500** (2003) 178–201.

[101] Dowler, B. and others, Performance of the ATLAS hadronic end-cap calorimeter in beam tests, Nucl. Instrum. Meth. **A482** (2002) 94–124.

[102] Cooke *et al.*, In situ commissioning of the ATLAS electromagnetic calorimeter with cosmic muons, Internal Report ATL-LARG-PUB-2007-013. ATL-COM-LARG-2007-012, CERN, Geneva, Nov 2007.

[103] Gabaldon Ruiz, C and Kuna, M and Hubaut, F and Pralavorio, P and Del Peso, J, Signal reconstruction in the EM end-cap calorimeter and check with cosmic data in the region $0 < \eta < 3.2$, Internal Report ATL-LARG-PUB-2008-001. ATL-COM-LARG-2008-001, CERN, Geneva, Feb 2008.

[104] M. Delmastro, Approximate estimate of optimal filtering bias on pulse amplitude reconstruction, `http://indico.cern.ch/materialDisplay.py?contribId=7&materialId=paper&confId=55718`.

[105] M. Delmastro, Quality factor analysis and optimization of digital filtering sign al reconstruction for liquid ionization calorimeters, NIM **A600** (2009) 545–554.

[106] ATLAS end-cap toroids: Technical Design Report, (CERN, Geneva, 1997), Electronic version not available.

[107] The Athena Framework, `https://twiki.cern.ch/twiki/bin/view/Atlas/AthenaFramework`.

[108] LHCb Software Architecture Group, GAUDI Architecture Design Document, `http://lhcb-comp.web.cern.ch/lhcb-comp/Meetings/offline/pdf/add.pdf`, 1998.

[109] The LHCb Collaboration, Gaudi Users Guide, `http://cern.ch/lhcb-comp/Frameworks/Gaudi/Gaudi_v9/GUG/GUG.pdf`, 2001.

[110] R. Brun and others, `http://root.cern.ch`.

[111] Lampl, W. and others, Calorimeter Clustering Algorithms: Description and Performance, ATLAS note, 2008, ATL-LARG-PUB-2008-002.

[112] Speckmayer, P., Energy measurement of hadrons with the CERN ATLAS calorimeter, Ph.D. thesis, Technische Universität Wien, 2008, CERN-THESIS-2008-051.

[113] Catani, S. and Dokshitzer, Yuri L. and Webber, B. R., The K^- perpendicular clustering algorithm for jets in deep inelastic scattering and hadron collisions, Phys. Lett. **B285** (1992) 291–299.

[114] J.M. Butterworth *et al.*, KtJet: A C++ implementation of the K(T) clustering algorithm, Comput. Phys. Commun. **153** (2003) 85–96.

[115] M. Cacciari and G.P. Salam, Dispelling the N**3 myth for the k(t) jet-finder, Phys. Lett. **B641** (2006) 57–61.

[116] Matteo Cacciari and Gavin P. Salam and Gregory Soyez, The anti-kt jet clustering algorithm, Journal of High Energy Physics **2008** (2008) 063.

[117] Lampl, W., Laplace, S., Lechowski, M., Rousseau, D., Ma, H., Menke, S. and Unal, G., Digitization of LAr calorimeter for CSC simulations, (2007).

[118] Issever, C. and Borras, K. and Wegener, D., An improved weighting algorithm to achieve software compensation in a fine grained LAr calorimeter, Nucl. Instrum. Meth. **A 545** (2005) 803–812.

[119] Aad, G. *et al.*, Expected Performance of the ATLAS Experiment - Detector, Trigger and Physics, (2009).

[120] Barillari, T. and others, Local Hadronic Calibration, ATLAS note, ATL-LARG-PUB-2009-001.

[121] Agostinelli, S. and others, Geant4 - a simulation toolkit, Nucl. Instrum. Meth. **A 506** (2003) 250–303.

[122] Quadt, A., Top quark physics at hadron colliders, Eur. Phys. J. **C 48** (2006) 835–1000.

[123] ATLAS detector and physics performance: Technical Design Report, 1, (CERN, Geneva, 1999), Electronic version not available.

[124] Doxiadis, A and Kayl, M, Estimating the isolated lepton rate in multi-jet events, Internal Report ATL-PHYS-INT-2008-022. ATL-COM-PHYS-2008-004, CERN, Geneva, Jan 2008.

[125] MPP top quark mass analysis software repository, `http://atlas-sw.cern.ch/cgi-bin/viewcvs-atlas.cgi/groups/MPP/ARA_Examples_Top/`.

[126] Bentvelsen, Stanislaus Cornelius Maria and Cobal, M, Top studies for the Atlas detector commissioning, Internal Report ATL-PHYS-PUB-2005-024. ATL-COM-PHYS-2005-039, CERN, Geneva, 2005.

[127] Verkerke, W and Van Vulpen, I, Commissioning ATLAS using top-quark pair production, Internal Report ATL-COM-PHYS-2007-023, CERN, Geneva, Apr 2007.

[128] J.M. Butterworth, J.R. Forshaw and M.H. Seymour, Multiparton interactions in photoproduction at HERA, Z. Phys. **C72** (1996) 637–646.

[129] W.-M. Yao *et al.*, Review of Particle Physics, Journal of Physics G **33** (2006 and 2007 partial update for the 2008 edition available on the PDG WWW pages (`http://pdg.lbl.gov/`)).

[130] M.L. Mangano, Merging Matrix elements and shower MCs, `http://cern.ch/~mlm/talks/lund-alpgen.pdf`, Talk at Lund University.

[131] Top Quark Monte Carlo Dataset References for 10TeV Production, `https://twiki.cern.ch/twiki/bin/view/AtlasProtected/TopReferences10TeV`.

Acknowledgements

In the past five years I was granted the opportunity participate in the vast research field of high-energy physics. I am very grateful to those who made this experience possible for me. In first instance this is Professor Dr. S. Bethke, being my academic supervisor. He gave me the opportunity to carry out this work during my stay at CERN and in the last year at the Max-Planck-Institut in Munich.
As a member of the Hadronic Endcap Calorimeter group at the Max-Planck-Institute in Munich I would like to thank all the members of this group, who always supported me in the different questions I came up with. Also the members of the MPI top group deserve my thanks for the help in setting up the analysis in our common framework. Especially, I want to express my gratitude to my advisors Dr. S. Menke, Dr. H. Oberlack and Dr. P. Schacht for their support. In particular Sven invested a lot of his time in helping me with all the different computing and physics issues I was stuck in - THANKS!
As a regular guest at the MPI and especially during the time I spent at CERN, Dr. P. Strizenec deserves my thanks for all the support he gave in the commissioning tasks - it was always a great pleasure debugging detector and code with him.
For my time at CERN I want to thank the members of the liquid argon group at CERN, who always helped me with the HEC specific issues which sometimes risked to come under in the commissioning effort...
And of course a great thanks to my office mates, my 'Mamas'! For the first two years Mama-Gabi in our Datcha at CERN, she really helped me to quickly feel at home in Geveva - MERCI! Then Mama-Marlene and Teresa here at the MPI. It was always fun with you in our offices!
Last but not least I thank all my family and Magdalena for the huge amount of patience in putting up with me during the past months where I became a boring and self- or at least PhD-centered nerd.